Distribution Agreement

In presenting this thesis or dissertation as a partial fulfillment of the requirements for an advanced degree from Emory University, I hereby grant to Emory University and its agents the non-exclusive license to archive, make accessible, and display my thesis or dissertation in whole or in part in all forms of media, now or hereafter known, including display on the world wide web. I understand that I may select some access restrictions as part of the online submission of this thesis or dissertation. I retain all ownership rights to the copyright of the thesis or dissertation. I also retain the right to use in future works (such as articles or books) all or part of this thesis or dissertation.

Signature:

_____ _____

Pui-Yan Ma Date

DNA Nanotechnology as an Emerging Tool to Investigate Cell Mechanics: From Studying T Cell Mechanotransduction to Development of Catalytic Amplification Assay for Readout of Cellular Forces

By

Pui-Yan Ma
Doctor of Philosophy

Chemistry

_____

Khalid Salaita
Advisor

_____

Vince Conticello
Committee Member

_____

R. Brian Dyer
Committee Member

Accepted:

_____

Lisa A. Tedesco, Ph.D.
Dean of the James T. Laney School of Graduate Studies

_____

Date

DNA Nanotechnology as an Emerging Tool to Investigate Cell Mechanics: From Studying T Cell Mechanotransduction to Development of Catalytic Amplification Assay for Readout of Cellular Forces

By

Pui-Yan Ma
B.S., Hong Kong Baptist University, 2012

Advisor: Khalid Salaita, Ph.D.

An abstract of
A dissertation submitted to the Faculty of the
James T. Laney School of Graduate Studies of Emory University
in partial fulfillment of the requirements for the degree of
Doctor of Philosophy
in Chemistry
2019

Abstract

DNA Nanotechnology as an Emerging Tool to Investigate Cell Mechanics: From Studying T Cell Mechanotransduction to Development of Catalytic Amplification Assay for Readout of Cellular Forces

By Pui-Yan Ma

T cells are key players in adaptive immune system, and their activation is crucial for maintaining functional defense mechanisms that destroy infected or cancer cells. Productive T cell activation only occurs when T cells form physical contact with opposing cells that present cognate antigens on their surfaces. This initial antigen recognition by T cell receptor triggers a series of phosphorylation events that ultimately activates T cell signaling and functions. Recent work has demonstrated externally applied forces can activate T cells. However, whether T cells generate internal forces transmitted to the surface receptors and whether these forces have a role in regulating T cell signaling and functions remain unexplored.

This thesis presents two separate lines of studies pertaining to development of biophysical tools that harness mechanical properties of DNA to study cell mechanics. In the first part of this thesis, I developed and applied DNA-based force probes that report (or physically cap) forces generated by the surface receptors of T cells with high spatial, temporal and force resolution. Work presented in Chapter 2 revealed that T cell receptor transmits pN forces to its antigen at artificial cell-cell junctions, using hybrid supported lipid bilayer as a model cell surface. Importantly, these forces persist when T cell receptor-antigen complexes spatially reorganize at the junction. In Chapter 3, I showed that T cell's LFA-1 adhesion receptor is a mechanosensor, where lateral mobility of cognate ICAM-1 ligand controls T cell-substrate interaction. I demonstrated LFA-1 can transmit forces >19 pN upon cell adhesion and migration, with a distinct force pattern compared to T cell receptor forces. Lastly, I discovered that LFA-1 mechanically communicates with T cell receptor to achieve fine-tuned T cell spreading, early signaling and functional responses. In the second part of this thesis (Chapter 4), I developed the first catalytic amplification assay for readout of integrin forces generated by fibroblasts. Additionally, I examined its potential in screening drugs that impair cell mechanics in a high throughput format. Overall, this thesis showcases the potential uses of engineered DNA structures as novel biophysical tools to revolutionize cellular force measurement.

DNA Nanotechnology as an Emerging Tool to Investigate Cell Mechanics: From Studying T Cell Mechanotransduction to Development of Catalytic Amplification Assay for Readout of Cellular Forces

By

Pui-Yan Ma
B.S., Hong Kong Baptist University, 2012

Advisor: Khalid Salaita, Ph.D.

A dissertation submitted to the Faculty of the
James T. Laney School of Graduate Studies of Emory University
in partial fulfillment of the requirements for the degree of
Doctor of Philosophy
in Chemistry
2019

Acknowledgements

Every PhD trainee must have gone through up and down. Mine was the same. I still remembered the tremendous amount of time I spent chasing on bad ideas (which I thought they were good at the very beginning!) and repeatedly working on bad experimental designs. On the other side. I enjoyed my time here mentoring students, travelling to conferences and talking to people with similar mindset day-to-day. This is truthy an unforgettable experience that cannot be find elsewhere.

This thesis cannot be done without the support of my advisor Professor Khalid Salaita. I first met with him 6 years ago in Hong Kong while he was travelling to give a talk there. During that time, I was about to make a tough decision on choosing a suitable oversea institute for my PhD studies. He has a unique persona that really is the primary reason attracting me to go to Emory. Still, I have not regretted my decision once. Khalid cares about our personal growth as a research. Despite his busy schedule, he can always squeeze time to talk and we can randomly pop in and discuss science and life with him. I am extremely grateful to have Khalid as my mentor. Without him, I will not be a mature, successful and independent scientist as of today. Thank you.

I would also love to thank my past and present committee members–Professor David Lynn, Professor Vincent Conticello and Professor Brian Dyer–for their profound insight, encouragement and support throughout my time at Emory. Other mentors I would like to thank are Professor Brian Evavold (Univ. Utah, Immunology), Professor Cheng Zhu (Georgia Tech, BME) and Professor Ronen Alon (Weissman Institute of Science, Immunology). As a Chemistry student without any

formal training in molecular immunology, they are willing to provide guidance and thoughts whenever I needed to make advance on my work.

I am also thankful to wonderful scientists and good friends that I crossed path with and learnt a lot from when I first joined the Salaita lab 5 years ago: Zheng Liu, Weiwei Zhang, Daniel Stabley, Yoshie Narui, Yun Zhang and Yuan Chang. Special tribute goes to Kevin Yehl, Yang Liu and Korelia Gailor who are good mentors and collaborators lifelong friends. I learnt a lot on DNA nanotechnology from Kevin, T cell mechanobiology from Yang and protein chemistry from Kornelia. Even now they often provide me guidance on many aspects of my life.

My sincere appreciation also goes to the current Salaita lab members: Kim Clarke, Jing Zhao, Josh Brockman, Roxy Glazier, Hanquan Su, Aaron Blanchard, Alisina Bazrafshan, Dale Comb, Brendan Deal, Rong Ma, Yixiao Dong, Anna Keller, Allison Ramey, Aysha Rashid, Yuxin Duan, Radhika Sharma, Rachel Bender, Jiahui Zhang, Yuesong Hu and Selma Piranej. The size of the lab has expanded twice since I joined but I find quite rare that we can maintain still a strong "bond" among each other. I will certainly miss the routine lab outings/ramen nights!

I also thank many of my friends that share the same culture and have helped me going through the tough time in graduate school: George Leung, Adriana Miu, Isaac Fung, Zion Tse, Chi Ngai, Lexie Chan, Julian Kwok and Julian Chan and Gary Lam. I shall remember the joy that we have had over the past six years.

The best part of being a graduate student is the opportunities to travel. I am luckily enough to meet a lot of interesting friends, who I am still keeping contact with, during the Lindau Nobel Laureate meeting and Scifinder future leaders program and thank you for your continuous love and support.

I want to dedicate the second last section to my family. My mom and Dad for their continuous support and love across the Pacific Ocean. My brother Yan-Kiu Ma who always look after my parents while I am away from home. Most importantly, my wife Ina Lee for tolerating me leaving Hong Kong for so long! After few more years I will be done with “schooling” (that’s our unique language) and I promise I will be making our lives as colorful as I can.

Lastly, I would like to express my gratitude to the predoctoral to post-doctoral transition award (F99/K00) administered by National Institutes of Health, US for the support of part of this thesis.

Table of contents

List of figures

List of schemes

List of tables

List of abbreviations

TCR	T cell receptor
pMHC	Peptide-major histocompatibility complex
ITAM	Immunoreceptor tyrosine-based activation motif
ZAP-70	Zeta-chain-associated protein kinase 70
Lck	Lymphocyte-specific protein tyrosine kinase
IS	Immunological synapse
cSMAC	Central supramolecular activation cluster
pSMAC	Peripheral supramolecular activation cluster
dSMAC	Distal supramolecular activation cluster
LFA-1	Lymphocyte function-associated antigen 1
ICAM-1	Intercellular Adhesion Molecule 1
OT	Optical tweezer
AFM	Atomic force microscopy
ECM	Extracellular matrix
FA	Focal adhesion
RTK	Receptor tyrosine kinase
TFM	Traction Force Microscopy
SMFS	Single Molecule Force Spectroscopy
MT	Magnetic Tweezer
BFP	Biomembrane Force Probe
FRET	Fluorescence Resonance Energy Transfer
PEG	Polyethylene glycol

Tsmod	Genetically encoded tension sensor
PECAM-1	Platelet Endothelial Cell Adhesion Molecule 1
EGFR	Epidermal growth factor receptor
GC	Guanine-Cytosine
WLC	Worm-like chain
QE	Quenching efficiency
RGD	Arg-Gly-Asp
TGT	Tension gauge tether
ITS	Integrative tension sensor
PSGL	P-selectin glycoprotein ligand-1
FISH	Fluorescence *in situ* hybridization
OMA	Optomechanical actuator
NIR	Near-infrared
MTFM	Molecular tension fluorescence-based microscopy
AuNP	Gold nanoparticle
SLB	Supported lipid bilayer
NSET	Nanometal Surface Energy Transfer
DLS	Dynamic light scattering
RICM	Reflection interference contrast microscopy
ROI	Region of interest
IL-2	Intraleukin-2
NK cell	Neutral killer cell
DOPC	1,2-dioleoyl-sn-glycero-3-phosphocholine

DPPC	1,2-dipalmitoyl-sn-glycero-3-phosphocholine
SUV	Small unilamellar vesicle
Biotinyl Cap-PE	1,2-dipalmitoyl-sn-glycero-3-phosphoethanolamine-N-(cap biotinyl) (sodium salt)
FRAP	Fluorescence Recovery After Photobleaching
PMA	Phorbol 12-myristate 13-acetate
Nck	Non-catalytic region of tyrosine kinase
Wasp	Wiskott–Aldrich Syndrome protein
NA	Numerical aperture
PCR	Polymerase chain reaction
ELISA	Enzyme-linked immunosorbent assay
MCR	Mechanically-induced catalytic amplification reaction
RCA	Rolling circle amplification
CV	Coefficient of variation
DMEM	Eagle's minimal essential medium
PBS	Phosphate buffered saline
HBSS	Hanks buffered salt solution
RPMI	Roswell Park Memorial Institute

Chapter 1

Introduction

Part of this chapter is adapted from **Ma, V.-P.-Y.** and Salaita, K. DNA Nanotechnology as an Emerging Tool to Study Mechanotransduction in Living Systems. *Small*, **2019**, DOI: 10.1002/smll.201900961

1.1. Molecular mechanism of T cell activation

T cells are highly mobile and have the ability to patrol the body [1-2] to swiftly identify and destroy foreign pathogens and cancerous cells, which is a critical step towards adaptive immunity.[3-4] The very first step of T cell response is the interaction between the T cell receptor (TCR) on the T cell and peptide-major histocompatibility complex (pMHC) presented on most cell types (**Figure 1.1)**. There are two classes of MHC complexes–class I MHC that presents peptides that are 8-12 amino acid long, and class II which binds peptides with lengths of 15-24 amino acid residues.[5] These MHC complexes differ in structure, origin and expression pattern that collectively define the diverse functional roles of T cells. For instances, cytotoxic T cells ($CD8^+$ T cells) interacts with class I pMHC on target cells (e.g. infected cells or cancer cells) and this interaction in turn triggers the release of cytotoxic granules leading to programmed cell death,[6] while helper T cells ($CD4^+$ T cells) recognize class II pMHC molecules on the surface of professional antigen presenting cells (e.g. dendritic cells, macrophages and B cells) and secrets cytokines that modulate the function of other immune cells.[7]

The TCR is a multi-subunit receptor complex that contains αβ heterodimer that has no intrinsic signaling domain, and CD3γ, CD3δ, CD3ε and TCRζ subunits that contain immunoreceptor tyrosine-based activation motif (ITAM) in their cytoplasmic tails (**Figure 1.1**),[8-10] and the ITAMs are the functional units that facilitate T cell signaling. At the molecular level, recognition of the agonist pMHC complex by the TCR induces the phosphorylation of the ITAMs by two protein tyrosine kinases Lck and ZAP-70. This initial event triggers a cascade of

biochemical signaling that induces elevation in intracellular Ca^{2+} and ultimately activates the effector function of T cells such as cytokine generation, target cell killing and generation of memory response depending on the phenotypes of T cells (**Figure 1.2**).[11]

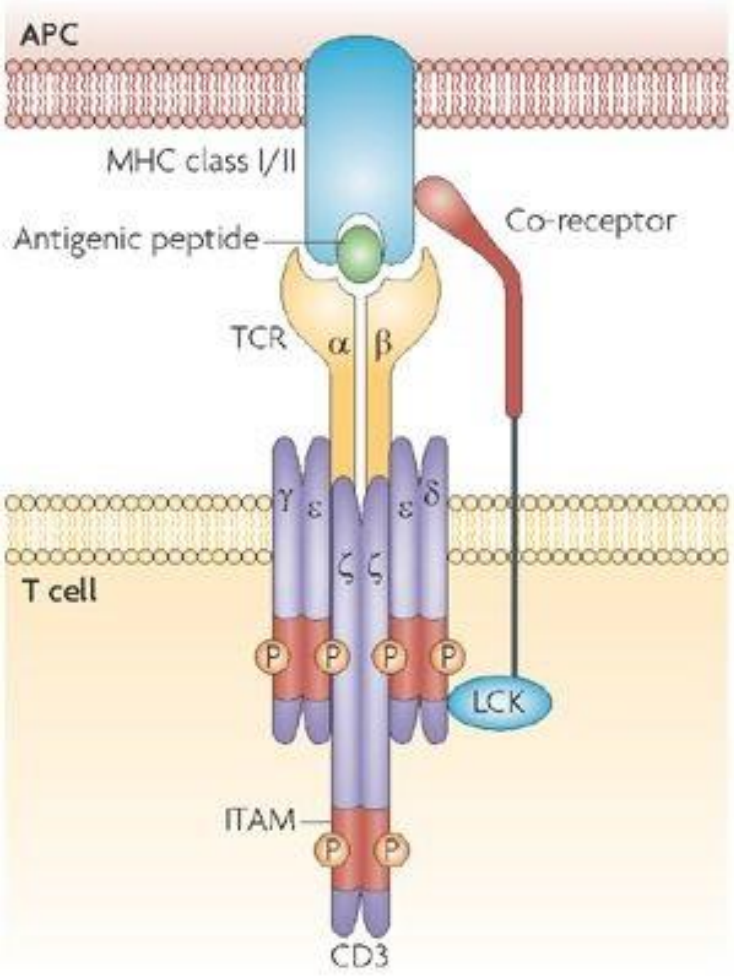

Figure 1.1. Cartoon structure of a TCR-pMHC complex. TCR subunits buried within the cytoplasmic domain have multiple tyrosine residues that can be phosphorylated upon TCR-pMHC binding. Reprinted from reference 10 with the permission of the publisher.

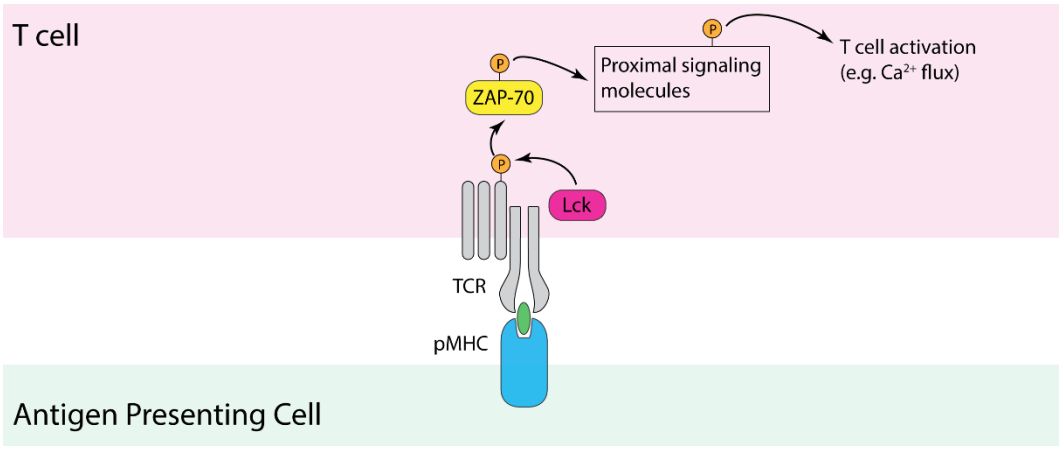

Figure 1.2. Simplified T cell biochemical signaling cascade. Binding of TCR to antigen triggers a series of phosphorylation events that ultimately activate T cells. The two key kinases are highlighted.

So how does pMHC binding change the TCR/CD3 complex to a state that facilitates phosphorylation of the ITAM domains of CD3? There are a number of unusual features that makes TCR unique compared to other surface receptors. Firstly, TCR-antigen recognition is exquisitely sensitive and selective. APCs and targets cells generally present an exceptional low amount of the agonist antigen within a sea of "self" peptides, which do not trigger T cell activation. In addition, a specific TCR on a T cell is programmed to response to a small subset of the "agonist" pMHC molecules. To avoid autoimmunity, T cells mush discriminate foreign pMHC from self-pMHC with exceptionally high sensitivity. Indeed, early work from Davis and coworkers demonstrated that a single antigenic-MHC on APC surfaces can trigger T cell activation, but the molecular mechanism remains unclear. Secondly, the TCR-agonist antigen bond is relatively weak (K_d = ~μM)[12] compared to other receptor-ligand interactions, but still this interaction can elicit a potent immune response. However, "self" pMHC complexes also bind to the TCRs with similar affinity, but this interaction does not lead to T cell triggering.[13] Lastly, TCR

can recognize multiple ligands with a range of affinities and generate differential T cell responses. For instance, a single substitution of amino acid on foreign antigen, termed altered peptide ligand, can generate a wide range of responses from full activation to weak activation.[14-15] In order to account for these exceptional usual features, a number of models of TCR triggering has been proposed involving receptor aggregation, receptor conformational change and spatial segregation of the TCRs (**Figure 1.3**). Still, none of them provides a full picture of T cell activation.[16]

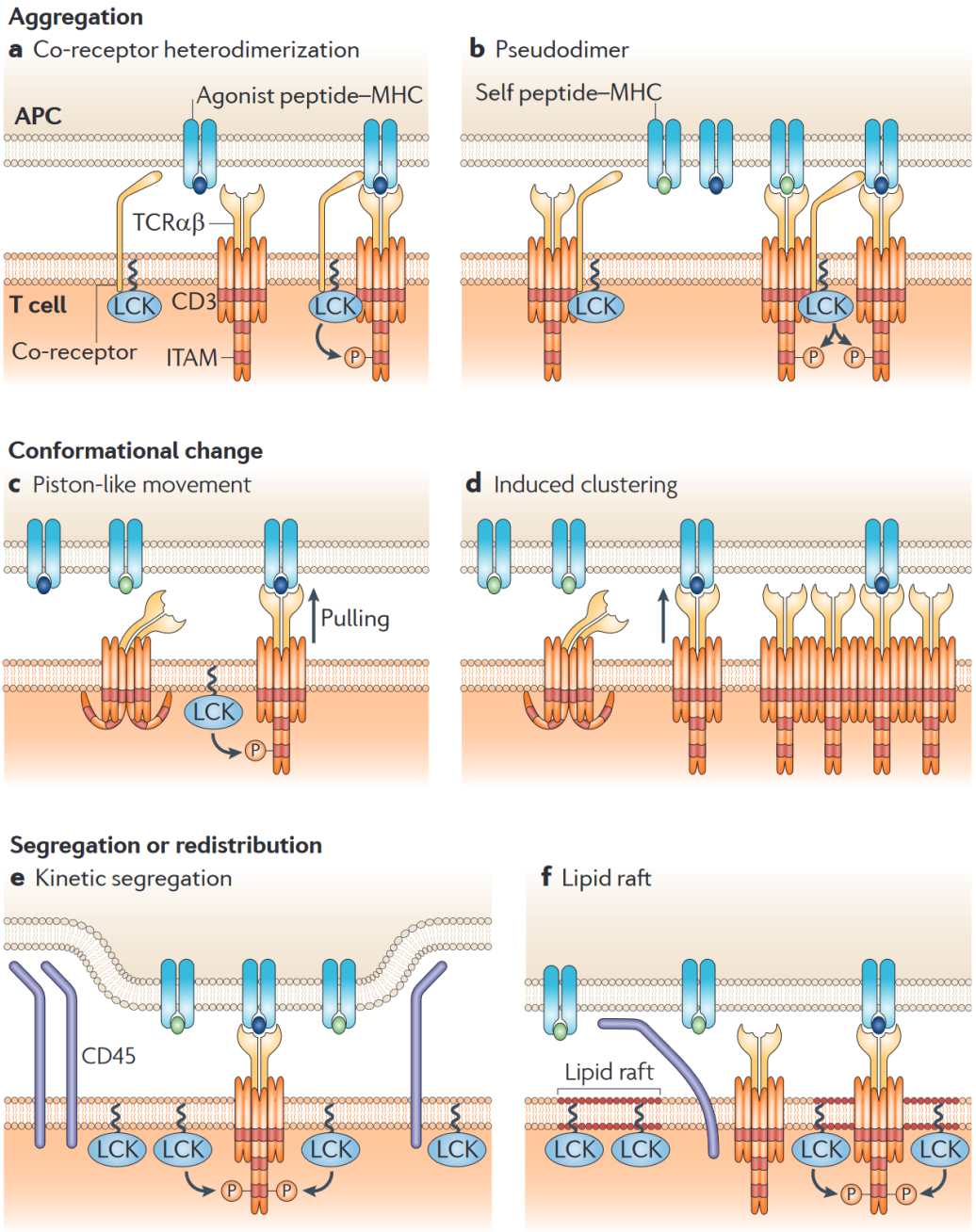

Figure 1.3. Proposed TCR triggering mechanisms. These classical proposed mechanisms can be classified into three groups based on the nature of interactions. **A) and B)** In the aggregation models, TCR-pMHC engagement recruits CD4/CD8 co-receptor that phosphorylates ITAMs. **C and D)** Conformation changes models postulate TCR-pMHC interaction triggers a structural switching of the TCR ectodomain and that exposes the cytoplasmic ITAMs for kinase phosphorylation. **E and F)** Kinetic segregation models propose formation of TCR-pMHC clusters segregates inhibitory tyrosine phosphatase or partition into lipid raft enriched with Lck. These two scenarios lead to a shift in overall phosphorylation level of ITAMs. Reprinted from reference 16 with the permission of the publisher.

1.2. Signal regulation by LFA-1 adhesion receptor on T cell membrane

Beyond initial TCR-antigen recognition, the receptor-ligand pairs within the contact zone between a T cell and an APC will physically remodel to form the immunological synapse (IS),[17-19] which is a key regulator of T cell signaling. Within minutes of contacts, the TCR along with adhesion molecules and co-stimulatory receptors form signaling microclusters that eventually segregated into distinct zones: a central zone that contains TCR-antigen is defined as central supramolecular activation cluster (cSMAC), a peripheral zone (pSMAC) that surrounds the cSMAC and is occupied by adhesion molecules and an outer zone (dSMAC) that contains bulky molecules such as CD43, 44 and 45 (**Figure 1.4**). Interestingly, it has been shown that altering the surface architecture within the IS with micropatterned substrates changes the T cell signaling such as Ca^{2+} activation and phosphorylation events,[20] highlighting formation of such a structure may be a regulatory mechanism to prevent over-activation of T cells.

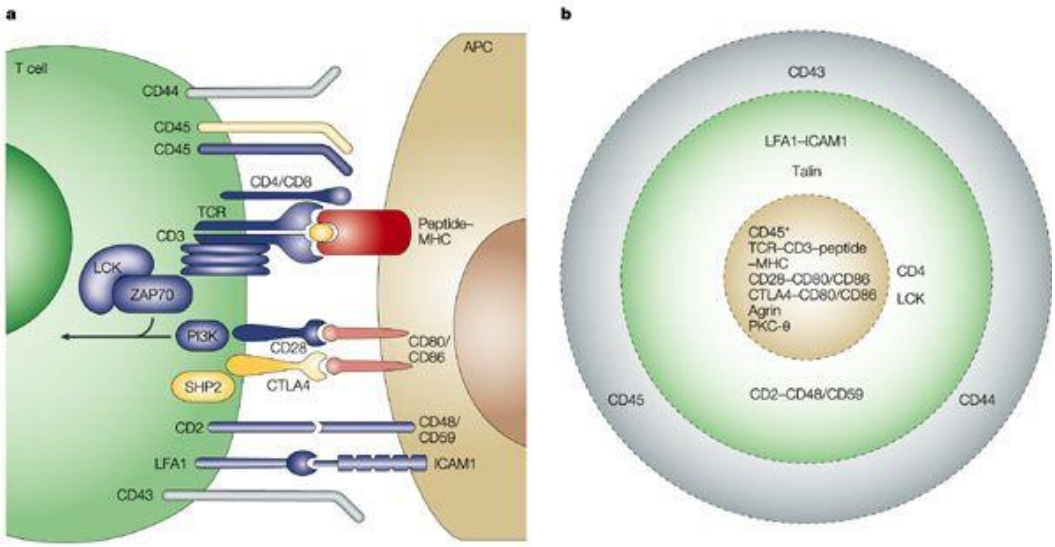

Figure 1.4. Architecture of the immunological synapse. A) Key receptor-ligand complexes formed at the T cell-APC junction collectively define the strength of T cell activation. **B)** "Bull-eye" immunological synapse with defined organization of receptors: A central zone with TCR-pMHC complexes and co-stimulating receptors; a peripheral zone with LFA-1-ICAM-1 and other adhesion complexes; and a distal zone with inhibitory receptors. Reprinted from reference 18 with the permission of the publisher.

The key molecule in the pSMAC is the T cell's LFA-1 integrin receptor, which binds to ICAM-1 ligands on the APCs.[21] LFA-1 consists of a α_L and a β_2 subunit and this structure can adopt at least three distinct conformational states: namely bent, extended, and extended open state (**Figure 1.3**)–all of them have different binding affinity towards the ICAM-1 molecule.[22] Low affinity LFA-1 assumes a bent state in which the extracellular headpiece is compact and bent. Conversion of low affinity LFA-1 to its extended or extended open state is achieved by "headpiece" opening, by which the extracellular ligand binding site is exposed making it accessible to ICAM-1 binding.[23-24] The low affinity LFA-1 can be activated by two distinct signaling mechanisms called "inside-out" and "outside-in" signaling.[25] In "inside-out" signaling, intracellular signaling cascade initiated by chemokine or TCR triggers the upregulation, clustering and headpiece opening of LFA-1. In "outside-in" signaling, LFA-1 can bind directly to the surface-immobilized ICAM in the presence of divalent cations (such as Mg^{2+}/EGTA) and signals directly. This could be explained by the fact that there could be a small fraction of LFAs that exist in extended state in resting cells. The divalent cation has a role of increasing affinity of LFA-1 for ICAM-1 by stabilizing the receptor-ligand interface, but it cannot induce receptor upregulation and clustering.

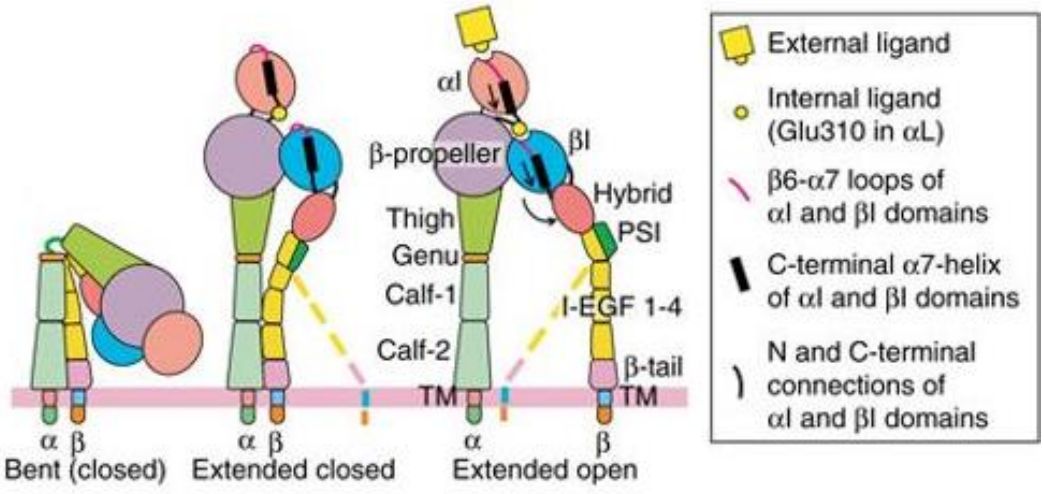

Figure 1.5. Integrin structure and conformational states. Typical integrin structures can form at least three conformational states. Reprinted from reference 71 with the permission of the publisher.

LFA-1 is historically recognized as a pure adhesion receptor that mediates formation of a stable IS to prolong the dwell time (and hence the signaling) of TCR-antigen complexes.[17] It is now increasingly appreciated that LFA-1, similar to other integrins, can trigger biochemical signaling to regulate T cell function that depends on distinct combinations of signals and the cytokine milieu.[26] A number of signaling proteins and transcription factors are directly associated to the LFA-1 receptor when LFA-1-ICAM-1 interaction occurs, and this leads to significant modeling of the transcription program to fine-tune the effector functions of T cells.[27-28]

1.3. Role of mechanical forces in T cell activation

T cell activation can also be modulated by the mechanical cues in their surrounding microenvironment, such as the stiffness of the opposing cell. This idea

is stemmed from the studies that showed T cells modulate their functions based on the rigidity of the interacting substrate presenting the cognate antigen. In one example, Milone and co-workers demonstrated that soft silicone elastomer (with Young's modulus < 100 kPa) can induce 4-fold increase in cytokine production and better proliferative response compared to T cells that were cultured on stiff substrates.[29] In another example, Hivorz and colleagues explored lower range of substrate stiffness (0.5–100 kPa) and their results showed that T cells' metabolic properties and cell cycle progression are linearly dependent on substrate stiffness within this range.[30] In the last example, Huse and co-workers revealed that the killing response of cytotoxic T cells – release of cytotoxic granules to lyse their target – is potentiated by the stiffness of the opposing target cells.[31]

Based on these observations, a number of questions pertaining to T cell mechano-sensitivity arise: Do T cells use mechanical forces to recognize the "correct" antigens? Do the TCR and LFA-1 (and other co-receptors) mechanically communicates with the TCR to fine-tune T cell signaling and function? In attempt to answer the first question, a number of research groups employed force spectroscopy to reveal that TCR functions as an mechanosensor. This hypothesis is first experimentally supported by Reinherz, Lang and colleagues.[32] In this early work, the authors used CD3ε coated bead that was manipulated by an optical tweezer (OTs), and they showed a tangential force of ~50 pN applied on the TCR via OTs were able to induce Ca^{2+} flux. The concept of mechanical triggering of T cells has been tested with other single molecule experiments. For example, Lang and colleagues showed that the TCR undergoes significant extension (~10-20 nm)

in response to pN forces generated by OTs, and the structural switching is related to the specificity of the TCR-pMHC interaction.[33] In another work, Butte and co-workers demonstrated using atomic force microscopy (AFM) that an intact cytoskeletal network is required for TCR force generation, and also T cell activation.[31] Interestingly, application of external cyclic forces to the TCR-ligand complex could re-activate the cell signaling even when the cytoskeleton was crippled.

In addition to the abovementioned examples, another important discovery in this area made by Evavold, Zhu and co-workers is that TCR forms ligand-induced "catch bonds", where the bond lifetime between TCR and antigen is lengthened with increasing magnitude of the applied force.[34] This is characteristically different than most non-covalent receptor-ligand interactions that form "slip bonds", where the bond dissociation lifetime decreases with increasing magnitude of the applied force. In this seminal study, the authors demonstrated that application of external forces in the ranges of 10-20 pN prolonged the TCR-agonist pMHC bond lifetime, while the TCR formed slip bonds with the non-agonist or partial agonist pMHC. This observation leads to a speculation that T cells could generate pN forces to mechanically select the agonist pMHC from a sea of antigens.

Nonetheless, there are inherent drawbacks of these single molecule force spectroscopy experiments. Firstly, these measurements failed to consider the role of co-receptor engagement (e.g. LFA-1-ICAM-1 interactions) which is typically ignored from these assays. Secondly, these assays require an experimenter to pull on the TCR-antigen complex with a specific loading rate, whether the T cell

receptor and other co-receptors transmit intrinsic forces to cognate antigens when encountering the APC in intracellular environment, and whether the forces have specific functions in initial antigen recognition, TCR signal amplification and long term biological functions is unknown. Therefore, sensitive biophysical assays to measure force transmission across these receptors, and also tools that can be used to study how forces modulate T cell signaling and responses are needed.

1.4. A succinct overview justifying the need to study mechanotransduction of cells

Living systems are exquisitely sensitive to mechanical cues that influence a broad range of processes such as biofilm formation,[35] embryonic development,[36] immune response,[37] wound healing,[38] cell proliferation and differentiation.[39] Akin to the biochemical exchange of information, mechanical interactions constantly and dynamically occur among neighboring cells or between cells and their extracellular matrix (ECM).[40] Therefore, it is not surprising that almost all cells have evolved the ability to detect and convert mechanical information into biochemical signals, a process widely known as mechanotransduction. The roots of this idea that physical forces influence biology were initially conceptualized by the Scottish Zoologist D'Arcy Thompson in his seminal work "*On growth and form*" more than a century ago.[41] This theoretical work generated much interest, but there was little progress in the field for many decades. This is because researchers lacked the technologies to *measure* the miniscule forces applied by cells, let alone single molecules, which hindered further progress in mechanobiology.

Nowadays, it is well known that the cellular cytoskeleton is the main force generating machinery that gives a cell its form and structure. Force generation is driven by the collective activity of motor proteins acting on the filamentous scaffolds of actin and microtubules. Given that a cell is constantly sensing the mechanical properties of its external environment, many mechanotransduction processes are mediated by cell surface receptors and interacting with the cytoskeletons. For example, integrins are a class of heterodimeric αβ transmembrane receptors that spontaneously assemble into a supramolecular assembly called focal adhesions (FAs) and transmit cellular forces bi-directionally to their ECM.[42] Several other surface receptors, such as cadherins,[43] T or B cell receptors,[44-45] Notch[46] and many receptor tyrosine kinases (RTKs)[47] also transmit forces to their cognate ligands and their activation pathways are mechanosensitive. In the past three decades, a number of innovative techniques have been developed for measuring forces in living cells, and these techniques transformed our understanding of mechanobiology (**Figure 1.6**).[48] The following sections give a brief account of these major techniques that are routinely employed in the field.

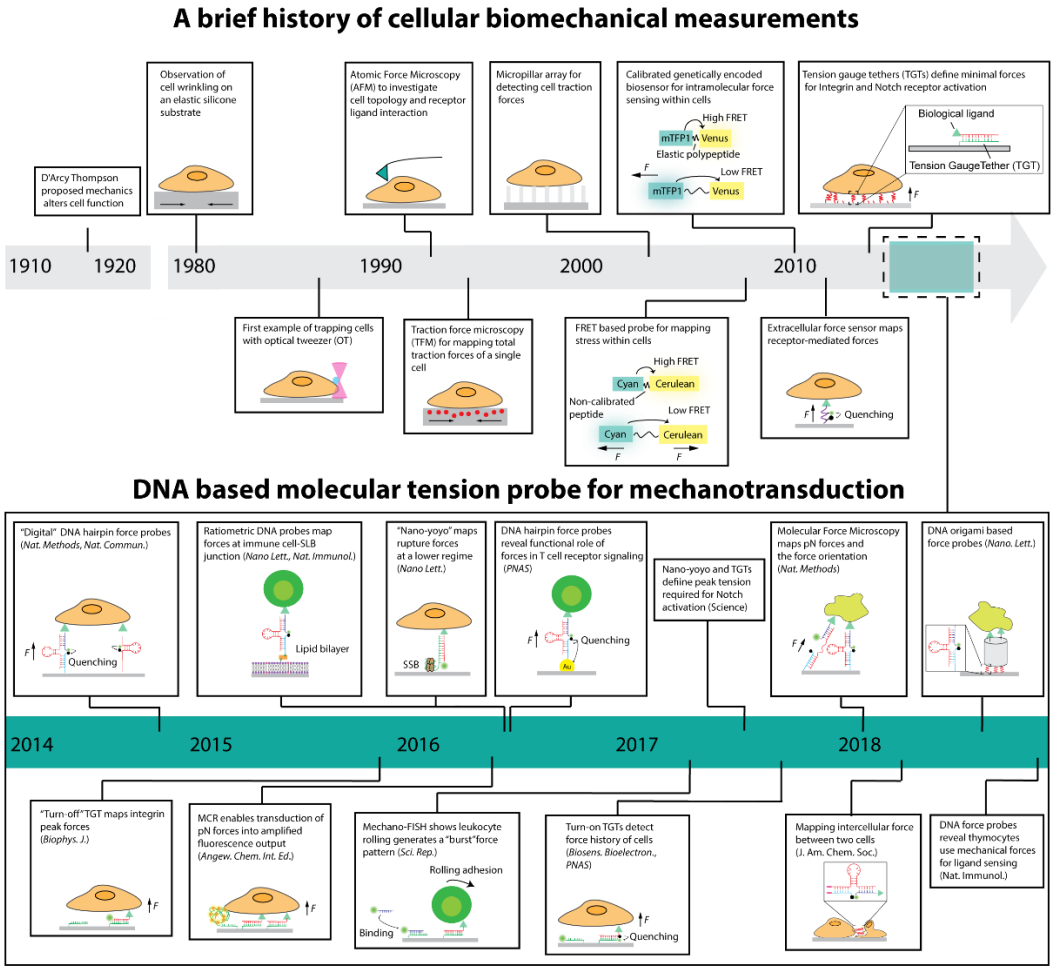

Figure 1.6. Available tools to study cellular mechanotransduction. Timeline of cellular biomechanical measurements (grey arrow) with a focus on the recent development of DNA-based force sensors (green line). Reprinted from reference 48 with the permission of the publisher.

1.5. Traditional methods to measure cellular forces

The first and a key development of a method to qualitatively "measure" forces occurred in 1980, where Harris and colleagues discovered that cells generate "wrinkles" on a silicone polymer substrate under light microscopy.[49] While this study strongly suggested that cells generate pulling forces on a substrate, the quantification of cell forces was very crude and preliminary. Subsequently, this observation led to the development of more quantitative methods such as traction

force microscopy (TFM)[50-54] and micropillar arrays[55-57] that measure polymer deformations to map cellular traction stresses (**Equation 1**).

$$Stress = \frac{F}{A} \quad (1)$$

where F = force and A = cross-sectional area

Particularly, TFM has gained wide adoption by the mechanobiology community because of its ease of use and longstanding history. TFM relies on plating cells onto elastic polymer substrates that are doped with fluorescent particles such that particle displacements can be used to computationally infer the stresses experienced by the polymer film. One issue in TFM is that quantifying substrate deformation is an indirect measurement of receptor forces, and the crosslinked nature of the polymer limits TFM's spatial (~μm) and force resolution (~nN).

In contrast to TFM, single molecule force spectroscopy (SMFS) methods such as AFM, OT, magnetic tweezer (MT) and bio-membrane force probe (BFP) detect pN forces exerted by individual cell surface molecules.[58] These methods are generally used to determine the threshold force that leads to ligand-receptor bond dissociation.[59] In other implementations, single molecule methods can be used to measure the forces transmitted by a cell to its receptor upon engaging of a ligand.[60-61] While these methods have transformed our understanding of the single molecule biophysics of cell surface receptors, their serial nature – interrogating one molecule

at a time – is not compatible with the dynamics of living systems where groups of homo- and hetero- receptors are typically engaged to trigger signaling events.

1.6. Molecular methods to measure cellular forces

It is widely recognized that mechanical forces underpin many of the molecular processes that maintain life. For example, protein cargo transport, translation, and transcription require spatially and temporally coordinated forces at the pN scale.[62-64] Many structural proteins regulate their activities under forces, where their cryptic signaling motifs are exposed in respond to molecular forces.[65] These forces are particularly hard to be measured by the traditional techniques either limited by their resolutions or compatibility.

Motivated by this technological gap, a number of recent advances have been made attempting to map these tiny molecular forces within or outside the cells. Many of these studies harnessed fluorescence resonance energy transfer (FRET) as a force reporter, where a pair of fluorescent dyes is flanked in between the two ends of a "molecular spring" composed of either a synthetic polymer, such as polyethylene glycol, or a biopolymer, such as polypeptides and nucleic acids. These approaches can be classified into three categories based on their behaviors in response to molecular forces, which are: reversible analog probes (Chapter 1.6.1), reversible digital probes (Chapter 1.6.2), and irreversible digital probes (Chapter 1.6.3).

1.6.1. Reversible analog probes

The reversible analog probes are composed of a spring that adopt random conformations at zero force.[66] Extension of these entropic springs yield an "analog" response to forces, where their extension proportionally responds to the magnitude of applied force. For polymers such as polyethylene glycol (PEG), it has been both theoretically and experimentally shown that the force-extension curve of these springs simply follows the worm-like chain (WLC) model (**Equation 2**),[67]

$$F = \frac{k_B T}{P}\left\{\frac{1}{4}\left(1 - \frac{x}{L_0}\right)^{-2} - \frac{1}{4} + \frac{x}{L_0}\right\} \quad (2)$$

where, k_B is Boltzmann constant; T is temperature; P, L_0 and x are the persistence length, contour length and the extension of the polymer chain, respectively. Based on this relationship, the dynamic force range of PEG-based springs solely depends on the contour length (L_0) of the polymer (*i.e.* M_w of polymer) and the forces experienced by these polymers can be estimated by measuring their extension (x).

A major breakthrough, reported just under a decade ago, was the development of a genetically encoded tension sensor (Tsmod) that maps the force transmission across the FA protein vinculin. In this method, Schwartz and co-workers separated the head and tail domain of vinculin molecule with a 40-amino acid elastic polypeptide commonly found from spider silk. Fluorescent proteins were engineered at each end of the polypeptide, and the efficiency of FRET reports the relative tension transmitted across the vinculin molecules (**Figure 1.7**). This study revealed that vinculin molecules experience an average force of ~2.5 pN within the FA, and the tension is highly dependent on the cell adhesion state.[68] The author

observed that highest tension was exclusively observed in assembling FA, which strongly suggests mechanical force plays a role in stabilizing FA in adhering fibroblast.

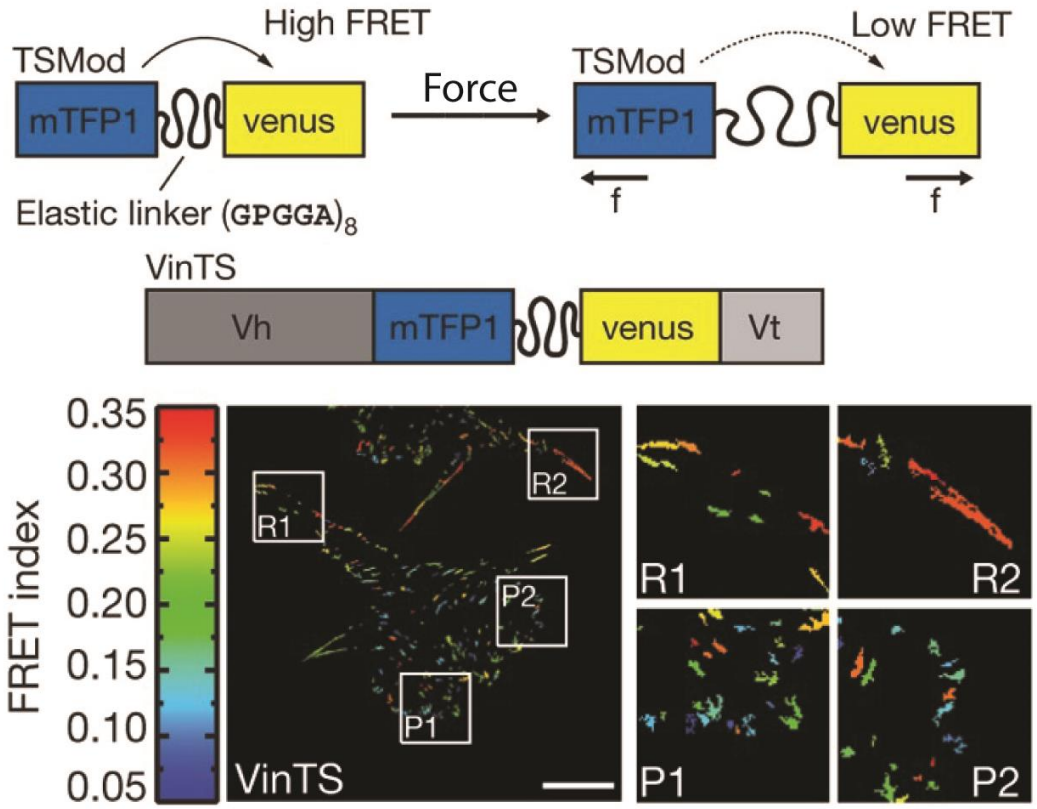

Figure 1.7. TsMod to study force transmission within the cells. Genetically encoded sensor maps force transmission across vinculin molecules within FA complexes. Reprinted from reference 68 with the permission of the publisher.

The development of TSmod has opened a new avenue to study the role of mechanics in contact dependent signaling. For instance, Dunn and co-workers generated E-cadherin tension sensing module that allowed for qualifying pN forces transmitted between the transmembrane domain and the catenin-binding domain of MDCK epithelial cells (**Figure 1.8A**).[69] Using this construct, the authors showed the cytoplasmic domain of E-cadherin is subjected to tension generated by

actomyosin cytoskeleton, regardless at the cell–cell contacts or the contact-free membranes, where cell-cell adhesion are not found. Schwartz and colleagues developed genetically encoded tension sensors for VE-cadherin and PECAM-1, which are mechanosensory complexes formed at the endothelial cell junctions, and studied how the forces across these protein complexes change in response to fluid shear stress.[70] In a normal culture condition, VE-cadherin was under substantial myosin-dependent tension while PECAM-1 had no detectable force. While shear flow induces the coupling of vimentin to PECAM-1 and leads to generation of forces across PECAM-1 and downstream biochemical signaling. Interestingly, the tension of VE-cadherin and PECAM-1 is not intimately linked. Vimentin knockdown only blocked the tension transmitted across PECAM-1 but not VE-cadherin, indicating that PECAM-1 is a shear stress mechanosensor (**Figure 1.8B**). Recently, Nordenfelt, Springer and colleague engineered a genetically encoded LFA-1 sensor in Jurkat lymphoblasts and showed that LFA-1 integrin experienced low pN tension during migration.[71] Additionally, they demonstrated actin engagement generates tension on LFA-1 β_2 subunit and this force induced and stabilized the active conformational state of LFA-1, which allows for high affinity binding to its cognate ligand ICAM-1.

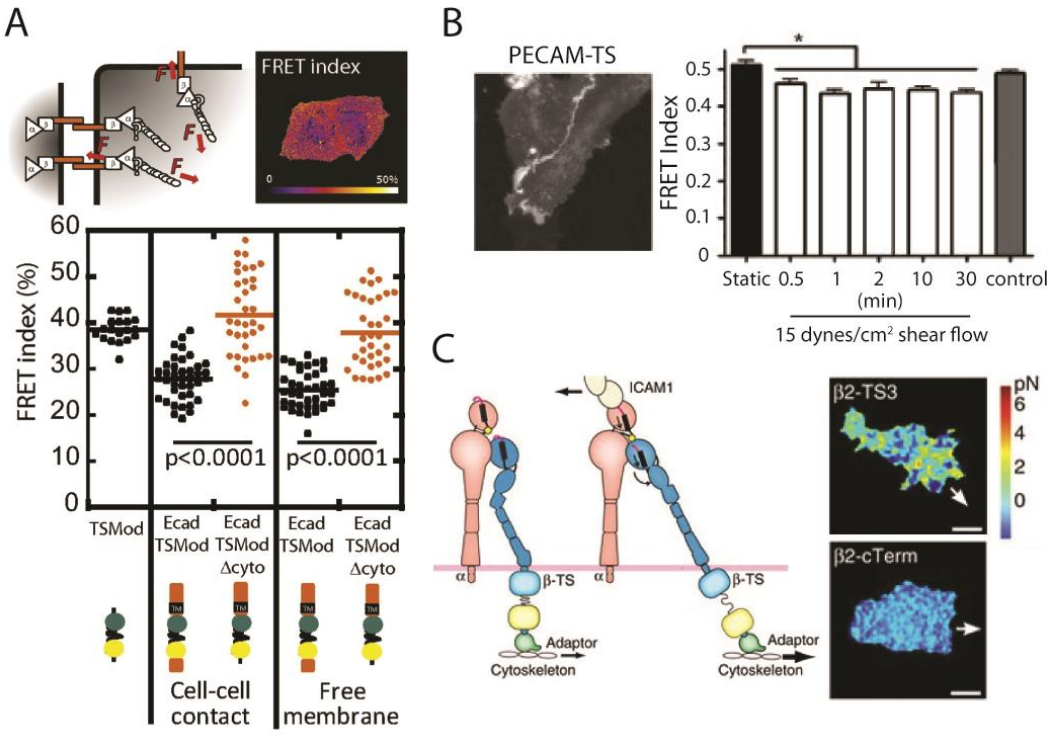

Figure 1.8. Other examples that used TsMod to study force transmission within cells. A) E-cadherin generated intracellular forces at the junction of epithelial cells. **B)** PECAM-1 is a shear stress mechanosensor where application of shear flow triggers TsMod unfolding. **C)** LFA-1 transmits low pN forces during migration. Reprinted from references 69-71 with the permission of the publisher.

While Tsmod is powerful in mapping intracellular molecular forces, it suffers from several drawbacks. For example, relatively large fluorescent proteins are used for the TsMod, which limits its dynamic force range resulting from poor resting FRET efficiency. The dynamic force range is additionally limited by the choices of short, random coiled polypeptides that are well characterized by SMFS. To alleviate some of these problems, our group reported surface the development of extracellular force sensors that are able to map receptor forces in real time. As a proof-of-concept demonstration, we constructed a reversible analog probe that consists of an extendable polyethylene glycol spring flanked by a pair of small

molecule dye-quencher. This probe was immobilized on a glass coverslip by biotin-streptavidin interaction and was used to map the endocytic forces of epidermal growth factor receptor (EGFR) upon interacting with its ligand presented on the probe (**Figure 1.9A**).[72] This representative system has been further refined to study mechano-chemical signaling of integrins. For instance, our group reported integrin receptors could transmit force up to ~15 pN to their cognate extracellular matrix ligands using a PEG-based analog force probe (**Figure 1.9B**).[73] Dunn and co-workers generated a polypeptide-based analog probe and reported most integrins only transmit 1-2 pN force within the FA (**Figure 1.9C**).[74-75] Although these probes are powerful to report force magnitude in continuum, estimating single receptor forces with these analog sensors is challenging. This is because the ensemble fluorescence signal generated by analogue probes is difficult to interpret. For instance, the measured signal may be produced by very few receptors bearing large forces, or many of receptors that generate comparatively low force and these scenarios are degenerate. This issue can be potentially be resolved using single molecule fluorescence techniques. That said, single molecule imaging conditions require oxygen scavengers and high concentrations of reducing agents which are relatively toxic to cells.

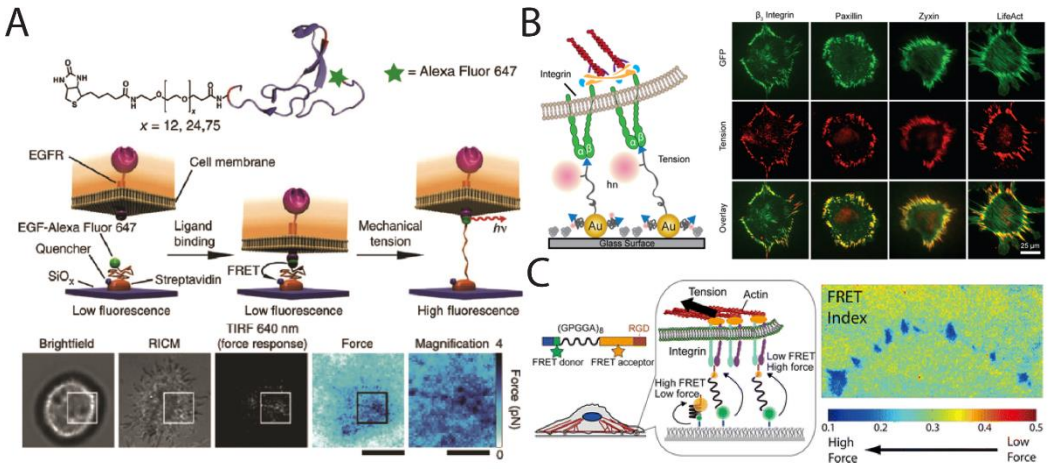

Figure 1.9. **Examples of PEG-based tension probes that exhibit reversible analog response. A)** EGFR generates pN forces during endocytosis of its cognate ligand presented on the probe. **B)** PEG-based tension probes report pN force transmitted by integrins and the forces were colocalized with adaptor proteins found in FA complexes. **C)** Polypeptide-based tension probes also showed integrins generated pN force within the FA complexes. Reprinted from references 72-74 with the permission of the publisher.

1.6.2. Reversible digital probes

The aforementioned concern warrants the development of more sensitive force probes that produce a "digital" signal (*i.e.* all-or-none) in respond to forces. This can be achieved using nucleic acids that form simple second structures, such as hairpin stem-loop (**Figure 1.10A**). It has been experimentally shown that the structural transition of a hairpin molecule only occurs at a very narrow range of applied forces, because the force-induced unfolding of this structure is highly cooperative. For simple hairpin structures with short stem-loop regions, one can assume that they adopt two-state transitions – folded and unfolded states with an energy difference separated by an activation barrier.[76] The mechanical stability of the hairpin ($F_{1/2}$) is defined by ΔG_{fold} and $\Delta G_{stretch}$, as shown in **Equation 3**.

$$F_{1/2} = \frac{(\Delta G_{unfold} + \Delta G_{stretch})}{\Delta x} \quad (3)$$

where $F_{1/2}$ of hairpin is the equilibrium force required to drive hairpin unfolding with 50% probability, ΔG_{unfold} is the free energy of DNA hybridization of the hairpin structure at zero force, $\Delta G_{stretch}$ is the free energy to stretch the hairpin structure upon unfolding (**Equation 4**) and Δx is the opening distance of hairpin from folded state to unfolded state typically identified from the correpsonding force-extension curve, or estimated using countour length per DNA nucleotide = 0.44 ± 0.02 nm, plus a correction term called "effective helix width" of 2.0 nm.[76]

$$\Delta G_{stretch} = \left(\frac{k_b T}{L_p}\right)\left[\frac{L_o}{4(\frac{1-x}{L_o})}\right]\left[3(\frac{x}{L_o})^2 - 2(\frac{x}{L_o})^3\right] \quad (4)$$

where k_b is the Boltzmann constant, T is the temperature, L_p is the persistence length and L_0 is the contour length of ssDNA, x is the hairpin extension from equilibrium

ΔG_{unfold} is an intrinsic thermodynamic property of folded DNA hairpins dictated by the free energy of collective base-pair stacking and hydrogen bonding. As illustrated in **Figure 1.10B**, increasing the guanine-cytosine (GC) content within the stem region of hairpin structures while keeping the stem-length constant increases the ΔG_{unfold} and also the $F_{1/2}$. This is because GC base pairs have higher thermostability than that of adenine and thymine base pairs (more negative ΔG).

Free energy of stretching ($\Delta G_{stretch}$) also has a role in modulating the $F_{1/2}$ of a hairpin. Considering an external force applied to unfold the hairpin, the base pairs in the helix are forced to "unzip" instantaneously producing a ssDNA region. The

nucleotides in this region and the loop are mechanically stretched behaving like an "entropic spring". Total extension of this ssDNA region is assumed to follow the worm-like chain (WLC) model, which describes force as a function of the molecular extension of the unfolded hairpin. This means that increasing the stem-loop length of the hairpin has a collective effect in modulating the ΔG_{unfold}, as more base pairs can be formed, and the $\Delta G_{stretch}$, which is dictated by the contour length of the hairpin stem-loop. The $F_{1/2}$ of most of the reported hairpins can span from a few pN up to ~20 pN (**Table 1.1**). At the low end of the range (~2−3 pN), the hairpins have higher probability to undergo thermally-induced unfolding and thus are less suitable for cell force measurements. In contrast, hairpins are rarely found to have $F_{1/2}$ value greater than 20 pN because the free energy of hybridization provides diminishing returns for longer stem regions. This defines the range of forces that are detectable by conventional hairpin probes.

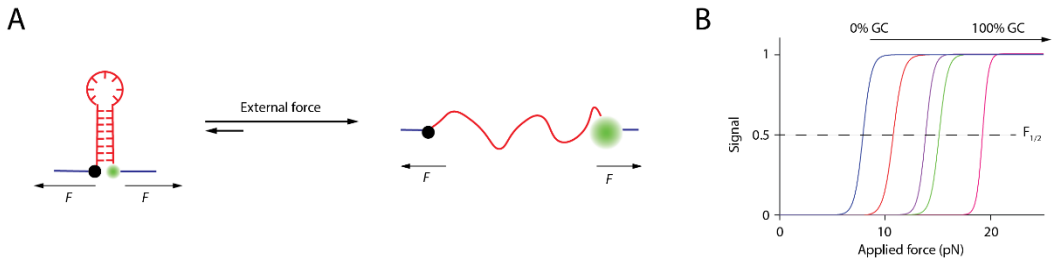

Figure 1.10. Mechanical stability of DNA hairpin structures. A) Mechanical unfolding of stem-loop region of a DNA-based force probe. **B)** Theoretical plot showing unfolding of DNA hairpin structures with the same length. Dashed black line indicates 50% expected increase in fluorescence signal at a force defined as $F_{1/2}$. Increasing GC content in the stem-loop structure increases $F_{1/2}$ of the hairpin structure. Reprinted from reference 48 with the permission of the publisher.

Table 1. Representative thermodynamic and mechanical parameter of hairpin structures used to construct DNA hairpin-based force probes.

GC content [%]	Stem size [bp]	Loop Size [nt]	ΔG_{fold} at 25 °C [kJ/mol][a]	Calc. $F_{1/2}$ at 25°C [pN][b]	ΔG_{fold} at 37 °C [kJ/mol] [a]	Calc. $F_{1/2}$ at 37°C [pN][b]	Exp. $F_{1/2}$ (pN)
22	9	7	23.3	7.8	12.8	5.9	4.7[c]
30	10	4	33.3	10.1	22.5	8.0	8.1[d]
35	20	4	90.8	12.0	68.9	10.0	11.3[d]
77	9	7	52.3	13.6	40.6	11.3	N.D.
100	12	4	100.9	20.2	86.1	17.8	13.1[c]
100	20	4	170.5	19.8	143.9	17.4	19.3[e]

[a)] Estimated using IDT oligo-analyzer tool and only the ΔG of the most stable conformer is listed. Conditions used for the predictions: 137.3 mM NaCl, 0.8 mM $MgCl_2$;[b)] Estimated using equation 3. Persistence length of ssDNA is assumed to be 1.3 nm and contour length of ssDNA is 0.63 nm per nucleotide;[c)] Biomembrane force probe calibration at 25 °C and 137.3 mM NaCl; [d)] Optical tweezer calibration at 25 °C, and 200 mM KCl. N.D. = not determined.

Compared to the initial PEG-based molecular force probes that used an elastic (entropic) polymer as a force responsive module, dynamic nucleic acid nanostructures such as DNA hairpins are fundamentally advantageous for several reasons. First, unfolding of a simple DNA hairpin structure under forces is highly cooperative and this resembles a "digital" response. In contrast, stretching PEGs and elastic polypeptides under forces typically shows a graded "analog" response, where the extension, and hence the fluorescence due to dequenching, increases as a function of the magnitude of the externally applied forces. Second, DNA hairpin structures have a well-defined force response which is tunable by modulating the ΔG of hybridization and stretching (i.e. changing the stem length and GC content), in contrast to the force response of entropic probes which is purely dictated by the

size of the “spring”, and thus their contour length. Third, DNA synthesis is highly modular allowing a variety of functional groups to be introduced during on-column synthesis or post modification at costs that are continuously dropping. Lastly, the use of well-defined DNA structures places the fluorophore in close proximity to the quencher [quenching efficiency (QE) = ~90−95%], and this in turn generates high signal-to-background ratio when the probe is open. For reference, typical QE for a fluorophore-quencher pair in entropic-spring based force probes is ~70% at best due to their random coil structure. Overall, these advantages make DNA-based hairpin probes as promising alternatives for mapping forces in the living systems.

The first generation of DNA force sensors for cells were comprised of a surface anchoring strand labelled with a quencher, a ligand strand modified with a fluorophore and a hairpin strand complementary to the other two. In the resting state, the fluorophore and the quencher are placed in close proximity. When cell receptors recognize their cognate ligands and pull with a force larger than the $F_{1/2}$, the stem-loop structure unfolds, thus separating the fluorophore from the quencher and resulting in restoration of fluorescence emission (**Figure 1.11A**). The generated fluorescence signal indicates the location where receptors actively transmit pN forces above the $F_{1/2}$ of the hairpin. This “three-component” system is facile to prepare because each element is synthesized separately; the force response, anchoring and ligand elements are unique oligonucleotides. Using this approach, one can quickly create a library of hairpin probes with different $F_{1/2}$ values without the need for cumbersome multi-step re-synthesis and purification. Our lap

developed three-component hairpin probes to visualize mechanical forces transmitted by integrins in live cells.[77] In proof-of-concept experiments, the authors seeded cells on a substrate presenting three-component force probes. Cells recognized the Arg-Gly-Asp (RGD) peptide on the force probes and generated fluorescence signals coincident with the markers of the FA complexes (**Figure 1.11B**).

We validated the force signals using cytoskeletal inhibitors which caused cessation of fluorescence signals, suggesting probe refolding. These results showed unfolding of hairpin probes was tightly regulated by the forces transmitted via the cytoskeleton of cells. Importantly, these DNA-based force probes enabled multiplex force measurement within integrin clusters that cannot be resolved using TFM. Using spectrally encoded tension probes with different $F_{1/2}$ values (4.7 pN and 13.1 pN), we showed that forces within a single FA distributed unevenly, and a subset of integrins pulled with a force that is lower than 13.1 pN but greater than 4.7 pN. These probes have been widely used in many of the subsequently studies (including the work presented in this thesis), and helped answering many fundemental questions pertaining to platelet,[78] B cell[79] and T cell signaling.[80]

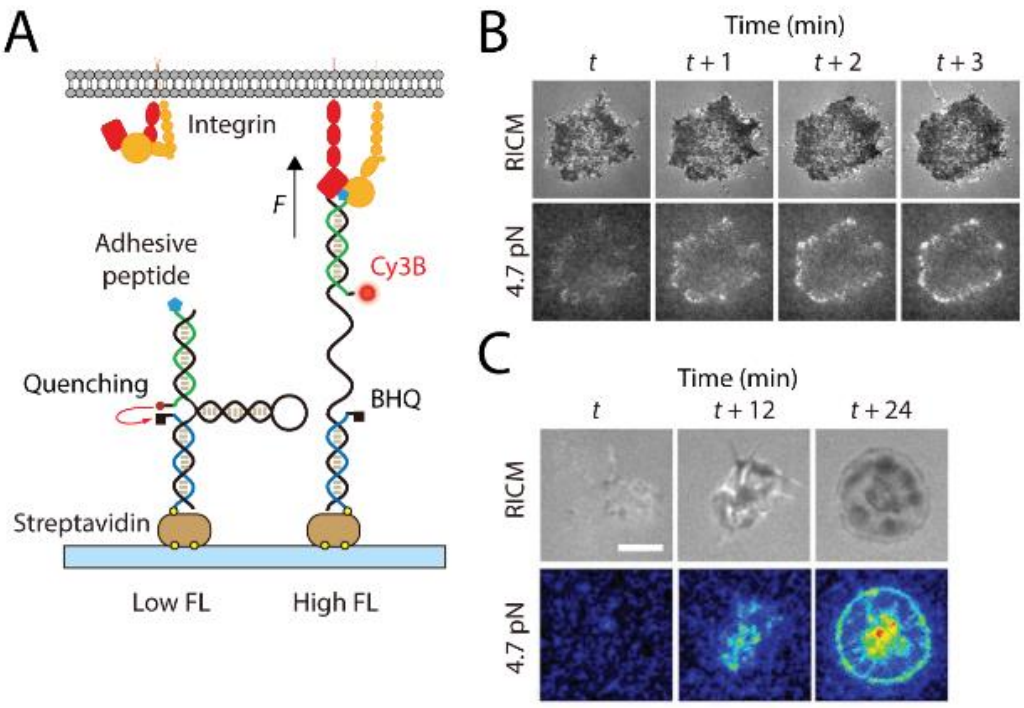

Figure 1.11. Examples of DNA hairpin-based tension probes that exhibit reversible digital reponse. A) The DNA force probe consists of three oligonucleotides to form the sensor and is immobilized on a glass surface via biotin-streptavidin interaction. This probe is decorated with a pair of fluorophore and quencher and a biological ligand to report the force-induced hairpin unfolding by a cell. **B)** Time-lapse images showing the spatiotemporal change in spreading and the force signal of a NIH-3T3 fibroblast cell. **C)** Time lapse images showing spreading of a human platelet and force signal plated on the DNA-based hairpin probe substrate. Reprinted from references 77 and 78 with the permission of the publisher.

Coincident with the work reported by our group, Chen and colleagues reported a similar method to generate DNA hairpin-based force probes.[81] In their approach, the RGD peptide ligand, fluorophore and quencher, and a reactive group for surface anchoring were installed in a single stranded oligonucleotide that forms a hairpin stem-loop. This probe was covalently grafted to a surface via thiol-maleimide coupling. Fibroblast cells were used as a model system for their study and showed similar conclusions to our work, where the fluorescence signals were

exclusively observed at the FA complexes and the force distribution by integrins was highly heterogeneous within a single FA. In comparison to our three-component DNA hairpin probe, this design is more robust, and hence it is amenable to imaging tension for longer time scales. Despite the increased potential stability, the single oligo tension probe has been rarely used in the intervening years due to the complexity of synthesis. It is because testing a range of DNA probes displaying different $F_{1/2}$ and fluorophore quencher pairs is not practical for the cell biology community that is less inclined to go through multistep synthesis and purification. Therefore, the three-component oligonucleotide design is the most widely used today.

1.6.3. Irreversible digital probes

In contrast to DNA hairpins, separating a DNA duplex under force is irreversible because of the lack of connection that holds the two strands together. Stretching the same duplex with different orientations has a drastically different outcome despite having the same thermal melting temperature (T_m) and ΔG of duplex formation. Force-dependent dissociation of duplexes can be induced by stretching it along its axis (5'-5', shearing geometry, **Figure 1.12A**) or perpendicular to its axis (5'-3', unzipping geometry, **Figure 1.12A**). Early single molecule experiments found that forces required to shear a DNA duplex linearly correlated to its length and approaches an asymptotic limit at a critical length of ~30 bp.[82] In contrast, forces required to separate duplexes in the unzipping

geometry tend to be much smaller because the external force applied is concentrated to break the nearest base pairs one by one in a stepwise fashion.[83-84]

There is rich experimental and theoretical work aimed at examining the mechanical stability of DNA duplexes in the unzipping and shearing geometry.[82, 85-89] An interesting model proposed by de Gennes[87] treats the DNA duplex as a ladder with springs connecting the nucleotides within the same strands and hydrogen bonding holds the inter-strands together. For a duplex that experiences shearing forces at both ends (5'-5'), it is hypothesized that the applied force is only distributed to a finite number of base pairs at both ends, rather than distributing evenly across the whole duplex. Based on these assumptions, the critical force, T_{tol}, required to melt 50% of the DNA duplex can be mathematically expressed as shown in **Equation 5**.

$$T_{tol} = 2f_c[x^{-1}\tanh\left(x\frac{N}{2}\right) + 1] \quad (5)$$

where f_c is the rupture force to break a single base pair (3.9 pN), $x = \sqrt{2}R/Q$ is a function describing the elasticity within the duplex – Q is a spring constant between neighbors within a strand, and R is a spring constant between base pairs in a duplex, N is number of base pairs formed within a duplex.

Alternatively, a duplex that experiences unzipping forces at the same end (5'-3') breaks readily by relatively small forces. From this model, the unzipping force required to melt a duplex is estimated to be ~12 pN.[90] For illustration, **Figure 1.12B** plots the rupture behavior of a 24 mer DNA duplex moving from an "unzipping" geometry to "shearing" geometry. χ^{-1} was experimentally determined

by single molecule pulling experiments with a "clamp" time of 2 s at room temperature. However, one caveat for this simplified model is that it does not account for the DNA duplex sequence, its GC content and more importantly, the time-dependent rate of melting as the rate of mechanical denaturation of DNA duplexes depends on the duration of the applied force. Interestingly, recent coarse-grained modeling[89] and Monte Carlo simulation[91] suggest that typical DNA duplexes used for *in vitro* experiment (N>20 bp) show weak dependence of rupture force on the duration of the applied force within biologically relevant time scales (t = ~ s to min, **Figure 1.12C**).This is predicted to hold for both the "unzipping" and "shearing" geometry. Hence, the theoretical work by de Gennes still carry relevance for cellular force measurements.

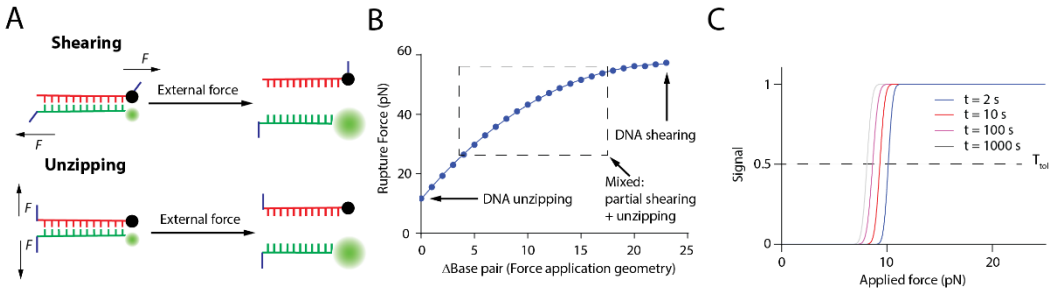

Figure 1.12 Mechanical stability of DNA duplexes. A) Rupturing of a DNA duplex with different force application geometries. **B)** Hypothetical plot showing the rupture force of a 24 mer duplex by changing the force application geometry based on the de Gennes DNA rupture model. ΔBase pair is determined by the base pair number between two force anchoring points. **C)** Theoretical plot showing unzipping of a DNA duplex as a function of the applied forces. A threshold force required to attain 50% of the fluorescence signal decreases as the force loading time increases from 2 s to 1000 s. Reprinted from reference 48 with the permission of the publisher.

The mechanical properties of DNA duplexes have been exploited as irreversible digital probes. Wang and Ha developed an approach, termed tension

gauge tether (TGT) assay for controlling the magnitude of peak tension experienced by receptors.[90] TGT is a ligand labeled DNA duplex tailored to dissociate at force levels exceeding its tension tolerance (T_{tol}). As defined in **Figure 1.12B and C**, T_{tol} of the TGTs can be fine-tuned by varying the ligand anchoring position. Receptor forces larger than the T_{tol} rupture the tether, and hence abolish mechanical signaling. In contrast, mechanical forces lower than the T_{tol} are maintained (**Figure 1.13A**). With the aim of defining the force magnitude required to activate a biophysically induced signaling cascade, Wang and Ha designed nine RGD-TGTs with T_{tol} ranging from 12-58 pN, and showed that these mechanically different, chemically identical DNA probes (with same T_m and ΔG of hybridization) had profound effects on integrin mediated mechanotransduction. They tested this system with several cell lines and concluded that a universal threshold force of ~40 pN was required for integrin mediated activation and initial cell adhesion. Interestingly, although the 43 pN TGTs supported initial cell adhesion, these cells failed to form robust FAs and stress fibers. On the other hand, cells seeded on the 56 pN TGTs allowed the formation of mature FAs and stress fibers. Therefore, they concluded that larger forces are needed for sustaining biophysical signaling of integrins. They also used this intriguing platform to test the force required for activation of Notch signaling and found that both the 12 pN and 58 pN TGTs support efficient Notch activation, suggesting Notch activation may be insensitive to mechanical forces or the activating force is below 12 pN. Since then, significant progress has been made toward developing more generalizable TGT probes for the community, including the development of protein G-TGTs to present Fc-fused functional protein ligands

with a specific conformation,[92] and the development of an easy-to-implement protocol for tethering TGT probes on regular cell culture dishes.[93]

An interesting approach to generate "turn-on" fluorescence signal resulting from bond rupture by receptor is the integrative tension sensor is the integrative tension sensor (ITS), or simply the "quantitative" TGT.[94] In this approach, the ligand presenting DNA strand is chemically coupled to a quencher while the surface anchoring strand is modified with a fluorophore and is placed in close proximity to the quencher, thereby quenching the emission of the fluorophore in the resting state. Integrin forces larger than the T_{tol} of TGT rupture the probe and remove the quencher from the surface, leading to generation of permanent "turn-on" signal (**Figure 1.13B**). Wang and co-workers[95] reported this strategy to map the traction forces generated by platelet during initial adhesion and activation. Similar to the finding using DNA-based hairpin probes,[77] platelets used two force generating machineries in mediating TGT dissociation. One exclusively located at the cell edges with forces >54 pN and weaker force >12 pN that spanned across the cell surfaces. Importantly, Wang and co-workers showed that actomyosin contraction was responsible for generating >54 pN integrin forces but not the weaker forces. In a subsequent report, Wang and co-workers used ITS to study the magnitude and spatiotemporal dynamic of the integrin forces in migrating cells.[96] Using keratocytes as a model system, the authors revealed that these cells generated forces >54 pN but <100−150 pN during rapid migration. These forces were exclusively produced at the rear margins and sides of the cells and were postulated to have a role in promoting cell rear retraction to facilitate cell migration. Unlike platelet,

immune cells and fibroblast, the source of these extremely high forces could be from actin treadmilling that stretches the cell membrane and generates a pulling force from de-adhesion rather than the actomyosin contraction.

The rupturing event of TGT can also be detected using a complementary, fluorescently labelled oligonucleotide. In one example, Chemla and co-workers used the surface immobilized single stranded DNA, resulting from TGT rupture, as a docking sequence for fluorescence in situ hybridization (FISH) (**Figure 1.13C**).[97] Here, a P-selectin ligand was chemically modified onto the TGT with T_{tol} of 12 pN to visualize the rolling adhesion of leukocytes, mediated by the PSGL receptor, under shear flow conditions. From this assay, the authors discovered a periodically patchy, yet highly asymmetrical pattern of the adhesion footprint generated by TGT rupture and the subsequent fluorescence *in situ* hybridization (FISH) probe binding, while no such patterns were formed in their control experiment where a rolling bead was used. This result suggested that the PSGL receptor on leukocytes may distribute unevenly across the whole cell surface. This feature is hard to resolve with TFM because the rolling behavior is rapid, and the rolling cell−surface contact is extremely small and approaches the spatial resolution of conventional TFM (~1 μm). In another example, we used the surface immoblized ssDNA resulting from TGT rupture as a primer sequence for amplification. This approach will be further discussed in Chapter 4.

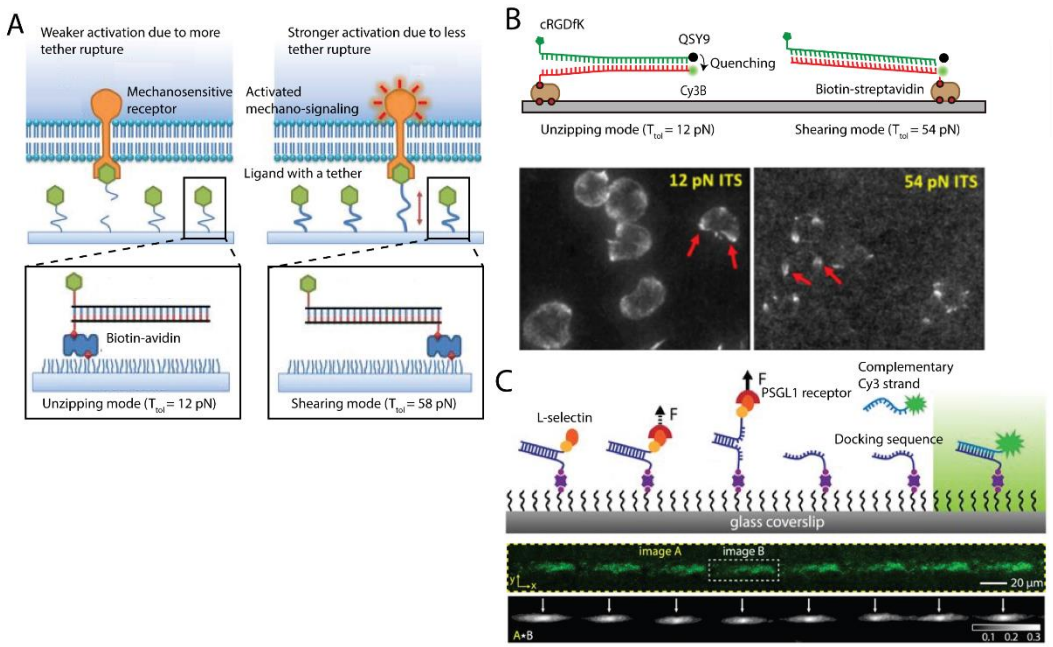

Figure 1.13. Tension gauge tether (TGT) sensors that generate irreversible analog responses. A) TGTs are rupturable DNA duplexes presenting ligands on a surface. A specific rupture force of the duplex (T_{tol}) can be estimated depending on the force application geometry. Mechanical denaturation of TGTs occurs when the receptor forces exceed the T_{tol}. The force required for cell attachment or activation can be determined using a range of TGTs with increasing T_{tol}. **B**) Quantitative TGT (ITS) consists of a pair of a fluorophore and quencher that are labelled on the TGT. Rupture of the TGT generates a permanently "turn-on" signal on the surface that can be used to track the spatial distributions of receptor forces (Top). Fluorescent imaging of mouse platelet cells reveals that these cells specifically pull with integrin forces >54 pN at the cell periphery (Bottom). **C**) FISH based TGTs utilize the exposed ssDNA strand, resulting from TGT rupture, as a docking sequence. Complementary Cy3B strand flowed into the chamber hybridizes with the docking sequence and generates a "turn-on" signal visualizable with total internal reflection fluorescence microscopy (Top). Adhesion footprint of a rolling leukocyte reveals periodicity of the rolling adhesion mediated by the PSGL1 receptors (Bottom). Reprinted from references 90, 95 and 97 with the permission of the publisher.

1.7. Thesis outline

The above sections have justified the importance of mechanical forces in T cell biology. I also have presented a brief account showcasing the development of molecular probes to study cellular mechanobiology. While reversible analog probes

(Chapter 1.6.1) have found uses in mapping the forces with high resolution, the signal resolution is inherently limited because the fluorescent signal is extremely hard to interpret due to the nature of the probes. In comparison, DNA-based force probes offer a number of significant advantages in this regard, because the fluorescent readout is digital, and the response can be easily interpreted using quantitative calibration techniques. This thesis is dedicated to push the frontier of DNA-based force probes. The use of these probes in revealing the mechanical basis of T cell signaling will be discussed in **Chapter 2 and 3**. Also, engineering strategies to improve the capability of DNA-based probes will be presented throughout the thesis.

In **Chapter 2** I will discuss the development of ratiometric tension probes that are capable of mapping TCR forces generated at the artificial cell-cell junction. First, I will discuss the synthesis and characterization of these probes in a cell free system. I will then show concurrent measurement of TCR forces and clustering during antigen encounter and subsequent long-range receptor-ligand rearrangement. Lastly, the biological importance of cytoskeleton on the TCR force transmission will be highlighted.

In **Chapter 3** I will describe the work on studying the LFA-1 adhesion receptor in T cells. The impact of lateral mobility of ICAM-1 on LFA-1 mediated adhesion and T cell signaling will be demonstrated. Then I will show the use of DNA-based force probes to directly map the forces transmitted by LFA-1 during ligand sensing, cell adhesion and migration. Lastly, I will present a novel biophysical assay to study

mechano-communication of TCR and LFA-1 and the impact of these forces on modulating T cell spreading, early signaling and late effector functions.

In **Chapter 4** I will describe the development of a novel bioanalytical assay that can catalytically amplify cellular forces into fluorescent signals. First, I will show optimization of the enzyme-mediated DNA amplification and the subsequent fluorescent detection on surfaces. Next, I will demonstrate that fibroblast cells generate significant traction forces to rupture the TGT probes, and the resulting surface anchored ssDNAs can be amplified using enzymes. Then, I will showcase the applicability of this new bioanalytical assay in screening drugs/antibodies that impair cell mechanics in both high content/throughput settings.

Chapter 2

Ratiometric Tension Probes for Mapping Receptor Forces and Clustering at Intermembrane Junctions

Adapted from **Ma, V.-P.-Y.**; Liu, Y.; Blanchfield, L.; Su, H.; Evavold, B. D. and Salaita, K. Ratiometric Tension Probes for Mapping Receptor Forces and Clustering at Intermembrane Junctions. *Nano. Lett.*, **2016**, *16*, 4552–4559

2.1 Introduction

Membrane receptors are ubiquitous in Nature and play a central role in transferring chemical information across the cell membrane.[98] The first step in the majority of signal transduction cascades, ranging from growth factor signaling[99-100] to T-cell activation,[17, 101-102] is ligand-induced dimerization and oligomerization of receptors. These higher-order clusters of receptors often function as a signaling complex for signal amplification, diversification, and in some cases serve to facilitate receptor internalization and signal degradation.[103] Interestingly, receptor oligomers are typically coupled to the cytoskeleton which offers an active scaffold for receptor translocation and organization, thus further fine-tuning signaling circuits.[104] Given the role of the cytoskeleton in force transmission and generation,[105] it seems intuitive to conclude that ligand-induced receptor clustering is intimately linked with mechanotransduction but evidence for this connection is lacking. This is due to the absence of methods to measure the mechanical forces experienced by ligand-receptor complexes during active signaling at the cell membrane.

The archetypal example highlighting the complex interplay between ligand-induced binding, receptor clustering and mechanical coupling is illustrated by the TCR.[16] A polarized and crawling T cell constantly scans the surfaces of APCs in search of foreign peptides that are bound to pMHC.[106-107] Upon TCR engagement and activation by their cognate pMHC ligand, the receptors form signaling microclusters that initiate T-cell activation cascades leading to Ca^{2+} flux and cytokine production. During activation, LFA-1 receptors bind ICAM-1 on the APC,

thus facilitating the formation of a stable intercellular junction.[104] Within this specialized junction, the T cell cytoskeleton associates with TCR and LFA-1 and sorts these receptors into distinct concentric zones. TCR microclusters undergo continuous translocation and become spatially organized in a structure known as the cSMAC, while LFA-1/ICAM-1 are re-organized into a ring-like structure surrounding the cSMAC.[17, 108]

The migratory nature of T cells and the central role of the cytoskeleton in TCR activation[109-110] suggest a fundamental connection between receptor oligomerization, signaling, and mechanotransduction. Several lines of evidence support an important role of mechanical force in T-cell activation and signaling.[111-112] First, Reinherz, Lang and co-workers showed that TCR is a mechanosensor that responds to externally applied pN forces from an optical tweezer.[32] This concept is further supported by Li and co-workers who demonstrated micropipette induced shear forces can activate T-cells,[113] and recently by and recently by our optomechanical actuator (OMA) nanoparticles which, upon stimulation of NIR light, are able to mechanically activate T-cells.[114] In addition, TCR undergoes distinct conformational transitions upon experiencing pN forces transmitted through the pMHC antigens.[33] Second, bio-membrane force probe experiments by Zhu, Evavold and colleagues showed that TCR-pMHC bond lifetime ($1/k_{off}$) is best correlated to antigen potency when 10–15 pN forces are applied to the TCR-pMHC complex.[34] Third, T-cells apply nN traction forces to deform micron-sized PDMS pillars within ~5 min of activation.[115] Lastly, restriction of TCR transport with diffusion barriers upregulates TCR signaling, possibly due the increased forces on

the TCR-pMHC complex and its altered spatial organization.[20] Still, whether the interplay of mechanics, clustering and chemical signaling influences T-cell function remains a longstanding question due to the lack of tools to quantify nanoscale mechanics of T-cells.

To investigate how physical inputs regulate or couple to signal transduction in living cells, we invented molecular tension fluorescence-based microscopy (MTFM), which maps pN receptor forces generated by cells using fluorescence imaging with high spatial (~200 nm) and temporal (~ms) resolutions.[116-117] Typically, MTFM probes consist of an extendable "spring" flanked by a fluorophore and quencher and immobilized on a surface. The probe is decorated with a ligand of interest, and is highly quenched in the resting conformation (>90% quenching efficiency). When cell surface receptors engage their ligand on the MTFM probe and apply sufficient mechanical load to extend the "spring" then the dye is de-quenched, which leads to significant enhancement in fluorescence. Second generation MTFM probes have further improved the dynamic force range,[118] sensitivity[119-120] and stability.[73-74, 121-122] We recently developed a gold nanoparticle (AuNP)-based DNA tension probe to directly image the TCR-pMHC forces on immobilized ligands and revealed that T-cells may harness mechanics for enhanced antigen sampling and discrimination.[123]

One remaining limitation for MTFM is that probes are immobilized onto a solid substrate, which is used for several reasons. First, it limits the lateral mobility of the ligand and thus the probe reports the integrated forces transmitted in the lateral and perpendicular directions through the ligand-receptor complex.

Immobilized MTFM probes provide mimics of the cell–extracellular matrix interactions, where ligands are physically affixed onto an immobile scaffold.[124] Second, by maintaining a constant probe density, the donor fluorescence intensity can be directly used to determine the quenching efficiency (QE) using the following relation (**Equation 6**):

$$QE = 1 - \left(\frac{I_{DA}}{I_D}\right) \quad (6)$$

where I_{DA} is the donor fluorescence under zero force condition and I_D is the donor fluorescence in the presence of applied forces.

In this way, a non-fluorescent acceptor (quencher) can be used, which reduces bleed-through, improves signal-to-noise ratio and also frees up additional fluorescence channels for live cell imaging of protein translocation and signaling activity. An alternate immobilization strategy would be to tether ligands onto laterally fluid surfaces mimicking the plasma membrane. In this scenario, it remains unknown whether MTFM probes on these surfaces would experience sufficient pN tension to generate detectable signal. In order to study mechanical forces at cell–cell junctions where ligands and receptors are allowed to diffuse laterally, it is necessary to introduce new methods that effectively integrate MTFM probes with fluid membranes.

One approach to mimic the cell–cell junction is the hybrid cell–supported lipid bilayer platform. The supported lipid bilayer (SLB) is comprised of phospholipids that self-assemble onto a solid substrate. These lipids form a fluid bilayer that can be chemically decorated with a variety of biomolecules, and thus

the SLB displays chemical and physical properties that resemble those of the cellular plasma membrane.[125-126] Importantly, when a living cell encounters an SLB displaying appropriate ligands, the cell surface receptors bind, oligomerize, and laterally translocate across the cell–SLB junction. Therefore, this platform provides a powerful tool to reconstitute juxtacrine signaling pathways such as IS formation during T-cell signaling,[127-131] receptor clustering in E-cadherin,[132] EphA2–EphrinA1,[47, 133] Notch–delta[134] and integrin–RGD[135-137] systems. Taking advantages of the cell–SLB platform, we aimed to tether MTFM tension probes onto an SLB to enable the study of receptor mechanics during active signaling at model cell-cell junctions.

2.2 Results and discussion

2.2.1. Design of ratiometric tension probes

To generate SLB-tethered tension probes, we first designed a DNA hairpin structure that places a fluorophore-quencher pair (Cy3B-BHQ2) in close proximity. DNA hairpins are immobilized onto a AuNP that further quenches the Cy3B fluorescence. The AuNP-tension probe is in turn immobilized onto a SLB using biotin-streptavidin and is further functionalized with a ligand. DNA hairpins unfold in response to mechanical strain, which separates the fluorophore from the molecular quencher and the AuNP surface. The magnitude of force needed to unfold the hairpin can be estimated from the $F_{1/2}$, which is the force that leads to 50% probability of unfolding at equilibrium.[76] Note that the loading rate and the duration of forces are unknown and thus the $F_{1/2}$ serves as a lower bound estimate

of the applied force. Due to the dual quenching of the dye by a molecular quencher (FRET)[138] and the AuNP via Nanometal Surface Energy Transfer (NSET),[139] this construct provides a 10-fold improvement in sensitivity over the existing MTFM probes.[118-119] To distinguish fluorescence enhancement due to clustering from that of tension, we introduced a second fluorophore (Alexa Fluor® 488, abbreviated A488 thereafter) to report on relative probe density (**Scheme 2.1**). The size of AuNP-tension probes is estimated to be 47.4±1.8 nm from dynamic light scattering (DLS) (**Figure A2.3**). Each particle is labeled with 38±1 hairpins as determined by fluorescence calibration (**Figure A2.4**).

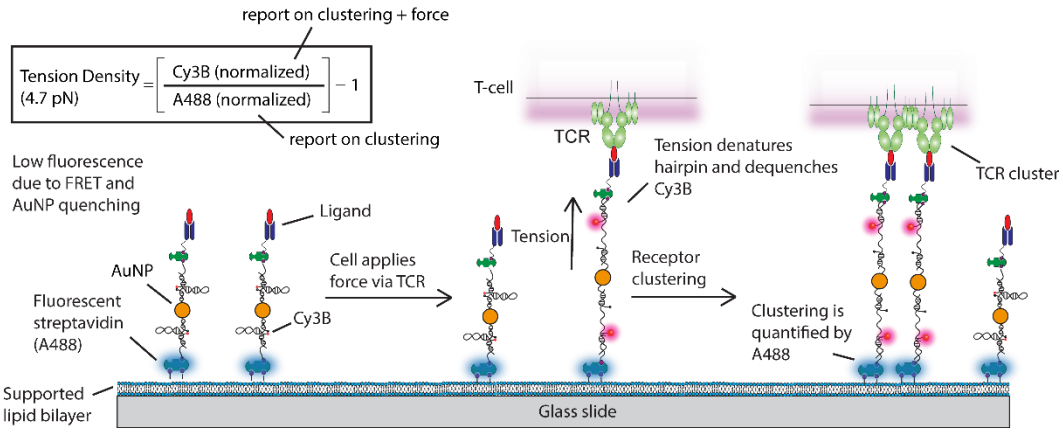

Scheme 2.1. Schematic representation of gold nanoparticle-based ratiometric tension probes

2.2.2. Validating ratiometric tension probes using biotinylated silica beads

To demonstrate that the ratiometric tension probe can reliably report on clustering and mechanics, we employed a model system to mimic the cell–SLB junction. In this system, tension probes ($F_{1/2}$ = 4.7 pN, see **table A2.1** for DNA sequences) were immobilized onto a SLB and decorated with streptavidin that engaged biotinylated microparticles (diameter = 5 μm) (**Figure 2.1A**). It has been shown that the junction between a spherical particle and planar SLB generates

interfacial tension across the ligand-receptor complexes (biotin-streptavidin) bridging the particle to the SLB.[140] This is due to the geometric mismatch between the particle and planar surface. We anticipated accumulation of streptavidin as well as the extension of a subset of DNA hairpins bridging the particle and the surface within the contact zone. Incubation of biotinylated microparticles onto the tension probe-SLB surface generated a strong interference pattern in reflection interference contrast microscopy (RICM), indicating close nanoscale contact between the particle and surface (**Figure 2.1B**). This interaction led to a drastic increase in fluorescence in both the Cy3B and the A488 signals (**Figure 2.1B)**. Line scan analysis across the microparticles showed a maximum of ~14 fold increase in Cy3B fluorescence, which reports on probe clustering and hairpin unfolding, while only a ~2.5-fold enhancement was observed in the A488 channel, which exclusively reports on clustering (**Figure 2.1C**). Fluorescence from both channels colocalized with the RICM interference pattern and were most pronounced at the center of the microparticle-SLB contact zone, confirming microparticle-driven probe clustering (**Figure 2.1D**).

To estimate the relative fraction of open hairpins induced by microparticle binding, we created normalized Cy3B and A488 images (normalized to a region of interest lacking cells). The normalized Cy3B image was divided by the normalized A488 image, and then was subtracted by 1 to obtain a tension density map, such that a tension density signal of ~0 corresponds to the background (**Scheme 2.1** and **Figure A2.2.3** for detailed image processing procedures). Tension density signals that are greater than 0 indicate a relative fraction of hairpins in the open state.

Molecular binding between microparticles and hairpin tension probes within the contact zone generated fluorescence enhancement greatest at the center and had an average tension density value of 4.29±1.16 (**Figure 2.1E**). As a control, we used AuNP-duplexes lacking a hairpin loop and for which the fluorescence increase is exclusively due to clustering rather than hairpin unfolding (see **table A2.1** for DNA sequences). As expected, tension density signal on these surfaces were significantly lower (0.05±0.13) compared to the surfaces decorated with hairpin tension probes (**Figure A2.2.4 and Figure 2.1E)**. Collectively, these results indicate that the ratiometric response of the tension probe is largely due to mechanical unfolding of the hairpin stem-loop of the tension probes.

We further evaluated the interaction between the microparticles and tension probes by immobilizing the tension probes on glass surfaces, where probe clustering is prohibited (**Scheme A2.2**). On these surfaces, the Cy3B signal was localized at the edges of the microparticle-surface junction. Unlike SLB surfaces, line scan analysis across the microparticles revealed two local maxima in Cy3B channel, and the peaks encased the center of microparticle-surface contact zone (**Figure A2.2.5**). In contrast, no accumulation of fluorescence in the A488 channel was observed (**Figure A2.2.5**). Control experiments using DNA duplexes showed a small increase in fluorescence (25.5±26.4%) in the Cy3B channel, whereas tension probes immobilized on glass surfaces had an average of 4-fold enhancement in Cy3B fluorescence (400±115%) underneath the microparticle-surface contact zone (**Figure A2.5**). These results show that ratiometric tension probes can be used to distinguish signals due to tension from that of clustering.

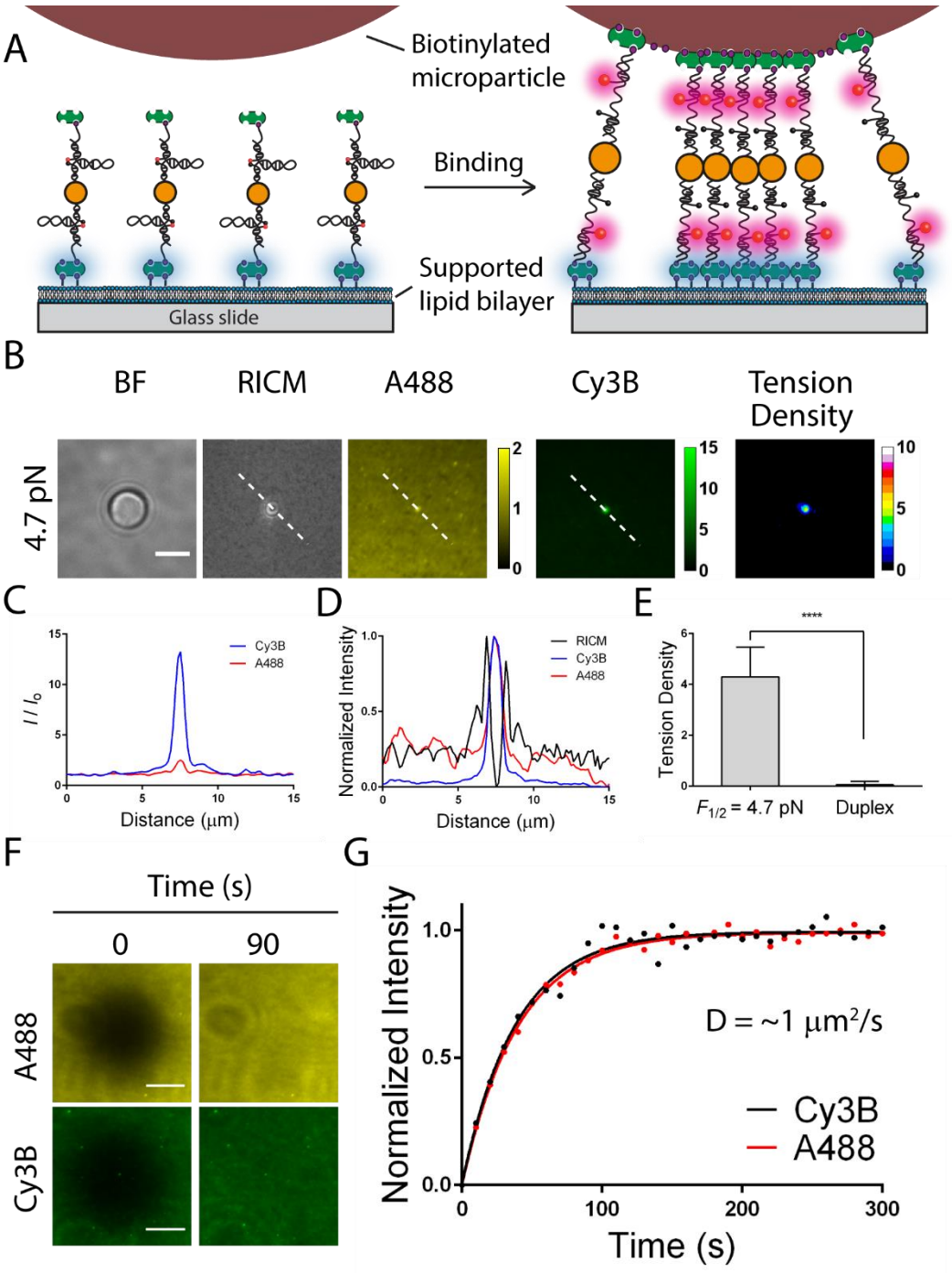

Figure 2.1. Biotinlyated silica microparticle as an artificial cell. **A)** Illustration of the contact zone between a biotinylated microparticle and a DNA tension probe surface anchored to a supported lipid membrane. **B)** Representative brightfield, RICM, Cy3B, A488, and tension density images showing the contact zone of a microparticle (diameter = 5 μm) that binds to SLB tension probes ($F_{1/2}$ = 4.7 pN). Scale bar = 5 μm. **C)** Plot displaying line scan of Cy3B and A488 channels for the microparticle shown in **B**. The intensity is normalized to the background regions

lacking the microparticle. **D)** Plot overlaying the line scan profile of fluorescence and RICM channels, and demonstrating their spatial colocalization. **E)** Bar graph showing the tension density of microparticles engaged to tension probe SLBs ($F_{1/2}$ = 4.7 pN) and control SLB surfaces decorated using DNA duplexes (n = 20 for each sample, error bar represents S.D. of the data) within the microparticle-SLB contact zone. **F)** Representative FRAP images showing recovery after 90 s. Scale bars = 10 μm. **G)** Representative FRAP recovery plots for Cy3B and A488 channels. Solid lines represent the fit made using the following equation $F(t) = A(1-e^{-t\tau})$. The Lateral diffusion coefficient (D) is calculated by: $D = w^2/4t_{1/2}$, where w is the radius of the Gaussian bleaching area; $t_{1/2}$ is the time for 50% recovery obtained from the fit. The values used for the calculation were: w = 10.4 μm (for both channels); $t_{1/2}$ = 26.5 s (Cy3B) and 27.9 s (A488).

2.2.3. Ratiometric tension probes map T cell receptor forces and clustering

To test whether the ratiometric tension probe is suitable for mapping TCR tension and lateral transport (**Scheme 2.1**), we tethered the $F_{1/2}$ = 4.7 pN probes onto SLBs presenting biotin and Ni-NTA (0.1% biotin-DPPE, 4% Ni-NTA DOGS and 95.9% DOPC). In a one-pot incubation, we decorated the tension probes with anti-CD3 antibody that binds and activates the TCR and also introduced His_6-ICAM-1 on the lipid membrane to support T-cell spreading (**Scheme A2.1 and method**). Given that each gold nanoparticle presents ~38 biotinylated DNA hairpins, it is possible for each particle to bind multiple streptavidin molecules on the SLB, thus reducing the probe mobility. To minimize multivalent binding, we tuned the biotin doping level in the SLB (from 0.001% to 1% biotin) and measured the stoichiometry between the gold particles and streptavidin. We identified that a concentration of 0.1% biotin-DPPE provides the highest density and optimal coverage of probes while maintaining their long-range fluidity (**Figure A2.6**). The mobility of the tension probes and A488-labelled streptavidin on this surface was confirmed by fluorescence recovery after photobleaching (FRAP) experiments.

Both the Cy3B and A488 fluorescence channels showed ~90% recovery within 90s (**Figure 2.1F**). The estimated lateral diffusion coefficients (D) of the fluorescent streptavidin and tension probes are almost identical (~1 $\mu m^2/s$), confirming that the tension probes are primarily bound to streptavidin tethered on the lipid membrane (**Figure 2.1G**).

With the fluid AuNP-tension probes in hand, we next plated CD4+ T-cells directly onto the surface. T cells rapidly spread upon initial engagement to the SLB (within the first 3 min). In a representative cell shown in **Figure 2.2A**, time-lapse imaging showed the accumulation of fluorescence in both Cy3B and A488 channels underneath the cell (**Figure 2.2A**, t = 3 min, white circle). The tension density (ratiometric) signal showed a gradual increase in intensity that colocalized with a subset of the accumulating Cy3B signal. This indicates that TCRs transmit mechanical forces exceeding $F_{1/2}$ = 4.7 pN to a fraction of the clustering anti-CD3 ligands. The T-cell continuously translocated anti-CD3 probes throughout the 15 min duration of the video. Starting at t = 4 min, centripetal movement of clusters was accompanied by waves of inward tension density signal (**Figure 2.2A**). A larger fraction of tension probes were unfolded at the periphery of the accumulating clusters. Kymographs of different region of interests (ROIs) showed that tension gradually developed across the cell surface over the 15 min duration of the video, and TCR tension and clustering are closely linked in space and time (**Figure 2.2B**). Note that the tension density signal was most pronounced for larger clusters at the micron-scale and this signal was highly dynamic. Smaller oligomers or monomers may also experience mechanical strain that is not reported by our probes because it

is below the 4.7 pN threshold for DNA unfolding or possibly due to the low signal-to-noise ratio associated with smaller assemblies. The lateral translocation of TCR-ligand complexes and their accumulation at sites of diffusion barriers strongly suggests that these complexes experience mechanical strain.[20] Nonetheless, our results provide the first direct evidence that the TCR transmits pN mechanical strain to its ligand within a fluid intermembrane junction.

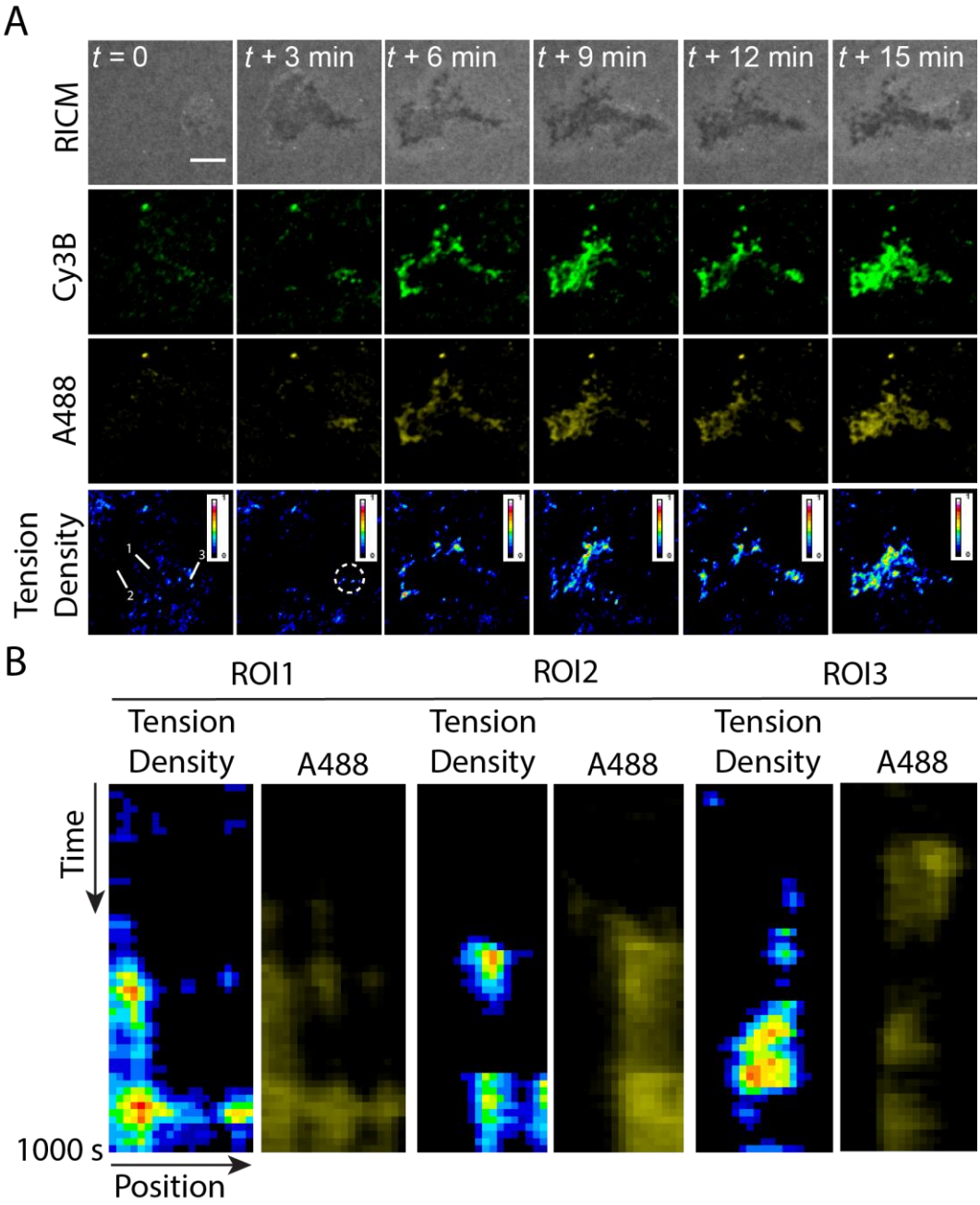

Figure 2.2. T cell interacting with DOPC-SLB with tethered ratiometric tension probes. A**)** Representative time-lapse images (RICM, Cy3B and A488 and tension density) showing the first 15 min of CD4+ T-cell engagement with the CD3-tension probes anchored onto an SLB. **B)** The kymographs display tension density and the A488 intensity as a function of time within the three regions of interest (lines in the tension density channel from **A**). Scale bar = 5 μm.

2.2.4. T cell receptors transmit forces at the cSMAC

We next aimed to investigate whether TCR-ligand complexes experience tension within the cSMAC, which forms at later points after formation of the IS and is associated with signal termination and receptor degradation.[108, 141] An important question pertains to the cSMAC structure is whether TCR-ligand complexes in this centralized assembly experience mechanical load during TCR recycling.[142] To answer this question, T-cells were incubated with the tension probe surfaces for 30 min to allow for complete cSMAC formation. After 30 min of cell spreading, we observed Cy3B and A488 signal in a central region that is a hallmark feature of cSMAC formation (**Figure 2.3A**).[143] The cSMAC displayed strong tension density signal with a maximum value of ~2, exceeding the values observed during initial TCR-ligand binding and clustering (**Figure 2.3A**). Also, the tension density within this structure was more homogeneous and less dynamic. Control experiments that used DNA duplexes showed the accumulation of anti-CD3 probes within a central cluster, but did not display significant tension density signal (**Figure 2.3A**). Scatter plot analysis revealed that an average tension density signal of 0.37±0.31 within the cSMAC while the control duplexes only had negligible signal (-0.02±0.08) (*n* = 25 cells for each group, **Figure 2.3B**). Immunostaining further confirmed that the Cy3B and A488 signals are strongly associated with TCR (Pearson correlation coefficients of ~0.8, **Figure A2.7**). Taken together these experiments demonstrate that the TCR-ligand complexes experience significant tension within the TCR recycling cSMAC structure.

2.2.5. TCR force transmission is enhanced by limiting the ligand mobility

To investigate the role of long-range lateral mobility of the ligand and how this influences TCR force transmission, we limited the mobility of SLBs by increasing streptavidin density (using 4% biotin-DPPE lipid composition). Lateral diffusion on these surfaces was significantly reduced as shown by FRAP measurements, in which the Cy3B signal from tension probes showed only ~40% recovery after 15 min (**Figure A2.8**). The reduced mobility could be due to local molecular crowding of the lipid bound streptavidin and the tension probes. T-cells plated on these surfaces showed reduced ligand translocation and accordingly, cSMAC formation was inhibited. Nonetheless, T cells plated on these surfaces showed that TCR-ligand complexes experienced tension across the cell junction and preferentially at the cell perimeter (**Figure 2.3C and D**). This spatial distribution of TCR tension is similar to that obtained using immobile tension probes.[31] Line scan analysis across the cell-SLB contact revealed that Cy3B signal exceeded the A488 signal across the whole inter-membrane junction (**Figure 2.3D**). These results demonstrate that T-cells transmit pN forces to ligand-receptor complexes with highly hindered mobility.

2.2.6. TCR forces and clustering are driven by myosin IIA

Literature precedent revealed that pre-treatment of T-cells with blebbistatin not only retarded their ability to form the cSMAC,[144-145] but also reduced IL-2 cytokine production.[146] These observations identify myosin IIA as an essential component contributing to TCR transport and ultimately T-cell immune function. To investigate whether impairment of myosin IIA activity directly regulates TCR

forces, we pretreated cells with 50 μM blebbistatin and plated these cells onto SLBs modified with tension probes for 30 min to allow for cell spreading. Under these conditions, T-cells formed limited clusters rather than the cSMAC (**Figure 2.3E**, A488 channel) and the tension density signal was dissipated (**Figure 2.3E**). This result shows that myosin IIA activity is required for mounting TCR tension during receptor clustering.

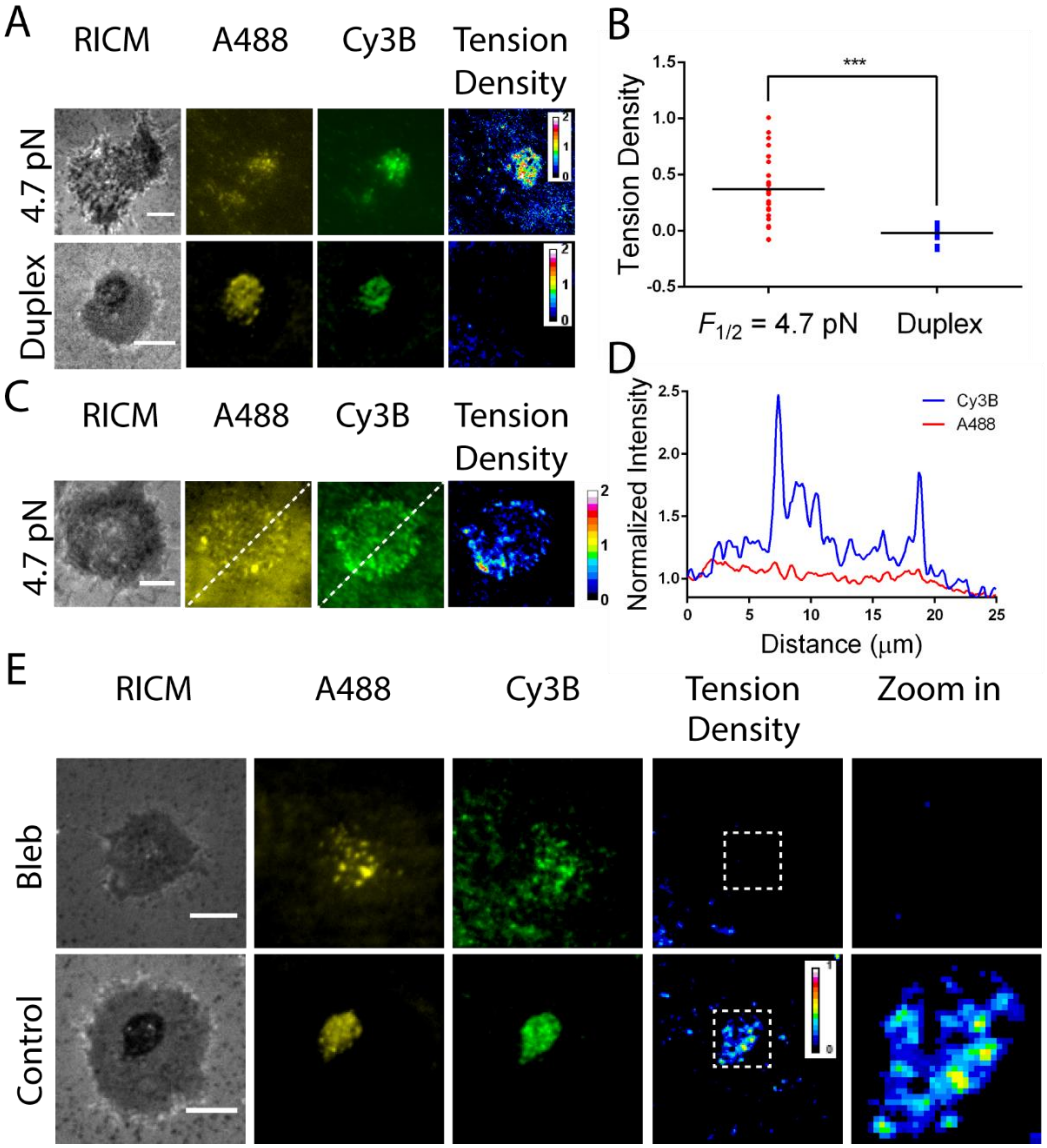

Figure 2.3. TCR transmits pN forces to ligands at cSMAC and limiting lateral mobility of SLBs enhances TCR forces. **A)** Representative images (RICM, Cy3B,

A488 and tension density) of CD4+ T-cells plated on fluid SLBs containing tension probes (upper panel) or control duplexes (lower panel) for a duration of 30 min. **B)** Scatter plot showing the mean tension density signal generated on tension probes and control duplexes within the cSMAC structure (n = 25 cells). **C)** Representative images (RICM, Cy3B, A488 and tension density) of CD4+ T-cells plated on the hindered SLB displaying tension probes. The mobility of tension probes was limited due to the high density of streptavidin on the SLB. **D)** Line profile across the cell (dashed line in **3C**) showing differential response in the Cy3B and A488 channels. **E)** Representative images (RICM, Cy3B, A488 tension density, and zoom in) of T-cells pre-treated with 50 μM blebbistatin (bleb) or without blebbistatin (control) and plated onto the 4.7 pN tension probe surface for a duration of 30 min. Scale bars = 5 μm.

2.3. Conclusion

In summary, we report the general design of ratiometric tension probes for direct imaging of mechanical tension experienced by ligand-receptor complexes within intermembrane junctions. Our ratiometric tension probes showed pN tension experienced by TCRs undergoing clustering and translocation in a myosin IIA dependent fashion. We also revealed mechanical forces within the cSMAC, which is possibly associated with the endocytosis of TCRs for recycling. Our approach is broadly applicable for studying the interplay between force and receptor clustering for juxtacrine receptor signaling pathways such as those for B-cell receptors, Eph–ephrin, cadherins, and Notch–Delta.

2.4. Materials and methods

2.4.1. Materials

Reagents, unless otherwise specified, were purchased from Sigma Aldrich (St. Louis, MO) and used as received. All solvents were of analytical grade and purified as needed. Cy3B NHS ester was purchased from GE Healthcare Life Sciences (Pittsburgh, PA). Lipids [DOPC (1,2-dioleoyl-*sn*-glycero-3-phosphocholine);

biotin-DPPE (1,2-dipalmitoyl-*sn*-glycero-3-phosphoethanolamine-N-(cap biotinyl)); and Ni-NTA DOGS (1,2-dioleoyl-*sn*-glycero-3-[(N-(5-amino-1-carboxypentyl)iminodiacetic acid)succinyl] (nickel salt) were purchased from Avanti Polar Lipids Inc. (Alabaster, AL). 5 μm silica microparticle was acquired from Bangs Laboratories Inc. (Fishers, IN). EZ-Link NHS-Biotin was purchased from Thermo fisher scientific (Waltham, MA). Recombinant mouse ICAM-1 Fc histag protein (cat no: 83550) was purchased from biorbyt (San Francisco, CA). Biotinylated anti-mouse CD3ε antibody (cat no: 145-2C11) was purchased from ebioscience (San Diego, CA). Alexa fluor 647 conjugated anti-TCR antibody (cat no: HM3621) was purchased from Life technologies (Grand Island, NY). All buffer solutions were made with Nanopure water (18.2 MΩ) and passed through a 0.2 μm filtration system. All oligonucleotides were purchased from Integrated DNA Technologies (Coralville, IA) or Eurofin Genomics (Huntsville, AL) and were purified either by reverse-phase HPLC or standard desalting. The backfilling PEG monothiol ($HS\text{-}(CH_2)_{11}\text{-}(OCH_2CH_2)_6\text{-}OCH_3$) was purchased from nanoScience Instruments (Phoenix, AZ). Bottomless 6 channel slides (Sticky-Slide VI 0.4, Cat no: 80608) were obtained from ibidi (Verona, WI).

2.4.2. Transgenic mice, T cell activation and purification

2D2 and SMARTA T cell receptor transgenic mice were housed and bred in the Division of Animal Resources Facility at Emory University in accordance with the Institutional Animal Care and Use Committee. These T cells express the CD4 co-receptor and recognize peptides in the context of the MHC allele I-Ab. Naïve T

cells were activated by culturing splenocytes ($5x10^6$ cells/well of a 24 well plate) with 1 mM peptide for 7 days in complete RPMI media [1x RPMI 1640 (Corning), 10% heat-inactivated fetal bovine serum albumin, 10 mM HEPES buffer (Corning), 50 mg/mL gentamicin solution (Corning), 5×10^{-5} M 2-mercaptoethanol and 2 mM L-glutamine. The peptides used to activate 2D2 and SMARTA T cells were myelin oligodendrocyte glycoprotein epitope 35-55 (MEVGWYRSPFSRVVHLYRNGK), glycoprotein epitope 61-80 (GLNGPDIYKGVYQFKSVEFD) and mycobacterium tuberculosis epitope 280-294 (FQDAYNAAGGHNAVF) respectively. T cells were harvested from culture by density centrifugation using Lymphocyte Separation Medium (Corning), density of 1.077-1.080 g/mL at 20ºC, in accordance with manufacturer instructions. Purified T cells were washed and stored in complete RPMI until analysis. In some cases, the cells were reactivated for additional experiments. In this case, 2×10^5 T cells (from the above purification step) were cultured for another week with fresh peptide and irradiated (3000 rads) splenic antigen presenting cells in complete RPMI.

2.4.3. General experimental procedures

Concentrations of purified oligonucleotide conjugates were determined by measuring their A_{260} values on Nanodrop 2000 UV-Vis Spectrophotometer (Thermo Scientific). MALDI-TOF Mass Spectrometry was performed on a high performance MALDI time-of-flight mass spectrometer (Voyager STR). The matrix for all experiments was prepared by freshly dissolving excess 3-hydroxypicolinic acid (3-HPA) in the matrix solvent (50% MeCN/H_2O, 1% TFA, 10% of 50 mg/mL

ammonium citrate). Dynamic light scattering was performed using NanoPlus DLS Nano Particle Size and Zeta Potential Analyzer. For transmission electron microscopy (TEM), AuNP-tension probes absorbed on TEM grid were negatively stained for 10 s using a 2% aqueous uranyl formate solution and imaged on a Hitachi H-7500 transmission electron microscope at an accelerating voltage of 75 KV.

2.4.4. Synthesis of A21B-Cy3B DNA strand

The strand is prepared following a reported protocol.[147] In brief, A mixture of A21B (10 nmol) and excess Cy3B NHS ester in 0.1 M sodium bicarbonate solution was allowed to react at room temperature overnight. The mixture was then subjected to P2 gel filtration to remove salts, organic solvent and unreacted reactants, and was further purified by reverse phase HPLC (solvent A: 0.1 M TEAA, solvent B: 100% MeCN; initial condition was 10% B with a gradient of 1%/min, flow rate: 1 mL/min). The desired product was characterized by MALDI-TOF mass spectrometry.

2.4.5. Fluorescence labelling of streptavidin

100 μg of the streptavidin was labelled with 5-fold excess of Alexa 488 NHS-ester in 1X PBS with 0.1 M sodium bicarbonate. The reaction was allowed to proceed for 15 min on a rotary platform. The mixture was then subjected to P4 gel filtration to remove unreacted dyes. The final product was characterized by UV-vis spectroscopy.

2.4.6. Synthesis of biotin-functionalized particles

The biotin-functionalized particles were prepared using modified literature methods.[148] Briefly, 100 µg/mL of the 5 µm silica microparticles were dissolved in 0.1 M sodium bicarbonate solution (volume = 90 µL), and were mixed with 100 µg/mL of NHS-biotin (dissolved in 10 µL DMSO prior adding to the reaction mixture). The particles were allowed to react on a rotary platform for 4 h. The reaction mixture was diluted to 1 mL using milli-Q water. The particles were purified by centrifugation (15,000 rpm, 5 min) for seven times. Finally, the particles were resuspended in milli-Q water and stored at 4 ºC.

2.4.7. Functionalization of AuNP with DNA tension probes or DNA duplexes

Citrate stabilized nanoparticles were prepared by the citrate reduction method[149] and the size (14±2 nm) was determined using by transmission electron microscopy. The functionalization of AuNP-DNAs was achieved using modified literature protocols.

Synthesis of AuNP-tension probes: 20 µM of Cy3B-A21B strand, T21A-BHQ2 quencher strand and 22 µM of hairpin strand (ratio = 1:1:1.1) were annealed in 50 µL 0.2X PBS buffer at 95 ºC for 5 min and the solution was allowed to cool to room temperature slowly. After 30 min, the resulting hybridized DNA solution was added to 1 mL of gold nanoparticle solution (10 nM) and was incubated on an orbital shaker for 1 h. Subsequently, phosphate buffer (0.1 M, pH = 7.4) and 10% sodium dodecylsulfate (SDS) solution (w/v) were added to the mixture bringing its concentration to 10 mM and 0.1%, respectively. The resulting solution was

gradually "salted" with six aliquots of 2 M NaCl solution (0.05 M each) over 2 h (20 min interval) to achieve a final NaCl solution of 0.3 M. Note that after each salting the gold nanoparticle solution was sonicated for 10 s in order to maximize DNA packing. The particles were agitated overnight and were light protected. Afterwards, 30 μM of passivating PEG (SH-PEG) was added to the AuNP-DNA solution and was allowed to incubate for 4 h. The reaction mixture was centrifuged (13,000 rpm, 20 min) three times and resuspended in 1X PBS solution.

Synthesis of AuNP-duplexes: 20 μM of Cy3B-A21B strand, T21A-BHQ2 quencher strand and 22 μM of the hairpin strand without stem loop (ratio = 1:1:1:1.1) were annealed in 50 μL 0.2X PBS buffer at 95 ^{o}C for 5 min and the solution was allowed to cool to room temperature slowly. AuNP-duplex probe were then prepared using the aforementioned protocol.

2.4.8. Preparation of small unilamellar vesicle

Small unilamellar vesicle (SUV) was prepared according to reported protocols.[47, 134, 150] In brief, lipids with desired composition were mixed in a round bottom flask. The lipid mixture was subjected to rotary evaporation to remove the chloroform solution. The lipids were further dried under a steam of N_2 and then hydrated with 2 mL of milli-Q water with a concentration of 2 mg/mL. Three cycles of freeze-thaw were performed in order to completely dissolve the lipids. The resulting lipids were then repeatedly extruded through polycarbonate filters with the size of 100 nm until the solution became clear (~10-20 times) and stored at 4 ^{o}C. The extruded SUVs are stable for 4-6 weeks.

3.4.9. Supported lipid bilayer (SLB) formation and functionalization (Scheme A2.1)

75 x 25 mm glass slides (cat. no: 10812, ibidi, Verona, WI) were sonicated in a mixture of water and isopropanol (1:1) for 30 min and then etched in piranha solution (**CAUTION: Piranha is highly reactive and explosive on contact with organics!**) for 15 min. After that, the substrates were cleaned extensively by immersing in a beaker containing clean milli-Q water for 6 times and dried in oven. The cleaned coverslips were then assembled to a 6 channel µ-Slide (ibidi, Verona, WI) to create flow chambers with a channel volume of 30 µL. Stock lipid vesicle solutions were diluted with 1X TBS buffer to a final concentration of 0.5 mg/mL. The vesicles were added to the channels and allowed to spread for 30 min. Unbounded vesicles were removed with three washes of 1X TBS.

For experiments with 5 µm biotinylated silica microparticles (Scheme A2.1A): Surfaces were incubated with 0.01% BSA for 30 mins, and then 10 µg/mL Alexa-488 labelled streptavidin for 45 min. Afterwards, 1 nM of the AuNP-tension probe solution was introduced to the flow chambers and incubated with the surface for 10 min. We found that a short incubation produced higher quality surfaces. 1 µM of free biotin was added and incubated with the surface for 15 min to block vacant streptavidin binding sites. Then 10 µg/mL of streptavidin was added and allowed to interact with the AuNP-tension probes for 30 min. Finally, 5 µm biotinylated silica microparticles were added and allowed for incubate for 10 min before imaging.

For experiments with T-cells (Scheme A2.1B): Prior to modification of the

bilayer surface, bilayers were incubated with 100 mM $NiCl_2$ for 5 mins to ensure Ni^{2+}-NTA binding. Surfaces were prepared similarly as mentioned above except for the last step. In the last step, the desired concentration of biotinylated anti-mouse CD3ε antibody and His-tagged ICAM-1 were loaded to the surface and incubated for 35 min. Note that prior to each incubation step, the surfaces were rinsed with 1X TBS to remove the unbounded species. In all experiments, 1X TBS solution in flow chambers was exchanged with hank's balanced salt solution (prior to addition of T-cells. Cells resuspended in hank's balanced salt solution were added on the surface.

5.4.10. Drug treatment

50 μM blebbistatin was incubated with T-cells for 15 min before cell plating. Drug treated cells were plated on the surface and were allowed to incubate for 30 min before imaging.

5.4.11. Image acquisition and analysis

Images were acquired using a Nikon Eclipse Ti epifluorescence microscope equipped with a TIRF launcher with three laser lines: 488 nm (10 mW), 561 nm (50 mW), and 638 nm (20 mW), an Intensilight epifluorescence source, a EMCCD camera (Photometrics) and the following Chroma filter cubes: reflection interference contrast microscopy (RICM), TIRF 488, TIRF 561 and TIRF 640, and a CFI Apo x100 objective (Nikon, numerical aperture = 1.49). Images were captured using the Element software package (Nikon) with the following exposure

times: 50–100 ms for RICM channel; 50–300 ms for T561 channel and 50–100 ms for T488 channel. The images were processed using Fiji, an open source imaging package based on imageJ. Image analysis for converting raw images into tension density signal is shown in **Figure A2.3**.

2.6. Appendix

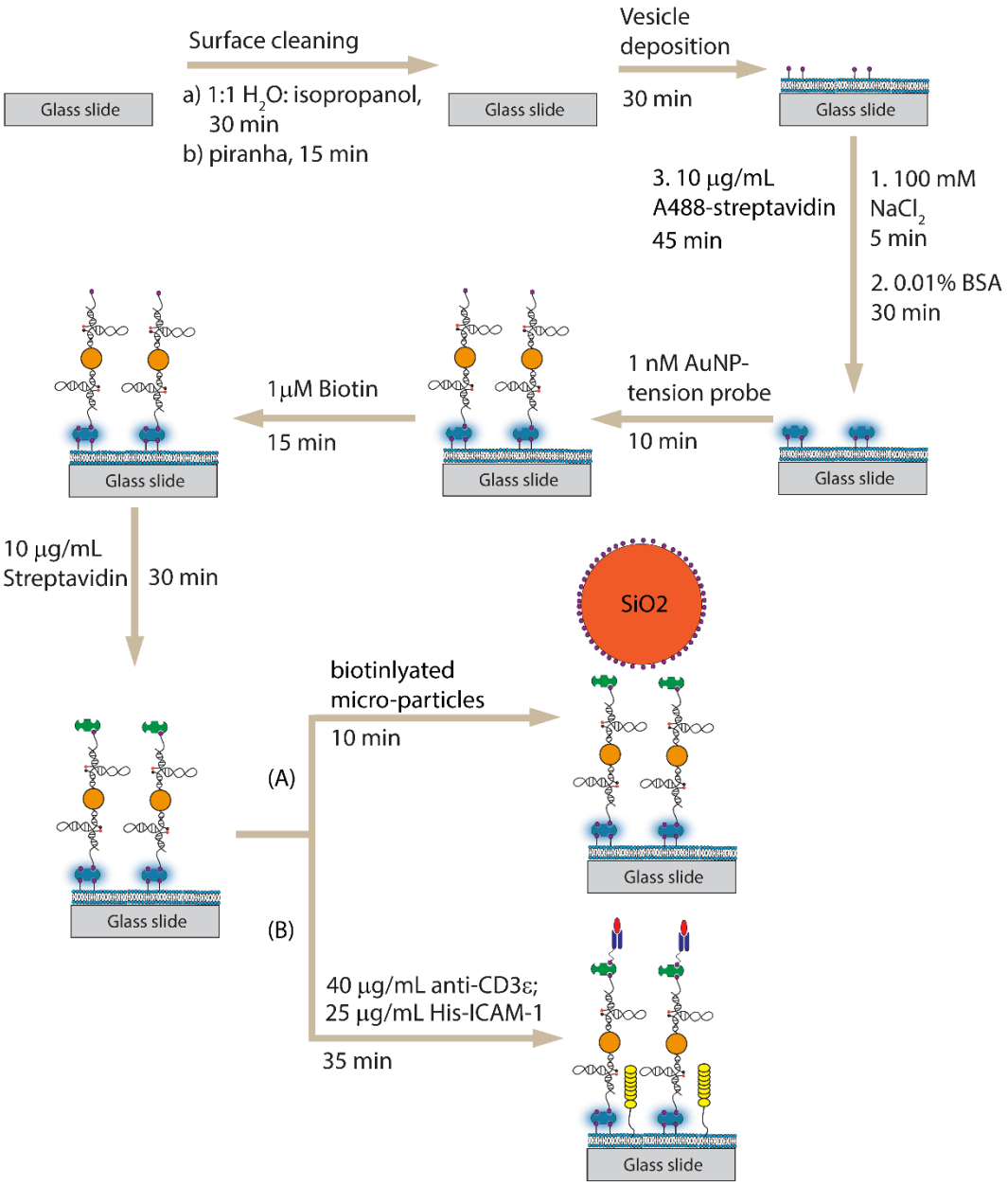

Scheme A2.1. Schematic representation showing the stepwise procedure for preparing supported lipid bilayers decorated with AuNP-tension probes.

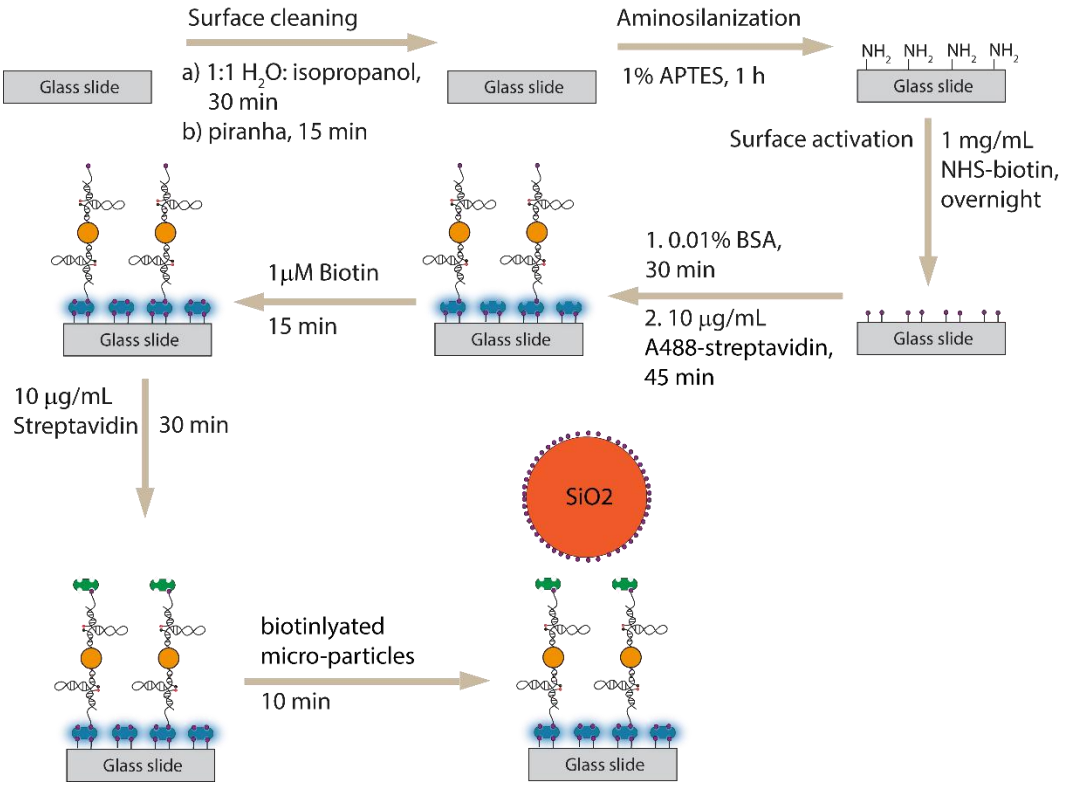

Scheme A2.2. Schematic illustration showing the stepwise procedure for immobilizing AuNP-tension probes onto a glass slide

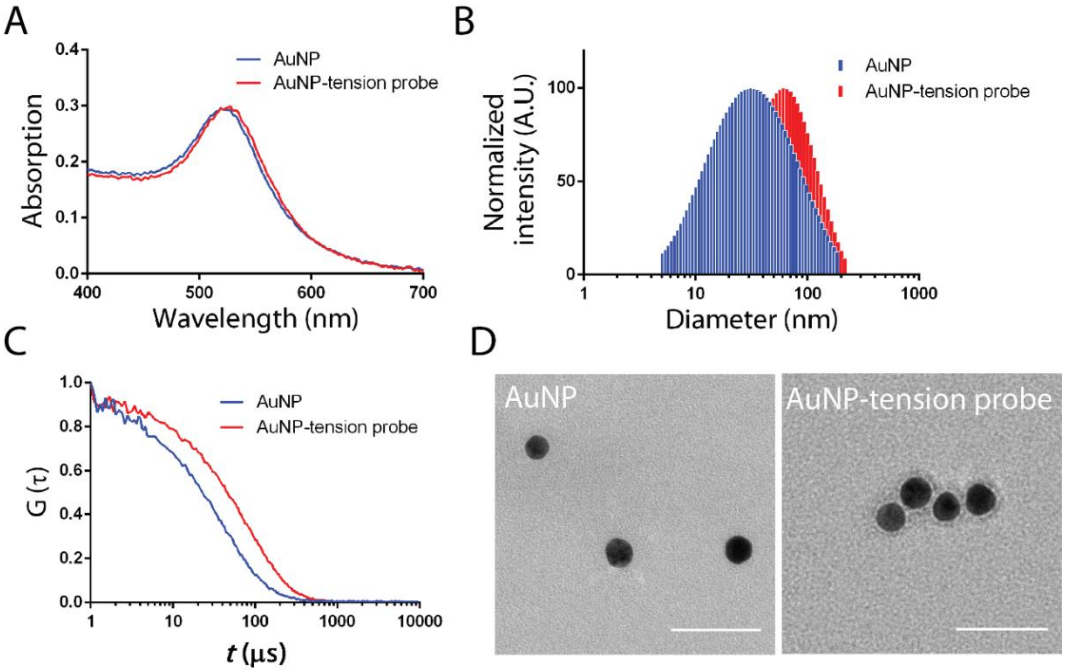

Figure A2.1. Spectroscopic characterization of AuNP and AuNP-tension probes. AuNP and AuNP-tension probes were characterized by UV-vis absorption spectroscopy; dynamic light scattering (DLS) and transmission electron microscopy (TEM). In a representative UV-vis spectrum, we observed an evident peak shift from 520 nm (AuNP) to 524 nm (AuNP-tension probe) that indicates attachment of DNA on the AuNP (**Figure A2.1A**). **Figure A2.1B and Figure A2.1C** showed the representative size histogram of AuNP and AuNP-tension probes also their autocorrelation functions measured by DLS. Statistics of DLS measurement are shown in **table A2.2**. **Figure A2.1D** showed representative TEM images of AuNPs and AuNP-tension probes. We observed an outer layer of stained DNA in AuNP-tension probe sample but not in bare AuNP. Scale bars = 50 μm.

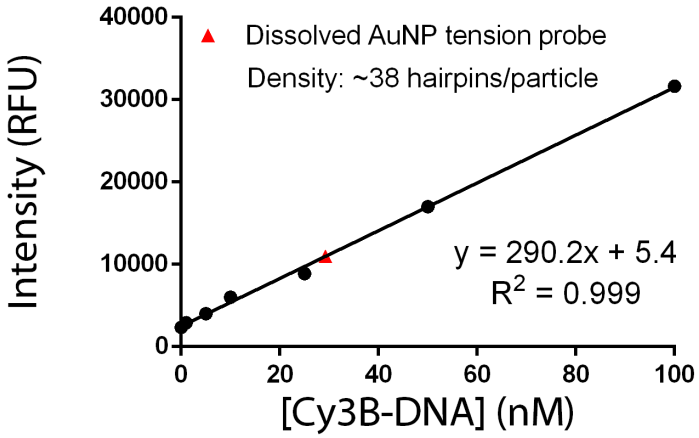

Figure A2.2. Quantification of the number of tension probes per AuNP. The number of tension probes per particle was determined by using a fluorescence calibration curve. In brief, 1 nM of AuNP-tension probe was dissolved using 25 µM KCN in 1X PBS for 30 min. 1 µM of the complementary strand was added into the resulting solution and was heat annealed to open the hairpin structure. A fluorescence calibration plot was constructed with increasing concentrations of "free" Cy3B-A21B strands. By fitting the fluorescence intensity of the dissolved, opened tension probes (red triangle) into the calibration plot, the density of the tension probes per particle was determined.

Slope of the calibration curve (m)	= 290.2
Intensity of the opened tension probes (*I*)	= 10098
Concentration of AuNP-tension probes (C_{AuNP})	= 1 nM
Number of tension probes per particle	= I/m/ C_{AuNP} = 10998/290.2/1 = **37.8 hairpins/particle**

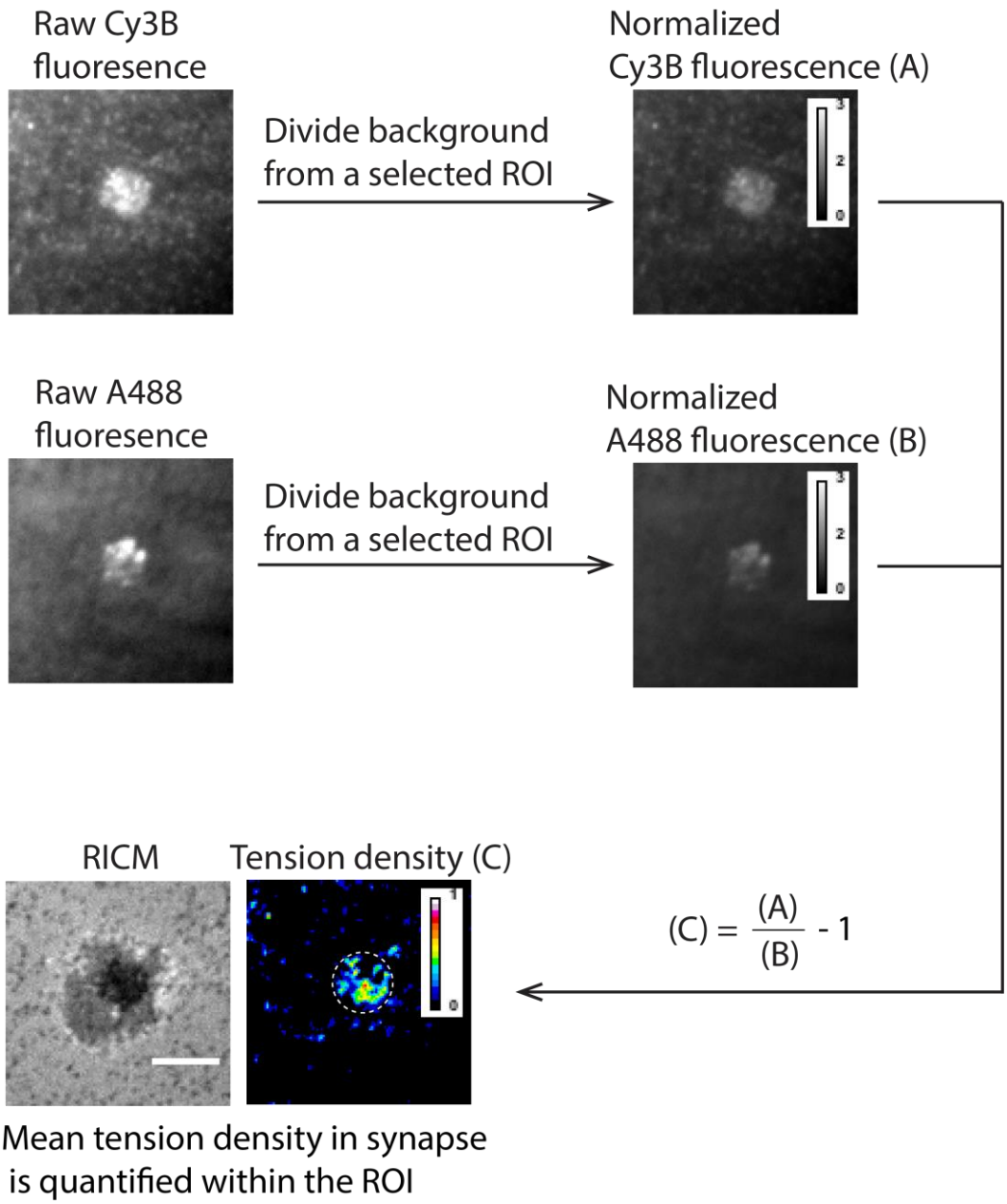

Figure A2.3. Image analysis pipeline to convert the raw images into tension density signal. A series of image operations were performed to in order to obtain the tension density signal. In brief, the raw images from the Cy3B and A488 channels were normalized by a defined region of interest lacking cells from the same sample, therefore yielding ratio images of probe (A) or A488-streptavidin (B), respectively. This normalization accounted for sample to sample differences in probe density. Then the normalized images of probe and A488-streptavidin were converted to tension signal (C) by dividing A (signal due to clustering and tension) by B (signal due to clustering), and subtracting the resulting image by 1. Scale bar = 5 μm.

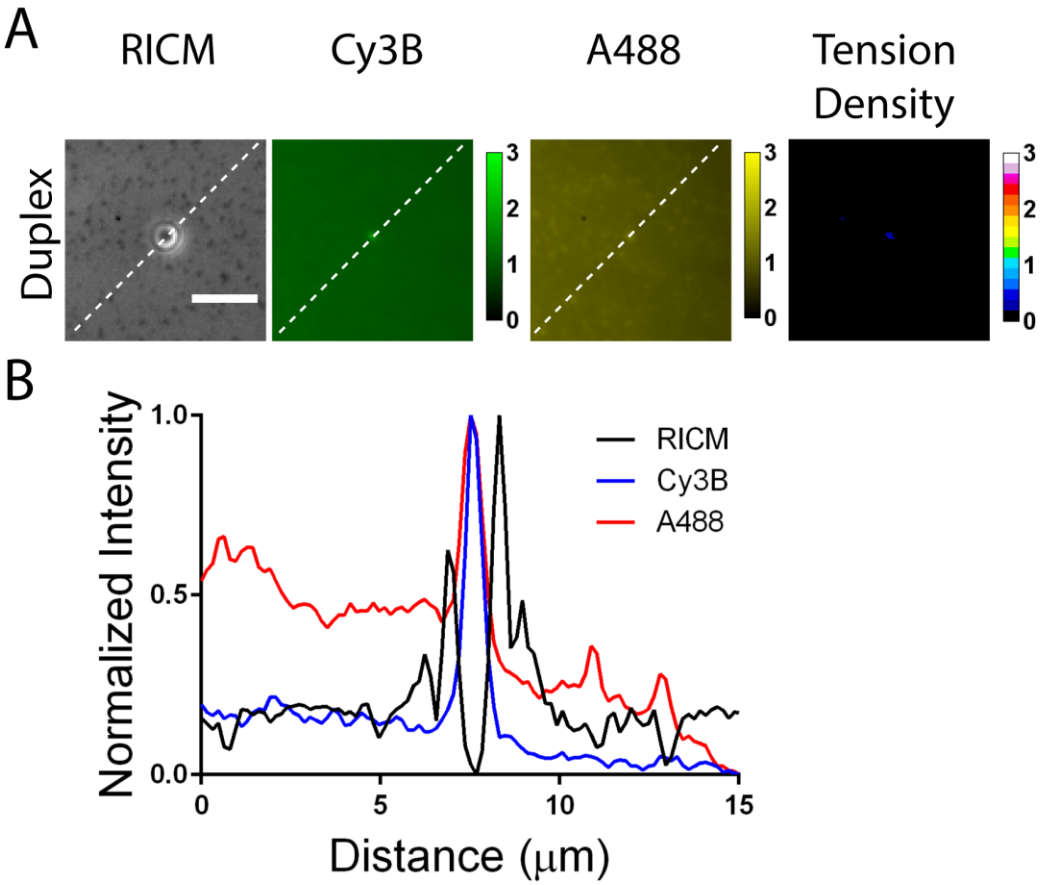

Figure A2.4. A) Representative RICM, A488, Cy3B and tension density images of biotinylated microparticle that binds to AuNP-duplexes on the SLB. Scale bar = 5 μm. **B)** Intensity profiles (dashed lines) of microparticle interacting with control duplexes on SLBs.

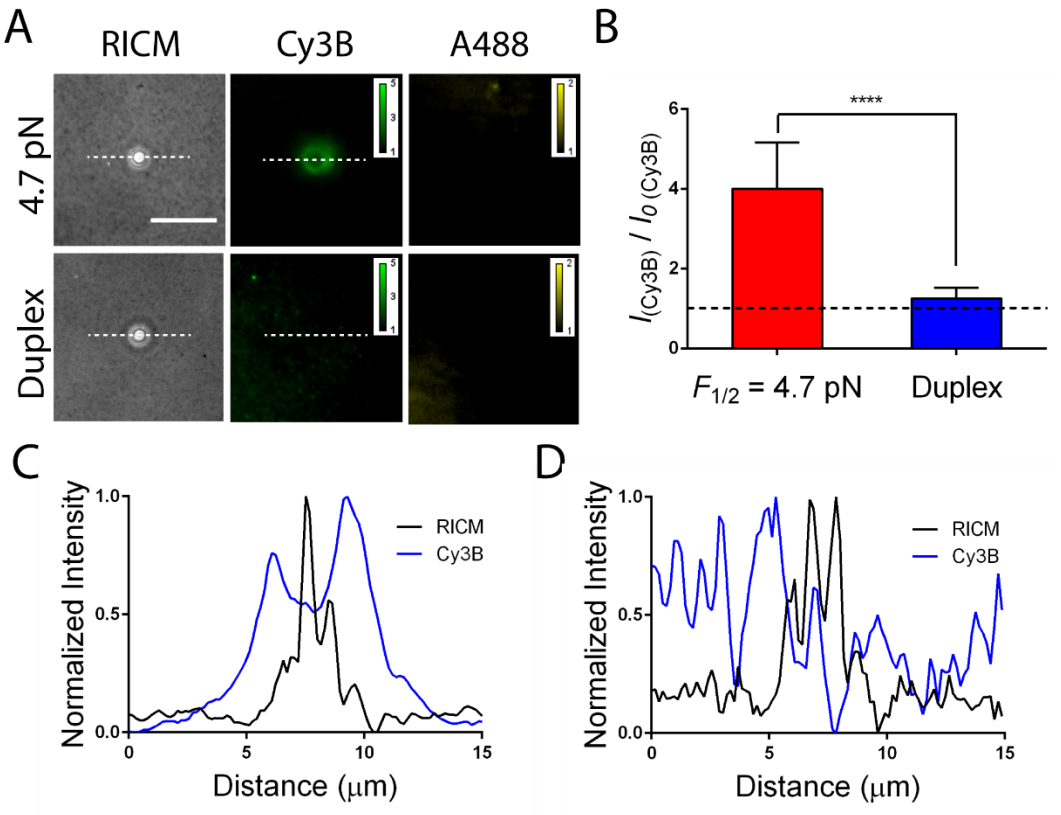

Figure A2.5. A) Representative images of biotinylated microparticles (diameter = 5 μm) that binds to AuNP-tension probes and control AuNP-duplexes immobilized on glass surfaces. Scale bar = 10 μm. **B)** Plot showing relative change in Cy3B fluorescence [$I_{(Cy3B)}$ / $I_{0\,(Cy3B)}$] within the contact zone of microparticles bound to tension probes and control duplexes. Error bar represents S.D. of the results (n = 20 beads). $I_{(Cy3B)}$ is the Cy3B fluorescence within the bead-surface contact and $I_{0\,(Cy3B)}$ is the background Cy3B fluorescence. **C and D)** Intensity profiles (dashed lines) of microparticle interacting with tension probes (**C**) and control duplexes (**D**) on glass surfaces. Note that the change in Cy3B signal of the control duplexes is minimal, and therefore its intensity profile appeared to be structureless.

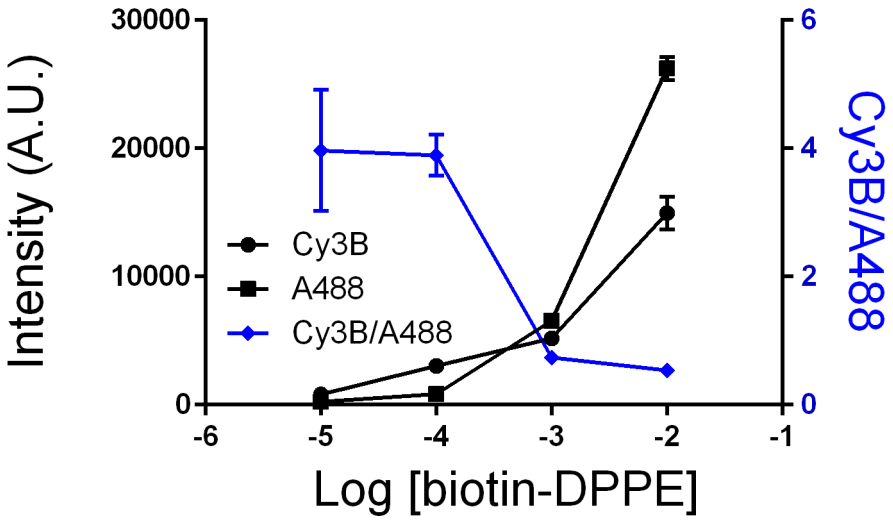

Figure A2.6. Plot of Cy3B and A488 intensity as a function of log[biotin-DPPE]. To optimize the stoichiometry between the AuNP-tension probes and the streptavidin, we tuned the concentration of biotin-DPPE lipid from 0.001% to 1% and measured the corresponding Cy3B and A488 intensity values. The Cy3B/A488 ratio signal decreased significantly at the 0.1% biotin-DPPE molar concentration and reached a plateau at 1% biotin-DPPE concentration. We chose the 0.1% biotin for anchoring the fluorescent streptavidin and tension probes for our experiments due to the following reasons: 1) both channels present a fluorescent monolayer allowing easy identification of clustering events; and 2) 0.1% biotinylated SLBs co-presenting ICAM-1 and tension probes are mobile with D = ~1 μm (**Figure 1G**). Note that greater concentrations of biotin-DPPE led to hindered mobility as measured by FRAP. In contrast, lower densities of biotin-DPPE led to highly fluid bilayers but these bilayers were sub-optimal for force measurement.

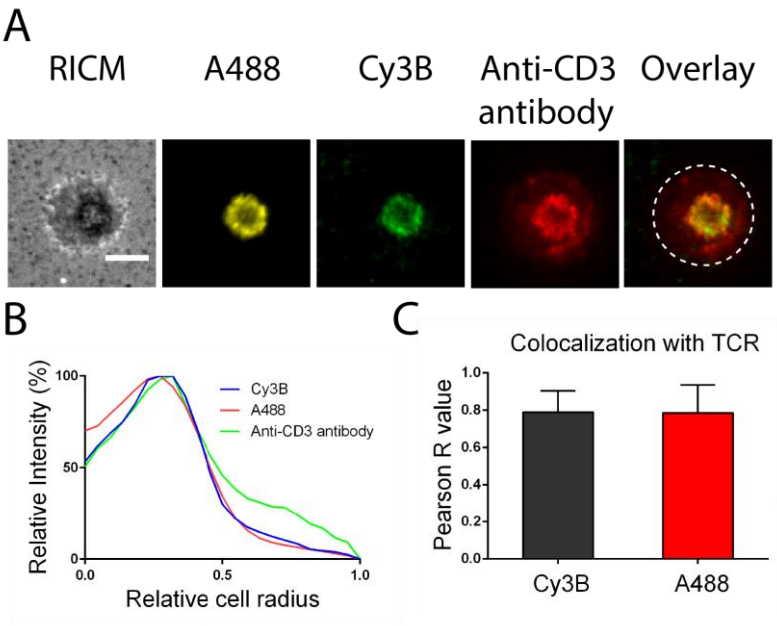

Figure A2.7. Co-localization between the A488 labelled-streptavidin (A488), tension probes (Cy3B) and TCR (red). To confirm signals observed in A488 and Cy3B channels are due to clustering of tension probes driven by TCR-ligand binding. We preformed immunostaining where we co-incubated Alexa647-anti-CD3 antibody targeting TCR for T-cells plated onto the SLB-tension probes for 30 min before imaging. Representative images of fluorescently labelled streptavidin (A488), tension probes (Cy3B), anti-CD3 antibody (A647) and overlay images show significant co-localization of these channels (**Figure A2.9A**). Radial distribution analysis reveals significant overlap of the peak signal in all three channels (**Figure A9B**, white circle). The mean co-localization between TCR and tension probe or A488-strepatividin is calculated as a Pearson correlation coefficient (R). Pearson co-localization value for the tension probe is 0.789±0.115 and that for A488-strepatvidin is 0.785±0.150 (n = 10 cells, error bars represent S.D. of the data)

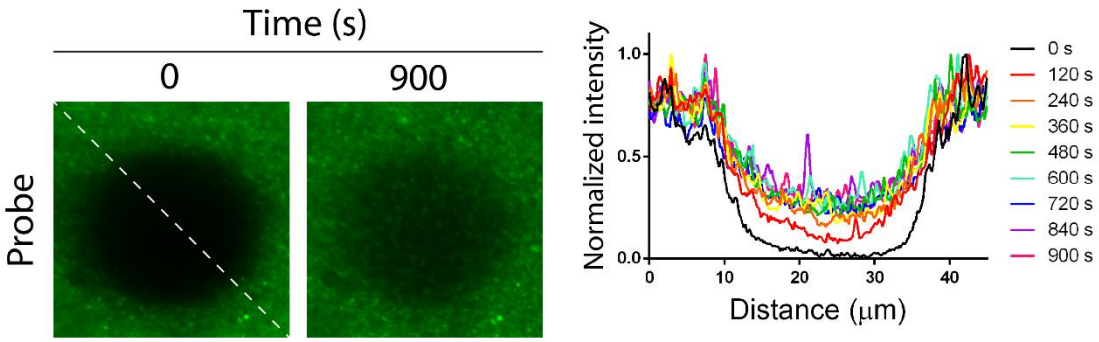

Figure A2.8. Representative FRAP images on SLBs (4% biotin, 4% Ni-NTA-DOGS and 92% DOPC). The fluorescence recovery of tension probes tethered on hindered SLB-tension probes (4% biotin, 4% Ni-NTA-DOGS and 92% DOPC) is significantly lower than that observed for the 0.1% biotin lipids. From the time course spectrum shown on the right, we observed *ca.* 40% recovery of fluorescence at t = 900 s. The retarded recovery is due to the increased molecular crowding of streptavidin and tension probes.

Table A2.1. Oligonucleotide sequences used in Chapter 2

Name	**Sequence (From 5' to 3')**
Hairpin ($F_{1/2}$ = 4.7 pN)[a]	GTGAAATACCGCACAGATGCGTTTGTATAAATG TTT TTTTCATTTATACTTTAAGAGCGCCACGTAGCCC AGC
Hairpin without stem loop	GTGAAATACCGCACAGATGCGTTTTTTAAGAGC GCC ACGTAGCCCAGC
T21A-BHQ2	/5ThiolMC6-D/TTTGCTGGGCTACGTGGCGCTCTT/3BHQ_2/
A21B	/5AmMC6/CGCATCTGTGCG GTA TTT CAC TTT/3Bio/
Complementary strand to 4.7 pN hairpin	GTATAAATGAAAAAAACATTTATAC

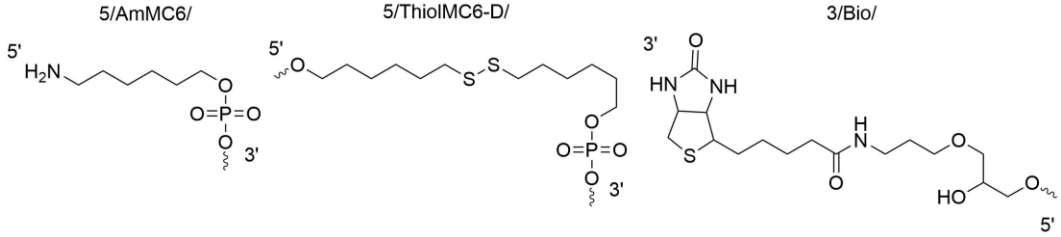

[a] Underlined bases represent the loop forming region.

Table A2.2. Dynamic light scattering to estimate the hydrodynamic radius of AuNP and AuNP-tension probes

ID	**Observed size (nm)**	**Polydispersity index (PDI)**
AuNP (14±2 nm)	25.6±0.7	0.296
AuNP-tension probe	47.4±1.8	0.287

Chapter 3

LFA-1 integrins are piconewton “mechanical rheostats” that tune T cell signaling and function

3.1. Introduction

T cells constantly scan the surfaces of antigen presenting cells (APCs) to search for cognate antigens.[151] When T cells make physical contact with APCs, the T cell receptor (TCR) recognizes the cognate peptide-histocompatibility complex (pMHC) expressed on the surfaces of APCs. Upon this initial TCR-pMHC engagement, additional ligations of co-stimulatory(inhibitory) receptors on T cells with their respective ligands on APCs collectively generates an output that defines the strength of T cell activation.[152] Because most of these receptor-ligand complexes only form productive interactions at the T cell-APC junction, we hypothesize that most of these receptor-ligand complexes experience mechanical forces and the forces generated by T cells modulate T cell signaling and function.

Recent single molecule force spectroscopy experiments suggested that TCR is a mechanosensor, where an applied force acting on the TCR-pMHC complex induces a 10-20 nm conformational extension of the TCR[153] and that triggers T cell activation.[154] Importantly, the TCR forms a "catch bond", where the TCR-agonist pMHC interaction can be stabilized with application of low pN forces and that the bond lifetime is maximized when a force of ~15 pN is applied.[34] At the single cell level, T cells also generated significant traction stress on αCD3-coated micropillar array[155] and elastomer.[156] Additionally, DNA-based force probes revealed individual TCRs transmitted 12-19 pN forces to its antigen and these forces were employed for "mechano-sampling" of the antigen quality.[157]

A second major mechanosensor used by T cells to generate productive contacts with their APCs is LFA-1, a major leukocyte integrin.[21, 158-159] In response to various biochemical inside-out activation signals, including TCR activation, this heterodimer recognizes the cell adhesion molecule ICAM-1 on both endothelial cells and on various antigen presenting cells. Among other accessory receptors on the T cell membrane, the LFA-1, when properly activated by a TCR signal, can stabilize transient T cell-APC interactions and sustain T cell activation.[160] T cells that cannot form LFA-1-ICAM-1 interactions have defective signaling capability and significantly hampered functions.[161-163] As integrin bonds are also catch bonds, the prevailing model of LFA-1 activation suggests that force transmission across the LFA-1-ICAM-1 complex facilitates conformational switching of the integrin, which couples to a separation of the cytoplasmic tails of the integrin heterodimer.[164] Laterally immobile ICAM-1 on the target cell is speculated to place the LFA-1 into an "extended-open, active state". In support of this view, constraining ICAM-1 mobility was shown to enhance T cell and NK cell functions.[113, 165] Additionally, TCR-triggered LFA-1 failed to bind to soluble ICAM-1, whereas surface bound ICAM-1 supports effective LFA-1 conformational switch and binding.[166] Recent work using a genetically encoded tension sensor (GETS) showed the LFA-1 β_2 subunit experiences ~2 pN forces at the leading edge of migrating T lymphoblasts.[71] These works collectively demonstrate that LFA-1-ICAM-1 interactions are tightly controlled by a physical mechanism that subsequently alters T cell activation and function. However, a few fundamental questions remain. For instance, how, when and where LFA-ICAM-1 complexes experience tension at the cell-cell junction?

What's the functional role of LFA-1 forces exerted by ICAM-1 on T cell activation? Do the TCR and LFA-1 mechanically communicate to generate a coordinated signal for T cell activation and function?

Herein, we employed supported lipid bilayer (SLB) technology and DNA-based molecular tension probes to dissect how LFA-1 mechanics impact T cell signaling and functions. We found that LFA-1 mediated T cell contact, adhesion and subsequent spreading are controlled by the lateral mobility of its cognate ICAM-1 ligand. Measurement with extracellular DNA-based force sensors show that T cells transmit forces to the LFA-ICAM-1 complex in the range of 4 to 19 pN, with a smaller subset of LFA-1 transmitting forces >19 pN at the periphery of actively spreading T cells. Additionally, multiplexed, spectroscopically distinct DNA force probes reveal that TCR and LFA-1 forces are spatially segregated. Lastly, by using DNA tension gauge tether (TGT) assay[90] to control the maximum forces transmitted by the LFA-1 and TCR, we found out that T cell functions can be fine-tuned by the magnitude of forces transmitted through each of these "mechanosensitive receptors". This is the first demonstration that a T cell can integrate multiple mechanical inputs to compute a signaling output.

3.2. Results

3.2.1. LFA-1 dependent T cell spreading and TCR signaling favor low ligand mobility

Traditional experiments with ligands incorporated within fluid SLBs revealed that receptor molecules on a T cell membrane undergo coordinated movement upon antigen recognition, where TCR and other molecules, including

the LFA-1 are translocated first as signaling assemblies, and later sorted into distinct zones forming the archetypical immunological synapse (IS).[17] In contrast, on professional APCs ICAM-1 molecules are properly anchored by their own cytoskeleton network, and indeed recent work suggested that LFA-1-ICAM-1 bonds are tightly regulated by mechanical inputs, as reduced lateral mobility of ICAM-1 on the surface of APCs leads to enhanced immune cell response in NK cells[113] Complementing this work, T cell response is enhanced when ICAM-1 is immobilized on substrates with optimal stiffness [167] and cytoskeletal anchorage of dendritic cell ICAM-1 facilitates T cell priming.[165] These observations led us to ask whether we could *in vitro* reconstitute the LFA-1-ICAM-1 interactions to dissect how proper ICAM-1 anchorage affects T cell adhesion and spreading (**Figure 3.1A**). We used SLB model since it recapitulates many of the chemical and physical features of the plasma membrane.[168] To tune the lateral mobility of the SLB, we generated membranes using lipids with different fluid-to-gel transition temperatures (T_m). DOPC (1,2-dioleoyl-sn-glycero-3-phosphocholine) membranes display a T_m of -17^oC while DPPC (1,2-dipalmitoyl-sn-glycero-3-phosphocholine) membranes form gel phase structures with a T_m of 41^oC. Therefore, DOPC and DPPC bilayers are chemical similar but show contrasting physical properties at 37^oC (**Figure 3.1A**). SLBs were formed by depositing small unilamellar vesicle (SUV) consisting of 99.9% DOPC (or DPPC) and 0.1% Biotinyl Cap-PE (1,2-dipalmitoyl-sn-glycero-3-phosphoethanolamine-N-(cap biotinyl) (sodium salt)) on a cleaned glass support by vesicle fusion. Truncated, biotinylated-GFP-Fc-ICAM-1 molecules (**Figure A3.1**) were tethered on the SLB *via* biotin-streptavidin

interaction to the biotinylated bilayer. The ICAM-1 density was estimated to be ~800 molecules/μm^2 on these bilayer systems using quantitative fluorescence microscopy (**Figure A3.2 and table A3.3**). The lateral mobility of ICAM-1 on these bilayers was estimated using Fluorescence Recovery After Photobleaching (FRAP), with an apparent diffusion coefficient (D) = ~1 μm^2/s on DOPC bilayers, and a minimal D on DPPC bilayers (**Figure A3.3**).

In these experiments, naïve $CD8^+$ T cells harvested from OVA-specific TCR transgenic mice (OT-1) were used. To decouple the TCR-antigen mediated adhesion from the LFA-1 triggered spreading on the SLB, we used known soluble cues to activate the LFA-1 receptors through two canonical inside-out signaling modules, including the TCR clustering □CD3ε mAb and the PKC agonist phorbol 12-myristate 13-acetate (PMA) which regulate LFA-1 conformation and clustering by recruiting cytoplasmic adaptors to the vicinity of the LFA-1 cytoplasmic tails.[169-170] A solution containing Mg^{2+}/EGTA was used to conformationally switch LFA-1 into a uniform high affinity state, bypassing inside-out signals that alter the cytoplasmic tails of LFA-1.[171] When ICAM-1 molecules were tethered on DOPC bilayer, all stimulants failed to trigger LFA-1 mediated T cell adhesion and spreading, as tracked using reflective interference contrast microscopy (RICM). Decreasing the ICAM-1 mobility using DPPC bilayer enhanced the spreading area of T cells under identical conditions (**Figure 3.1B**). At extreme, ICAM-1 anchored directly on glass surfaces initiated highly efficient LFA-1 mediated adhesion (**Figures 3.1B** and **C**). These initial results suggested that LFA-1 adhesiveness favors low mobility of ICAM-1 molecules. Constraining the mobility of ICAM-1

ligands on SLBs provides mechanical stabilization to the LFA-1-ICAM-1 interactions critical for optimal T cell adhesion and spreading.

As TCR-pMHC bonds have been suggested to be also mechanosensitive,[172-174] we next asked whether constraining the lateral mobility of antigens influences their potency for T cell activation (**Figure 3.1D**). To maximize cognate pMHC density, the biotinylated antigen (OVA-N4), which is an agonist for OT-1 cells, was incubated with the streptavidin coated DOPC- or DPPC-bilayer as stimulating surfaces to activate T cells. Here, a super-physiological density of OVA-N4 (~800 molecule/μm^2) [175] was used to challenge the cells in the absence of self-pMHCs and other auxiliary molecules, and thus, these bilayer surfaces presented a chemically identical TCR agonist that differed only in ligand mobility. When naïve OT-1 cells were incubated on the DOPC bilayer presenting OVA-N4, only minimal adhesion and spreading were observed, while limiting the long-range lateral mobility of antigen using DPPC bilayer significantly enhanced T cell adhesion and spreading (**Figure 3.1E and F**). Immunostaining of phospho-ZAP70 (pY-ZAP70), a canonical marker of proximal TCR signaling magnitude,[176-177] revealed that antigen mobility significantly altered the magnitude of early T cell signaling, which occurs downstream of the initial TCR-antigen interaction (**Figure 3.1E and G**). Notably, pY-ZAP70 signaling strength was significantly stronger when T cells interacted with OVA-N4 presented on the low mobility DPPC bilayer **(Figure 3.1G).** These data suggest that at high antigen density, engagement of multiple TCR-pMHC interactions is favored by proper anchorage, supporting the possibility that the TCR is an anisotropic mechanosensor.

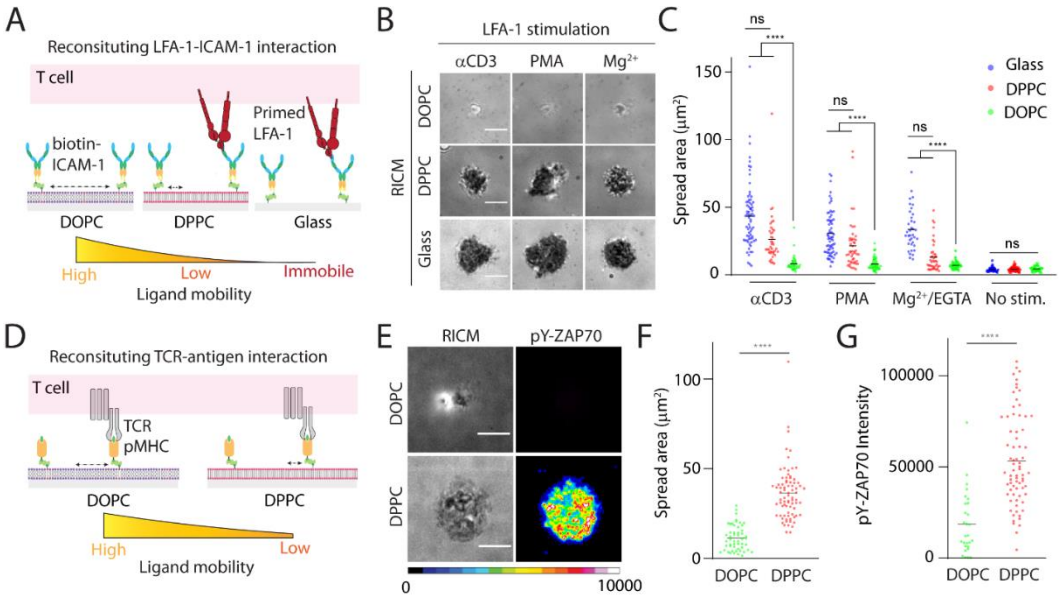

Figure 3.1. LFA-1 dependent T cell spreading and TCR mediated signaling favor low mobility ICAM-1 and pMHC. A) *In vitro* reconstitution of LFA-1-ICAM-1 interaction in lipid bilayers with either low (DPPC) or high (DOPC) lateral mobility. **B)** RICM images showing *in situ* LFA-1 primed naïve OT-1 cells spreading on substrate after ~30 min of seeding. **C)** Plot quantifying the spread area of cells on these substrates after stimulation with different agents. **D)** *In vitro* reconstitution of TCR-antigen interactions using lipid bilayers with either low (DPPC) or high (DOPC) lateral mobility. **E)** RICM and Immunofluorescence images of naïve OT-1 cells interacting with DOPC or DPPC bilayer presenting the OVA-N4 after ~30 min of plating. Cells were fixed and stained with Alexa 647-pY-ZAP70 antibody. **F)** Plot showing spread behavior of T cells on DOPC bilayer or DPPC bilayer presenting anchored OVA-N4. **G)** Plot showing pY-ZAP70 intensity of cells interacting with DOPC or DPPC bilayer presenting OVA-N4 antigen. Density of both ligands is estimated to be 800 molecules/μm^2. N > 40 cells from three different experiments. Line represents mean. ****P < 0.0001. Scale bars = 5 μm.

3.2.2. DNA-based force sensors reveal that different LFA-1 subsets transmit a spectrum of pulling forces within distinct compartments of T cells spreading on ICAM-1

Previous work using GETS has revealed the mechano-response of LFA-1 in Jurkat T lymphoblast, where a minor population of LFA-1 transmitted an average force of ~2 pN across its β_2 subunit. Given that majority of integrins have been

reported to bear forces > 50 pN,[78, 90, 178] much higher than the dynamic force range that can be reported by GETS, we hypothesize that LFA-1 may be mechanically similar to other integrin molecules. To test this possibility and also follow spatially and temporally LFA-1 mediated force generation by TCR stimulated T cells undergoing spreading, a variant of DNA-based molecular force probes[48, 179] was developed to map LFA-1 forces generated by TCR stimulated T cells interacting with ICAM-1 reconstituted directly on a glass surface (**Figure 3.2A**). Key to this approach is the use of copper-free click chemistry to covalently graft the DNA-probes onto a substrate. When a cell receptor (e.g. LFA-1 or TCR) generates forces on its cognate ligand that is $>F_{1/2}$ of the hairpin (defined as 50% probability of hairpin unfolding at equilibrium). The secondary stem-loop structure unwinds, thus separating fluorophore and quencher, and generates enhanced fluorescence signal indicating force transmission across the receptor-ligand pair of interested. As a first set of experiment, we simultaneously fused naïve CD8+ OT-1 T cells with soluble αCD3 onto substrates presenting ICAM-1 coated DNA-based force probes with a $F_{1/2}$ of 4.7 pN. Cell spreading, and tension signals were tracked using RICM and epi-fluorescence microscopy, respectively. After ~3-4 min of incubation, OT-1 cells engaged and spread on the tension probe substrate and generated force signals underneath the cell contact area. As control experiments, non-stimulated cells did not engage and spread. Also, αCD3 primed cells spread on a control tension probe substrate, which is comprised of a DNA duplex lacking the hairpin stem-loop, but were unable to generate fluorescence enhancement (**Figure 3.2B and Figure A3.4 for analysis pipeline**). Next, to better define the magnitude of LFA-1 forces, we

allowed the T cells to adhere onto hairpin probes with a $F_{1/2}$ of 19 pN. Surprisingly, although the cell adhesion footprint was similar to the cells on 4.7 pN probes, T cells generated tension exclusively at the periphery. Further qualification revealed that only ~0.5% of the 19 pN hairpin probe were unwound underneath the cell, whereas a total of ~5% of 4.7 pN probes were occupied and stretched by the LFA-1 receptors (**Figure 3.2C**). These results reveal increase in fluorescence signal is a direct consequence of LFA-1 force transmission to the ICAM-1 ligand, with a very minor population of LFA-1 molecules, probably high affinity LFA-1-ICAM-1 bonds, that can generate forces >19 pN during spreading and migration.

To study the force evolution during initial adhesion, spreading and migration mediated by LFA-1, we acquired 10 min time-lapse sequences capturing the spatiotemporal changes of the LFA-1 generated forces with an interval of 20 s (**Figure 3.2D**). The mean intensities underneath the T cells at each time point were normalized to the highest intensity within the sequence. From time-lapse videos, we identified T cells experience changes in phases during ligand sensing by LFA-1. Within the first 3-4 min of cell plating, αCD3 primed cells engaged with the 4.7 pN ICAM-1 tension probes, and first generated forces at the center of the cell-surface contact accompanied with spreading. The distribution of the LFA-1 force was highly dynamic after the initial spreading phase. Interestingly, T cells started to generate highest forces mostly at the cell periphery while forming random migration within confined areas (**Figure 3.2E and Figure A3.5**). Analysis of the force signals at the cell-substrate contact also indicated two phases of tension evolution□a rapid increase in force signal during the initial adhesion and spreading,

followed by a stable phase when cells started to randomly migrate on the substrate (**Figure 3.2F**).

Actomyosin forces have been proposed to stabilize the LFA-1-ICAM-1 interaction by unclasping the integrin heterodimer.[180-181] Therefore, we challenged αCD3-primed cells with the 4.7 pN tension probes to measure the effect of cytoskeletal perturbation on the LFA-1 forces. Inhibition of myosin II activity using blebbistatin did not abolish cell spreading and the LFA-1 forces. On the other hand, stabilization of actin turnover by jaspakinolide completely eliminated cell spreading and prohibited the LFA-1 force generation. Collectively, these results support the hypothesis that actin protrusion, rather than myosin contractility, is the primary driver for LFA-1 mediated T-cell spreading, motility and tension generation (**Figure A3.6**).

We next directly compared the efficacy of different LFA-1 activation cues in inducing LFA-1 force transmission. As shown above, physiological activation with TCR ligation triggered LFA-1 mediated T cell spreading on the ICAM-1 force sensors and the mean tension signals were significantly higher than with other stimulants. PMA-primed cells were migratory (**Figure A3.5**), and they generated tension exclusively at the cell periphery, albeit the mean tension signals were significantly lower than those of TCR primed T cells. While artificial Mg^{2+}/EGTA LFA-1 activation induced strong cell adhesion and minimal motility, consistent with inability of the LFA-1 bonds to properly detach (**Figure A3.5**). Notably, this artificially activated LFA-1 generated the weakest tension signals reflecting inadequate coupling of the artificially activated LFA-1 to the cytoskeleton (**Figures**

3.2G and H). To dissect the spatiotemporal profile of the force bearing LFA-1 molecules that are induced by these distinct stimulants, we performed a spatial analysis where the LFA-1 forces at the lamellipodia of the cells are directly compared to that at the center (**Figure A3.7**). Interestingly, αCD3 primed LFA-1 molecules produced a low edge-to-center tension ratio (<1) when compared to that of PMA primed LFA-1 molecules (~2.1). LFA-1 activated by artificial conformational stabilization also generated a low edge-to-center ratio that was due to low tension intensity close to background (**Figure A3.2I**). These results indicated that only when the LFA-1 heterodimers were properly activated by TCR and triggered recruitment of cytoskeletal adaptors, these heterodimers, once bound by anchored ICAM-1, can exert high forces on individual ICAM-1 molecules at the interface of T cell-substrate contact.

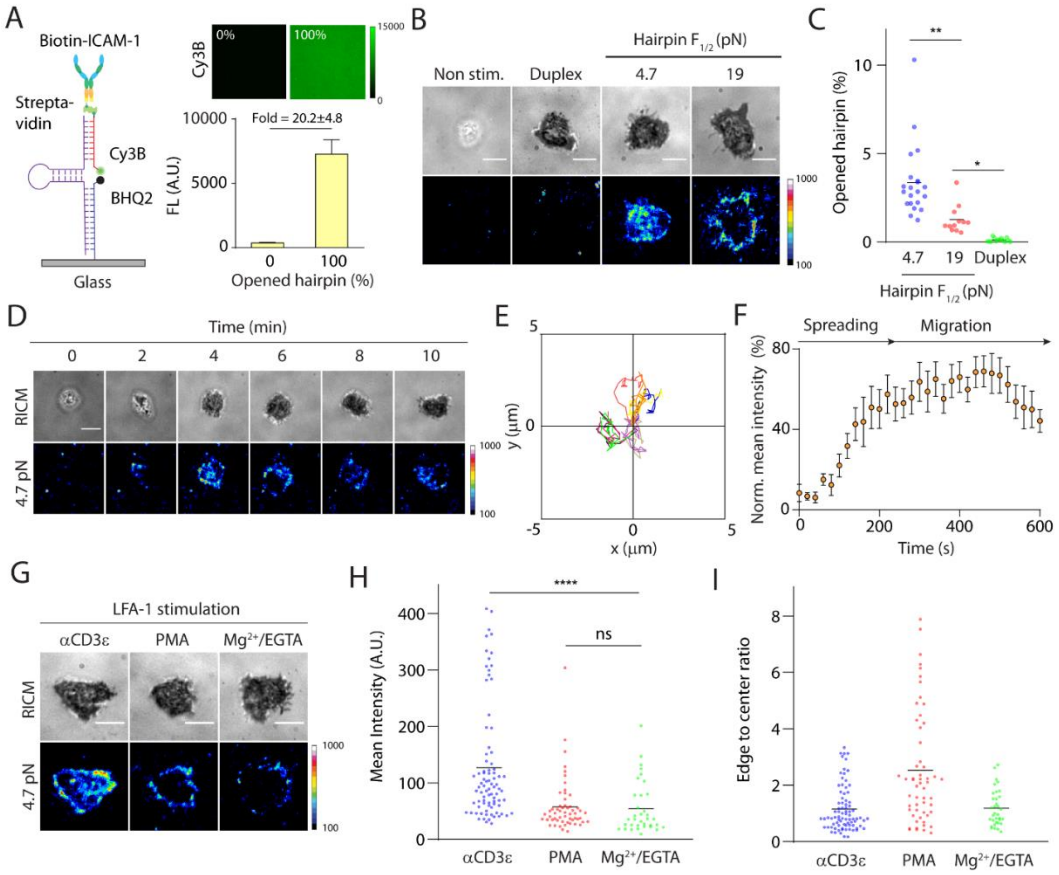

Figure 3.2. Extracellular DNA-based LFA-1 tension probes. A) Design and qualification of covalently grafted ICAM-1-DNA-based tension probes. **B)** RICM and tension images show *In situ* αCD3 primed naïve OT-1 cells spread and generated tension on probes with $F_{1/2}$ of 4.7 pN or 19 pN after ~15-20 min of plating. Controls include non-primed naïve OT-1 cells (non stim.) and αCD3 cells on control DNA-probes that lack hairpin stem-loop (duplex). **C)** Plot showing average hairpin opening underneath the cell-substrate contact. N>20 cells from three independent experiments. **D)** Time lapse RICM and tension images showing initial landing of an *In situ* αCD3 primed cell. **E)** Displacement plot showing cell tracks of 10 randomly selected αCD3 primed cells on the tension probe substrates within 10 min. **F)** Average LFA-1 tension evolution profile generated from 10 randomly selected αCD3 primed cells landing on the 4.7 pN tension probe substrates within the first 10 min. Error bar represents SEM. **G)** RICM and tension images showing *in situ* primed cells with different agents after ~15-20 min of cell plating. **H)** Plot qualifying the mean tension intensity underneath the cell-substrate contact. **I)** Plot qualifying the ratios of the edge tension to the central tension. N > 40 cells from three independent experiments. ****P < 0.001. Scale bars = 5 µm.

3.2.3. Multiplexed DNA based tension probes report spatiotemporal dynamics of TCR and LFA-1 forces

We next developed multiplexed DNA force probes to ask how the LFA-1 forces compare to TCR tension in terms of location and timing when both LFA-1 and TCR ligands are anchored. We generated ICAM-1 and OVA-N4 tension probes that were spectrally encoded by Cy3B and Atto647N reporters, respectively (**Figure 3.A**). Naïve OT-1 cells seeded on the multiplexed probe surfaces generated highly distinct force patterns, where the LFA-1 forces were primarily found at the cell edge and the TCR-pMHC bonds primarily experienced forces at the focal zone in migrating cells (**Figure 3.3B**). Line scan (**Figure 3.3C**) showed the force signals from these two channels were spatially segregated. To exclude the possibility that this difference was due to artifacts from surface preparation, we labelled the OVA-N4 ligands onto both Cy3B and Atto647N probes and found that the force responses from both channels were highly colocalized and none of the cells formed a motile phenotype. This spatial segregation could be explained by that TCR is presented on the microvilli for active antigen scanning[182-183] while TCR stimulated LFA-1 is on the plasma membrane. Single color imaging of LFA-1 force with surface immobilized antigen additionally confirmed that the observed ring pattern of mechanically activated LFA-1 was not due to imaging artifact (**Figure A3.8**). This result demonstrated the first multiplexed pN force map for TCR and LFA-1, highlighting temporally coordinated mechano-communication of these two receptors at distinct compartments of actively spreading TCR stimulated T cells.

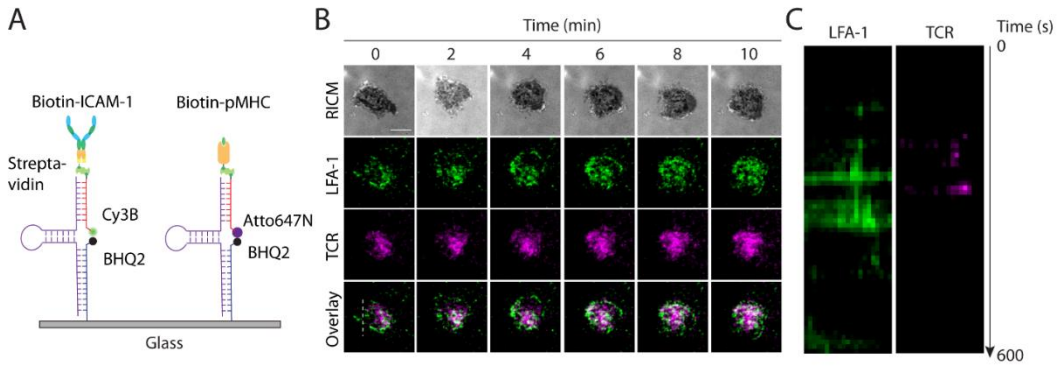

Figure 3.3. Spectrally encoded, multiplexed extracellular DNA-based TCR and LFA-1 tension probes. A) Design of multiplexed real time DNA-based tension probes for simultaneous mapping of TCR and LFA-1 forces. **B)** Time lapse images showing cell footprint and spatial segregation of the LFA-1 and TCR forces. Representative RICM and tension maps of the LFA-1 ($F_{1/2}$ = 4.7 pN, green), TCR ($F_{1/2}$ = 4.7 pN, magenta) and the overlay channel of a single OT-1 cell were shown. Scale bar = 5 μm. **C)** Kymograph displays tension signals generated by the LFA-1 (green) and the TCR (magenta) as a function of time within the line of interest in shown in the overlay channel in **B)**.

3.2.4. Mechanochemical stabilization of LFA-1-ICAM-1 bonds potentiates TCR triggered T cell activation

Using tension gauge tether (TGT) assay,[90] we examined the mechanical requirements for LFA-1 activation in the absence of surface anchored TCR ligand. TGTs are comprised of ligand-tethered DNA duplexes that rupture under sufficient receptor forces and report the minimum force requirement for receptor activation (**Figure 3.4A**). αCD3ε primed OT-1 cells were seeded on ICAM-1-TGT surface with tension tolerance (T_{tol}) of 12 pN or 56 pN, and were immunostained for pY-ZAP70 (**Figure 3.4B**). 56 pN ICAM-1 TGTs triggered more aggressive spreading than the 12 pN TGTs (**Figure 3.4C**), supporting our earlier results that TCR stimulated LFA-1 can transmit forces >19 pN on the ICAM-1 ligand. Interestingly, phosphorylation of ZAP-70 was markedly potentiated by LFA-1 forces, since T

cells seeded on 56 pN-ICAM-1-TGTs displayed significant pYZAP-70 recruitment all over the membrane surface, while T cells on 12 pN showed only minimal pYZAP-70 activity (**Figure 3.4D**). Thus, LFA-1 forces >12 pN, which stabilize a subset of high affinity LFA-1-ICAM-1 bonds, deliver a mechano-chemical feedback loop to enhance TCR mediated T cell signaling. To validate that these TGTs are functional with new attachment chemistry, we also generated N4-TGTs with T_{tol} = 12 and 56 pN and observed differential ZAP70 phosphorylation levels also on these force sensitive TCR ligands (**Figure A3.9**)[157], confirming our previous results. Furthermore, when T cells were immunostained for *F*-actin, cells seeded on neither the 12 pN or 56 pN N4-TGT probes developed a cortical actin ring. Surprisingly, the actin ring exceeded the spread area of cells on 12 pN TGTs (**Figure A3.10**) suggesting that initial traction forces >12 pN were generated to sample antigens and that caused rupture of the 12 pN TGT probes, leading to shrinkage of the cell contact.

To further confirm that the inability of T cells to signal is due to probe rupture, we next designed turn-on TGT assay where a fluorophore and quencher are attached to the TGT probes (**Figure A3.11**).[94-95] Cells generated a strong ring like turn-on signal associated to probe rupture when seeded on 12 pN N4-TGTs, but not the 56 pN TGTs (**Figure A3.11**). The ring size was highly similar to the spread area of cells seeded on 56 pN-N4 TGTs, confirming that the TCR generates >12 pN contractile forces to sample antigen (**Figure A3.11**). Additionally, αCD3 primed cells were also able to mechanically rupture the 12 pN ICAM-1-TGTs, but

not the 56 pN ICAM-1 TGTs, at the cell edge. These results indicate that both TCR and LFA-1 transmit forces >12 pN to enhance ZAP-70 signaling.

We then asked whether LFA-1-ICAM bonds can mechanically amplify the TCR signaling initiated by surface anchored agonist. To test this hypothesis, we generated surfaces presenting both the OVA-N4 and ICAM-1. The ICAM-1 was anchored through the TGT to the surface and the OVA-N4 was directly immobilized on the glass surface (**Figure 3.4E**). We systematically tuned the OVA-N4 density from ~0.1 to 100 molecules/μm^2, while keeping the density of ICAM-1-TGT constant (~1000 molecules/μm^2). As a control, we generated surfaces only presenting varied density of antigens. Naïve OT-1 cells were seeded on these surfaces for 1h, and were immunostained for pY-ZAP70. For surfaces without ICAM-1 molecules, cells minimally adhered and spread even at the highest antigen density (**Figure 3.4G and Figure A3.12**). Similarly, pY-ZAP70 level was significantly retarded (**Figures 3.4F and H**) This result indicated that at physiologically relevant densities of antigens, TCR-pMHC bond alone could not support efficient cytoskeletal remodeling and TCR signaling without co-signaling from LFA-1-ICAM1 bond. Indeed, co-presentation of ICAM-1 on TGT probes with surface immobilized TCR agonist dramatically changed T cell responses. Inclusion of ICAM-1 tethered through 56 pN-TGT dramatically increased OT-1 spreading and pY-ZAP70 level at ~100 antigens/μm^2, and these responses dropped as a function of antigen density, reaching lowest responses at ~0.1 antigen/μm^2 (**Figures 3.4F-H and A3.12**). ICAM-1 tethered through 12 pN-TGT resulted in enhancement of both spreading and pY-ZAP70 level at the highest antigen density,

albeit to a lesser extent compared to 56 pN ICAM-1-TGT, as a larger fraction of LFA-1-ICAM-1 bonds were mechanically liable. A similarly decreasing trend was observed, but both the spreading and pY-ZAP70 responses dropped to the lowest level at ~1 antigen/μm^2 (**Figures 4F-H and A3.12**).

The pY-ZAP70 levels of T cells seeded on surfaces co-presenting antigen and ICAM-1-TGTs to those seeded on antigen only surfaces were directly compared. Fold enhancement of pY-ZAP70 measures the strength of mechanical sensitization from LFA-1-ICAM-1 bond to the TCR signaling. As shown in **Figure 3.4I**, 56 pN ICAM-1-TGT promoted ~4 to 4.2-fold increase of pY-ZAP70 level at higher antigen densities (10-100 antigens/μm^2), while this response dropped to ~1.3 fold at 0.1 antigen/μm^2. Similarly, ZAP70 signaling was also enhanced with the use of 12 pN ICAM-1 TGT, despite of the fact that only ~3 to 3.5 fold of signal enhancement were observed at the antigen densities of 10-100 10-100 molecules/μm^2. Surprisingly, the signal gain from LFA-1-ICAM-1 interaction was completely abolished at ~1 antigen/μm^2. Curve fitting of these results yielded apparent EC_{50} (pY-ZAP70) = ~3.1 antigens/μm^2 for cells seeded 12 pN-ICAM-1 TGT surfaces, while this value was ~6-fold lower for cells seeded on 56 pN-ICAM-1 TGT surfaces, with EC_{50} (pY-ZAP70) = ~0.5 antigens/μm^2 (**Figure A3.13**). Nevertheless, at this very low OVA-N4 density, high density ICAM-1 could still markedly enhance the sensitivity of TCR sampling even when both molecules were presented on a high mobility DOPC-bilayer (**Figure A3.14**). Collectively, these results suggest that a successful mechanical-chemical feedback loop between TCR

and LFA-1 requires mechanically stabilized high affinity LFA-1-ICAM-1 bonds, and that these bonds can tune the antigen dose required for optimal T cell activation.

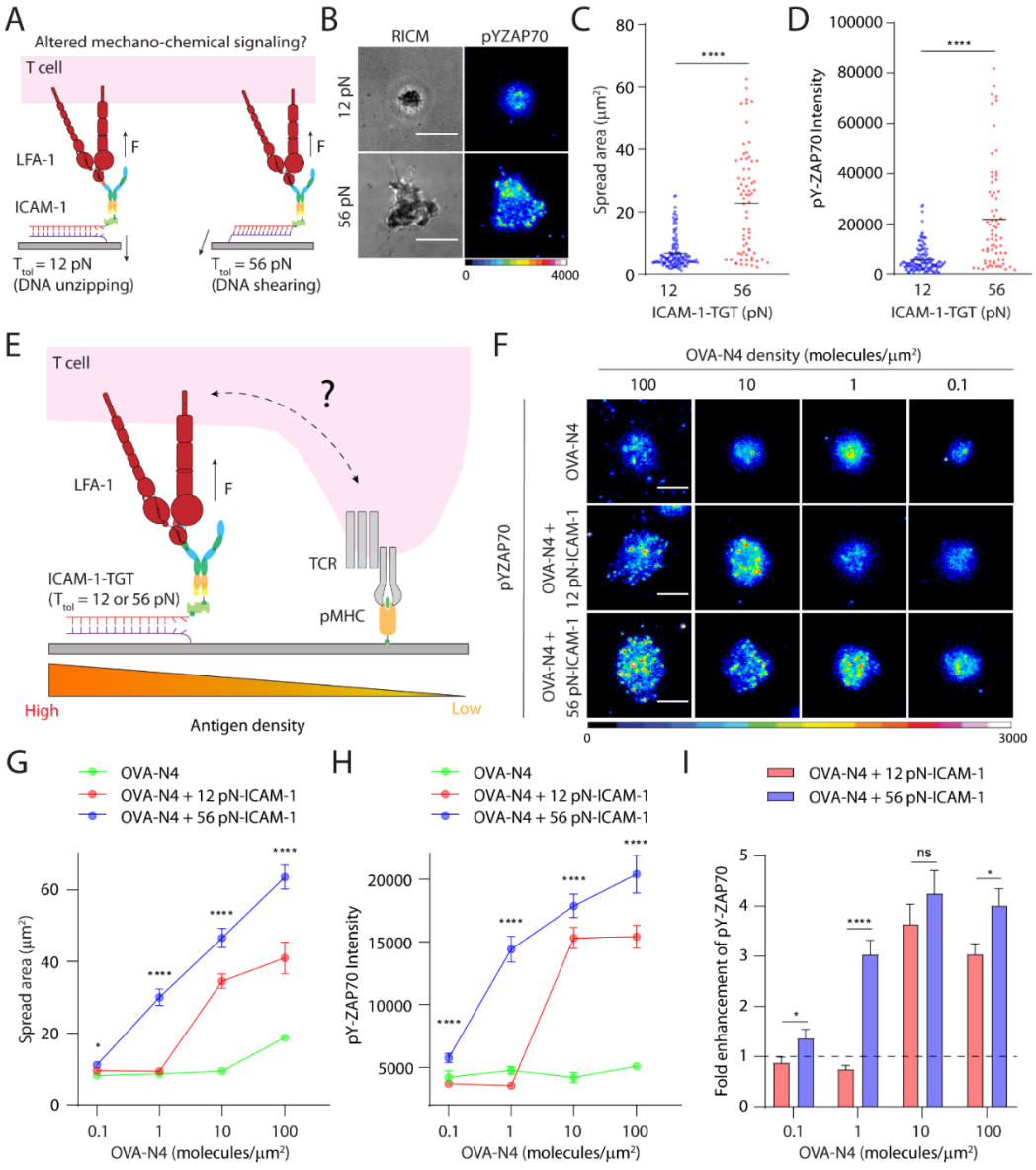

Figure 3.4. A) Schematic showing the design of TGT assays to cap maximal forces that can be transmitted to LFA-1-ICAM-1 bonds. **B)** RICM and immunofluorescence images showing *In situ* αCD3 primed naïve OT-1 cells spread on ICAM-1-TGT substrates after 1 h of incubation. Cells were stained with Alexa 647-pY-ZAP70 antibody. **C and D)** Quantification of spread area and pY-ZAP70 intensity of cells seeded on 12 pN or 56 pN ICAM-1 TGT substrates. N>50 cells from three independent experiments. **E)** Schematic showing the design of multifunctional surfaces presenting both ICAM-1 ligands (through the TGT) and immobilized agonist pMHC. **F)** Immunostaining for pY-ZAP70 of cells seeded on

surfaces coated with immobilized OVA-N4 (control), immobilized OVA-N4 and 12 pN ICAM1-TGT, or immobilized OVA-N4 and 56 pN ICAM-1-TGT. Antigen densities were varied from ~0.1 molecules/μm^2 to ~100 molecules/μm^2. **G) and H)** Quantification of spread area and pY-ZAP70 intensity of cells seeded on OVA-N4 only, OVA-N4 and 12 pN ICAM-1 TGT or OVA-N4 and 56 pN ICAM-1 TGT substrates**. I)** Plot showing enhancement of pY-ZAP70 intensity of cells seeded on OVA-N4 and 12 pN ICAM-1 TGT or OVA-N4 and 56 pN ICAM-1 TGT substrates compared to those on antigen only surfaces. ICAM-1 density is estimated to be ~1000 molecules/μm^2. *P<0.05, ****P<0.0001. N>30 cells from two independent experiments.

3.2.5. Mechanical communication between TCR and LFA-1 augments T cell signaling and function

In light of the potential mechano-communication mechanism between TCR and LFA-1, we next developed multiplex tension array where the N4 and ICAM-1 ligands were spatially encoded with a unique T_{tol} through the TGT, resulting in 4 (2^2) possible scenarios (**Figure 3.5A**). Cells seeded on a combinatorial surface with 12 pN-N4, 12 pN-ICAM-1 TGTs had the lowest adhesion areas and pY-ZAP70. When 56 pN-TGT was employed to present the ICAM-1, cells had larger spread areas and enhanced pY-ZAP70 (**Figures 5B-D**), suggesting that mechanically stable LFA-1-ICAM-1 bonds enhance T cell spreading and TCR signaling. Interestingly, co-presentation of ICAM-1 ligands did not further enhance T cell spreading, and pY-ZAP70 induction when both the antigen and ICAM-1 were tethered through TGTs with highest mechanical tolerance (56 pN).

We then used the multiplexed tension array to test whether mechanical communication between TCR and LFA-1 impacts cytokine generation. Consistent with our immunostaining experiment, cells cultured on a combinatorial surface with 12 pN-N4 and 12 pN-ICAM-1 generated the least IL-2 cytokine compared to other combinations of TCR agonist and ICAM-1. IL-2 was linearly produced at

early time points and was used to estimate the rate of secretion (**Figure 5E**). Surprisingly, we found that despite pY-ZAP70 levels were significantly different when seeded on single component N4-TGTs with drastically different mechanical tolerances (**Figure A3.9**), T cells produced similar amounts of IL-2 at 6 h and 12 h regardless of the mechanical tolerance of the TCR ligand (**Figure A3.15**). Nevertheless, aCD3 primed cells seeded on the 56 pN ICAM-1 TGTs generated trace amounts IL-2 that is statistically higher than those seeded on 12 pN ICAM-1 TGTs, further suggesting the contribution of mechanosensitive LFA-1-ICAM-outside in signaling to TCR signaling (**Figure A3.15**).

We next directly compared the slopes of IL-2 secretion of these combinatorial surfaces to that of single component N4-TGTs (**Figure A3.5F**). For surfaces encoded with 12 pN-N4 TGT, inclusion of 12 pN-ICAM-1 only had a minimal impact on the ΔIL-2, while the 56 pN-ICAM-1 sensor enhanced the rate of IL-2 generation by ~50%. Interestingly, incorporation of 12 pN-ICAM-1 and 56 pN-ICAM-1 TGT on the 56 pN-N4 TGT surfaces increased the rate of IL-2 generation by ~30% and 50%, respectively (**Figure A3.5F**). These results suggest that cytokine generation, which is a measure of the magnitude of T cell activation, is also dependent on the ability of both TCR and LFA-1 to mount optimal tension on their respective ligands. Collectively, our proximal TCR signaling and cytokine outputs results suggest that LFA-1 generated forces potentiate both the early T cell signaling events at the T-APC contact and the subsequent gene transcription programs culminating in IL-2 production, the hallmark of T cell activation and proliferation.

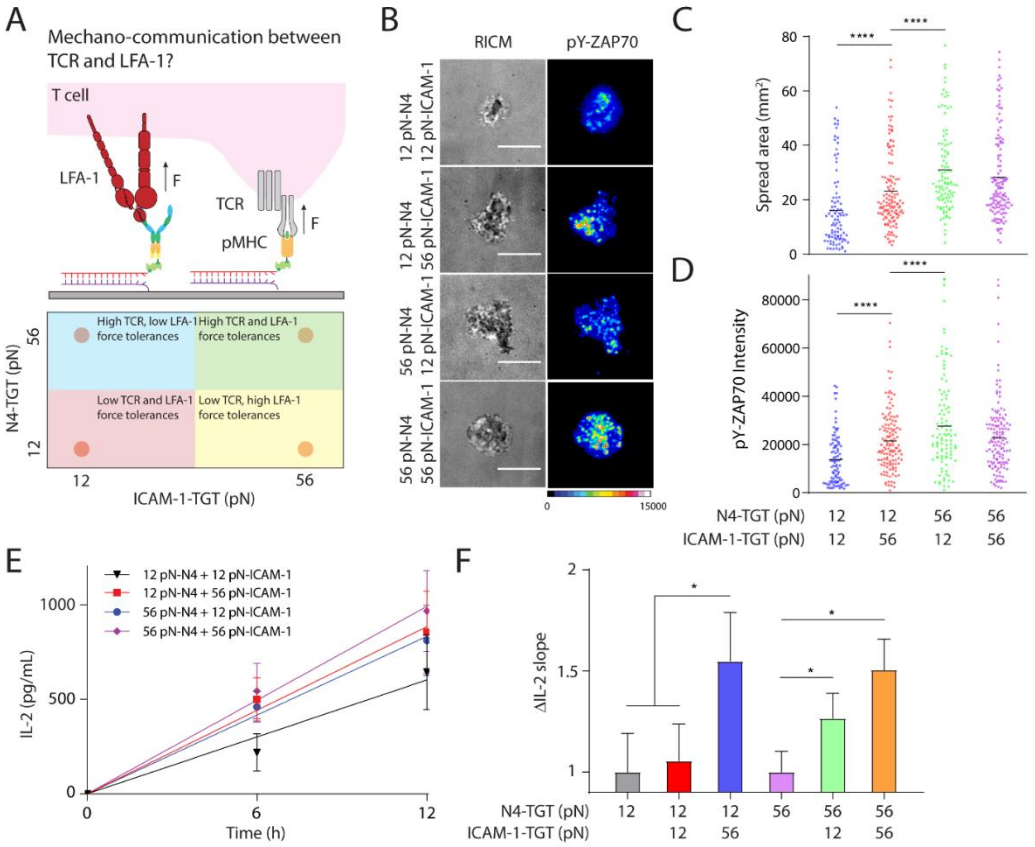

Figure 3.5. A) Multiplexed tension array to cap maximal forces that can be transmitted through the TCR-antigen and LFA-1-ICAM-1 bonds. **B)** RICM and immunofluorescence images showing naïve OT-1 cells spread on these multiplexed TGTs after 1 h of incubation. Cells were stained with Alexa 647-pY-ZAP70 antibody. **C and D)** Quantification of spread area and pY-ZAP70 intensity of cells seeded on multiplexed TGT substrates. N > 100 cells from three independent experiments. **E)** Plot showing the IL-2 concentration generated by cells seeded on multiplexed TGT substrates after 6 and 12 h. **F)** Quantifying the rate of IL-2 generation by comparing the slope to cells seeded on single component, antigen coated TGTs. Three independent experiments for E and F. Line represents mean and error bar represents SD. *P<0.05, ****P<0.0001. Scale bars = 5 µm.

3.3. Discussion and conclusion

Precise modulation of LFA-1 affinity and avidity by TCR signaling is important for the stoppage of highly motile T cell on various APCs.[184] At the same time, TCR-activated LFA-1 allows formation and maintenance of durable T cell-APC IS, which can lower the threshold of TCR signals required for T cell activation. The IS is often generated by segregated assemblies of TCR-pMHC and of LFA-1-

ICAM-1 bonds that are redistributed into distinct zones of the T-APC contact or T cell contact with SLB reconstituted with LFA-1 and TCR ligands.[17, 185-186] Using SLB as a model platform, we demonstrate that TCR signal (triggered by αCD3 crosslinking) is insufficient to trigger strong LFA-1-ICAM-1 anchorage on fluid membrane, but readily drives LFA-1 bond formation with immobile ICAM-1. Additionally, antigen presented within fluid SLB does not provide stable anchor for the TCR and also fails to support productive T cell signaling. These results further support the conclusion that TCR and LFA-1 are both mechanosensors and that they optimally deliver T cell activation signals if occupied by mechanically tolerant, properly anchored ligands.

We are the first to determine both spatially and temporally how the LFA-1 integrin of primary T cells transmits forces to anchored ICAM-1 by using novel DNA-based tension probes of ICAM-1. TCR-triggered LFA-1 transmit molecular forces to the ICAM-1 ligands with magnitudes from >4.7 pN, with a subset of receptors, possibly high affinity LFA-1-ICAM-1 bonds, that experience forces > 19 pN. Our measurements of LFA-1 transmitting forces, in the range of 4.7 pN, are consistent with an earlier report that showed intermediate affinity LFA-1 experiences ~2 pN force during T cell migration[71]. Our results are also consistent with the work by Zhu and co-workers which measured a catch LFA-1-ICAM-1 bond with ~15 pN strength apparently critical for high affinity acquisition of this interaction.[187] Further TGT experiments with ICAM-1 showed that these are the high tension LFA-1-ICAM-1 bonds rather than the low tension bonds that potentiate TCR signaling and enhance antigen sensitivity Our results are therefore

a first demonstration of a mechanochemical feedback loop to enhance TCR signaling and T cell activation by a small subset of high affinity LFA-1-ICAM-1 bonds at the immune synapse.

Under physiological conditions, surface receptors on T cells work cooperatively to form long lived IS or short lived kinapses that tune T cell signaling and response.[188] Attempts to dissect the crosstalk between TCR and LFA-1 were made with micropatterned substrates and confirmed that LFA-1-ICAM-1 bonds enhance traction forces of T cells.[189] We developed multiplex tension probes and tension array to study mechanochemical feedback between these two receptors, and found that both the TCR and LFA-1 applied forces to their cognate ligands and thereby modulate T cell signaling, activation and function. Since the LFA-1 and TCR compartments are spatially segregated and are also biochemically distinct, and since TCR signals positively regulate LFA-1 binding to ICAM-1, their distinct mechanically linkages to the cortical actin cytoskeleton seems to provide a persuasive mechanism for this precise control.[172] Previous work demonstrated that the LFA-1 cytoplasmic tails are associated with specific cytoskeletal adaptor proteins such as talin, vinculin and kindlin that connect LFA-1 to the actin cytoskeleton,[190-191] while TCR may be linked to cortical actin with an entirely different set of adaptor proteins such as Nck, VAV and WASp.[192]

Based on these findings, we propose a working model to explain how T cell signaling and function are potentiated by the mechanochemical feedback loop between the TCR and LFA-1 (**Figure 3.6**). Initial TCR-antigen interaction between a T cell and an APC triggers downstream signaling for T cell activation and an

"inside-out" signaling that primes the LFA-1 into a conformation that is able to bind ICAM-1. Properly anchored ICAM-1 allows efficient force transmission from the actin cytoskeleton to LFA-1-ICAM-1 bonds, further stabilizing this interaction by "catch bond". The high tension LFA-1-ICAM-1 bonds promote downstream signaling for cytoskeletal remodeling and supply additional biochemical signals that further potentiate T cell signaling. For instance, the LFA-1-ICAM-1 can generate signal through the ZAP-70 and that was reported to regulate Jurkat T migration and may converge with TCR signaling to amplify the extent of T cell activation. Nonetheless, our results strongly suggest that these distinct assemblies, although spatially distinct, can converge mechanical signals from integrins and TCRs to control optimal T cell activation, proliferation, and differentiation.[193] It would be interesting to test how different integrin adaptors recruited by low and high tension LFA-1-ICAM-1 bonds communicate with different TCR assemblies. Another open question for future studies is whether LFA-1 and other integrins can similarly amplify in a mechano-regulated manner signaling cascades triggered by other immunoreceptors such as the B cell receptor[79, 194-195] and Fc-receptors.[196]

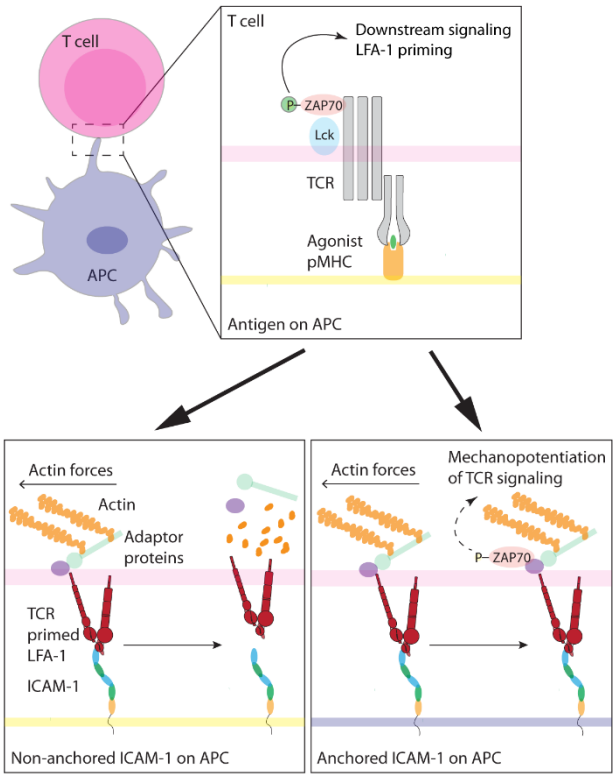

Figure 3.6. Working model of a potential mechano-communication mechanism between TCR and LFA-1 to amplify T cell signaling. Initial TCR-antigen encounter triggers TCR signaling that primes LFA-1 into intermediate conformation. Binding of the TCR-primed LFA-1 to ICAM-1 requires formation of a mechanically stable bond that provides a mechanochemical feedback loop to potentiate TCR signaling.

3.4. Materials and methods

3.4.1. Reagents

Reagents, unless otherwise specified, were purchased from Sigma Aldrich (St. Louis, MO) and used as received. All solvents were of analytical grade and purified as needed. No. 1.5H coverslips (#10812) and sticky-Slide VI 0.4 (#80608) were purchased from Ibidi (Fitchburg, WI) Cy3B-NHS ester (#PA63101) was purchased from GE Healthcare Life Sciences (Pittsburgh, PA). Azide-PEG_4-NHS ester (#AZ-103) was obtained from Click Chemistry Tools (Scottsdale, AZ). RPMI and DMEM medium (#10-103-CV), heat inactivated FBS (#35-015-CV), penicillin-streptomycin solution (#30-234-CI) and gentamicin sulfate solution (#30-005-CR)

were purchased from Corning Mediatech (Corning, NY). 1,2-dioleoyl-sn-glycero-3-phosphocholine (DOPC, #850375C) and 1,2-dipalmitoyl-sn-glycero-3-phosphocholine (DPPC) were purchased from Avanti Polar Lipids Inc. (Alabaster, AL). Texas Red-DHPE (#23301) was purchased from AAT Bioquest (Sunnyvale, CA). Oligonucleotides (Table S1) were obtained from Integrative DNA technologies (Coralville, IA) and were purified either by reverse-phase HPLC or standard desalting. Transfection grade linear polyethylenimine (#23966-1) was purchased from Polysciences, Inc. (Warrington, PA). All buffer solutions were made with MilliQ water (18.2 MΩ cm^{-1}) and passed through a 0.2 μm filtration system.

3.4.2. Antibodies

Purified anti-mouse CD3ε (clone 145-2C11, #100302) was purchased from BioLegend (San Diego, CA). Alexa Fluor® 647 Mouse Anti-ZAP70 (PY319)/Syk (PY352) (#557817) was obtained from BD biosciences.

3.4.3. General Experimental

Concentrations of purified oligonucleotide conjugates and the ICAM-1 proteins were determined on a Nanodrop 2000 UV-Vis Spectrophotometer (Thermo Scientific). MALDI-TOF Mass Spectrometry was performed on a high performance MALDI time-of-flight mass spectrometer (Voyager STR). Matrix for DNA analysis was prepared by freshly dissolving excess 3-hydroxypicolinic acid

(3-HPA) in the solvent (50% MeCN/H_2O, 1% TFA, 10% of 50 mg/mL ammonium citrate).

3.4.4. Oligonucleotide synthesis

The strand is prepared following a reported protocol. In brief, A mixture of A21B (10 nmol) and excess Cy3B-NHS ester or Atto647N-NHS ester (50 µg) in 0.1 M sodium bicarbonate solution (pH = 9) was allowed to react at room temperature overnight. The mixture was then subjected to P2 gel filtration to remove salts, organic solvent and unreacted reactants, and was further purified by reverse phase HPLC (solvent A: 0.1 M TEAA, solvent B: 100% MeCN; initial condition was 10% B with a gradient of 1%/min, flow rate: 1 mL/min). The product was characterized by MALDI-TOF mass spectrometry.

3.4.5. OT-1 cell harvesting and purification

OT-1 T cell receptor transgenic mice were housed and bred in the Division of Animal Resources Facility at Emory University in accordance with the Institutional Animal Care and Use Committee. OT-1 T cells express the CD8 co-receptor and specifically recognize chicken ovalbumin epitope 257–264 (SIINFEKL) in the context of the MHC allele H-2K^b. Naïve, OT-1 T cells were enriched from the spleen using magnetic activated cell sorting according to manufacturer instructions provided with the CD8a+ T cell Isolation Kit (Miltenyi Biotec, Germany). Briefly, a single cell suspension of splenocytes was obtained and incubated with biotinylated antibodies specific for unwanted splenic cell populations. These

populations were separated from the OT-1 T cells following incubation with anti-biotin magnetic beads and enrichment on a magnetic column. Purified T cells were washed and resuspended in HBSS solution and kept on ice before experiment.

3.4.6. Plasmids

The monomeric and dimeric ICAM-1-sfGFP constructs (see amino acid sequences in **table A3.2**) were ligated to the LentiORF pLEX-MCS Vector (Thermo Scientific) with the help from the Emory Integrated Genomics Core.

3.4.7. Lentiviral production and generation of stable expressing soluble, biotinylated-recombinant mouse ICAM-1 cell lines

HEK293FT cells for lentivirus production were maintained in complete DMEM [10% FBS, penicillin G (100 IU/mL), streptomycin (100 µg/mL)] at 37 ^{o}C with 5% CO_2. Lentivirus particles were produced HEK293FT cells in 1X T225 flasks by co-transfection of the pLEX transfer plasmid with the 2nd generation packaging plasmids pMD2.G and psPAX2 (a gift from Didier Trono, Addgene plasmid #12259 and #12260) using linear polyethylenimine (MW = 25,000). The particles were harvested from the supernatant 60−72 h post-transfection, filtered and concentrated into ~250 µL in D20 media (DMEM + 20% FBS) by ultracentrifugation or Amicon® centrifugal filters and stored in -80^{o}C before use.

For lentiviral transduction, ~20,000 TB-15 cells (a variant of HEK293T cells stably expressing BirA biotinylating enzyme, a gift from Prof. John Altman and Dr. Richard Willis from the NIH Tetramer Core Facility at Emory University) was

seeded onto a 96 well cell culture plate. On the next day, ~50 µL of concentrated lentivirus particles were added to the cells. After 6 h of infection, the media was exchanged to complete DMEM. Transduced cells were expanded to appropriate density before adaptation to suspension culture. We use the FreeStyle 293 expression media supplemented with 200 µM of D-biotin for direct adaptation in a shaking incubator (8% CO_2, shaking speed = 135 rpm). Soluble ICAM-1 molecules were collected from the supernatant every 3 days or when the cell density reached ~1,000,000 cells/mL.

3.4.8. Purification of biotinylated ICAM-1s from suspension culture

The harvested supernatant was centrifuged for 5 min at 1,200 rpm to pallet the cells. The supernatant was then carefully removed and filtered using 0.2 µm filter to remove any remaining cells in the solution. To the filtered solution, 50 mM Tris (pH = 7.5), 500 mM NaCl and 10 mM imidazole were added, and the resulting solution was directly added to Ni-NTA agarose bead (200 mL supernatant per 1 mL bead). The solution was incubated on a rotary platform overnight at 4^{o}C. On the next day, the bead was packed to a plastic polypropylene column and washed with 10X column volume of 50 mM Tris (pH = 7.5), 500 mM NaCl and 10 mM imidazole. Finally, the protein was eluted with 50 mM Tris (pH = 7.5), 500 mM NaCl and 1M imidazole. The eluted solution was concentrated using Amicon Ultra-15 centrifugal filter and buffer exchanged into 1X PBS. The concentrations of the ICAM-1s were adjusted to 1 mg/mL and stored at -80^{o}C before use.

3.4.9. Fluorescence microscopy

The microscope was a Nikon Eclipse Ti driven by the Elements software package. The microscope features an Evolve electron multiplying charge coupled device (EMCCD; Photometrics), an Intensilight epifluorescence source (Nikon), a CFI Apo 100× (numerical aperture (NA) 1.49) objective (Nikon) and a TIRF launcher with three laser lines: 488 nm (10 mW), 561 nm (50 mW), and 638 nm (20 mW). This microscope also includes the Nikon Perfect Focus System, an interferometry-based focus lock that allowed the capture of multipoint and time-lapse images without loss of focus. In all the reported experiments, we used the following Chroma filter cubes: TIRF 488, TRITC, and reflection interference contrast microscopy (RICM).

3.4.10. Preparation of DNA hairpin-based molecular tension probes on glass surfaces

No. 1.5H glass coverslips (Ibidi) were sequentially sonicated in MilliQ water (18.2 MΩ cm^{-1}) and 200 proof ethanol, 10 min each. The glasses were rinsed copiously with MilliQ water and immersed in freshly prepared piranha solution (3:1 sulfuric acid:H_2O_2) for 30 min to remove organic residues from and activate hydroxyl groups on glasses **(CAUTION: Piranha is highly reactive and explosive on contact with organics!**). The cleaned substrates were rinsed with MilliQ water in a 200 mL beaker for at least 6 times and further washed with acetone thrice. Slides were then transferred to a 200 mL beaker containing 3% APTES in acetone for 1 h, washed with ethanol thrice and thermally cured in an oven (~110^{o}C) for 15 min.

The slides were then mounted to 6-channel microfluidic cells (Sticky-Slide VI 0.4, ibidi). To each channel, ~50 µL of 10 mg/mL of NHS-PEG_4-azide (Click Chemistry Tools) in 0.1 M $NaHCO_3$ (pH = 9) was added and incubated for 1-2 h. The channels were washed with 1 mL MilliQ water thrice and the remaining water in the channels were removed by pipetting, surfaces were further dried by blowing compressed nitrogen directly into the channel. The surfaces were further blocked with 0.1% BSA in 1X PBS for 30 min and washed thrice with 1X PBS and ~50 µL of solution was kept inside the channel to prevent drying.

Subsequently, the hairpin tension probes were assembled in 1M NaCl by mixing the Cy3B labeled A21B strand (220 nM), quencher strand (220 nM) and hairpin strand (200 nM) in the ratio of 1.1: 1.1:1. The mixture was heat annealed at 95 ^oC for 5 min and cool down to 25 ^oC for 30 min. ~50 µL of the assembled probe was added to the channels (total volume = ~100 µL) and incubated overnight at room temperature. This strategy allows for covalent immobilization of the tension probes on azide-modified substrates via strain-promoted cycloaddition reaction.

On the next day, the unbound DNA probes were removed with 3X PBS washes. Then 5 µg/mL of streptavidin was added to the channels and incubated for 45 min at r.t.. The surfaces were cleaned with 3X PBS washes. Next, 5 µg/mL of ICAM-1 ligand was added to the surfaces, incubated for 45 min r.t. and washed thrice with 1X PBS. Surfaces were buffer exchanged with HBSS before imaging.

Naïve OT-1 CD8+ T cells were harvested and resuspended in HBSS. Cells were premixed with stimulatory reagents (e.g. αCD3ε, PMA, Mg^{2+}/EGTA) right before adding to the tension probe substrates and were allowed to spread at 25 ºC. Typically, cells start to engage the probes within 5 min of plating.

3.4.11. Preparation of ICAM-1 tension gauge tether (TGT) substrates

Similar to the tension probe substrate preparation, the TGT probes were assembled in 1M NaCl by mixing the top strand (biotin-labeled strand, 200 nM) and bottom strand (DBCO-labelled strand, 200 nM) in the ratio of 1:1. The mixture was heat annealed at 95 ºC for 5 min and cool down to 25 ºC for 30 min. ~50 µL of the assembled TGT was added to the channels and incubated overnight at room temperature. Biotinylated ICAM-1 was anchored on the TGT surfaces in the same way as mentioned in the previous section.

3.4.12. Preparation of multiplexed TGT substrates for co-presentation of ICAM-1 and pMHC

Multiplexed TGT substrates were prepared by sequential cycloaddition reactions. First, the ICAM-1 coated-TGT was prepared using the aforementioned protocol. After removing the unbound ICAM-1, the surfaces were incubated with 100 nM TGT strand overnight at room temperature. The unbound TGT probes were removed with 3X PBS washes. Then 5 µg/mL of streptavidin was added to the channels and incubated for 45 min at room temperature, and the channels were washed with 1X PBS thrice. Finally, 1 µg/mL of biotinylated pMHC (OVA-N4)

was added to the channels, incubated for 45 min, washed thrice with 1X PBS and buffer exchanged with 1X HBSS.

3.4.13. Preparation of small unilamellar vesicle

Small unilamellar vesicle (SUV) was prepared according to reported protocols. In brief, lipids with desired composition were mixed in a round bottom flask. The lipid mixture was dried using a rotary evaporator to remove the chloroform. The lipids were further dried under a steam of compressed N_2 and then hydrated with 2 mL of MilliQ water with a concentration of 2 mg/mL. Three cycles of freeze-thaw were performed in order to completely dissolve the lipids. The resulting lipids were then repeatedly extruded through a 80 nm polycarbonate filter until the solution became clear (~10 times) and stored at 4 ^{o}C. The extruded SUVs are stable for 4-6 weeks.

3.4.14. Supported lipid bilayer (SLB) formation

The wells in an optically transparent 96 well plates were cleaned with 200 µL of 200 proof EtOH for 5 min at room temperature and washed thrice with ddH_2O. Then the wells were further cleaned with 200 µL of 1% (w/v) KOH for 10 min at room temperature, washed thrice with ddH_2O and completely dried. The plate was treated with plasma for 3 min. After the plasma treatment, the vesicles (0.5 mg/mL) were added to cleaned 96 well plate and allowed to spread for 30 min at 50^{o}C. Unbounded vesicles were removed with three washes of 1X PBS. SLBs were subsequently blocked with 0.1% BSA in 1X PBS for 30 min and the substrates were washed thrice with 1X PBS. Then, 1 µg/mL of streptavidin was added and

incubated with the substrates for 45 min. Wells were washed thrice with 1X PBS. Subsequently, 5 µg/mL of biotinylated ligand(s) were added and incubated for 45 min. Wells were washed with 1X PBS and buffer exchange with HBSS before imaging.

3.4.15. Immunofluorescence staining

1 x 10^5 purified naïve OT-1 cells i) were mixed with 10 µg/mL of αCD3ε and immediately plated on the ICAM-1 TGT surfaces or ii) were directly plated on multiplexed tension array. They were allowed to adhere and spread for 1 h at 37°C. Cells were then fixed by 4% formaldehyde in 1X PBS for 10 min. The surfaces were gently washed thrice with 1X PBS to prevent cell detachment. Cells were then permeabilized in 0.1% Tween 20 for 5 min and washed thrice with 1X PBS. Subsequently, 2% BSA was added to the surfaces and incubated overnight at 4°C. On the next day, the surfaces were washed thrice with 1X PBS and ~50 µL of solution was kept inside the channel. 20 µL of the Alexa Fluor® 647 Mouse Anti-ZAP70 (PY319)/Syk (PY352) was added to each channel and incubated for 1 h at r.t.. Surfaces were then washed thrice with 1x PBS and buffer exchanged with 1X HBSS before imaging.

3.4.16. IL-2 ELISA

TGT surfaces used for ELISA experiment were prepared with a slightly modified protocol allowing direct immobilization of probes on regular polystyrene 96 well culture plate. First, the wells were cleaned with 200 µL of 200 proof EtOH for 5

min at room temperature and washed thrice with ddH_2O. Then the wells were further cleaned with 200 µL of 1% (w/v) KOH for 10 min at room temperature, washed thrice with ddH_2O and completely dried. The plate was treated with plasma for 3 min. After the plasma treatment, the wells were functionalized accordingly with the aforementioned procedures.

1×10^5 purified cells were resuspended in R10 media (RPMI 1640 + 10% FBS) and cultured on multiplexed tension assay for 6 h or 12 h (total volume = 100 µL). The culture supernatant was collected at the indicated time points and concentration of IL-2 was measured using the LEGEND MAX™ Mouse IL-2 ELISA Kit (Biolegend) according to the manufacturer protocol.

Appendix

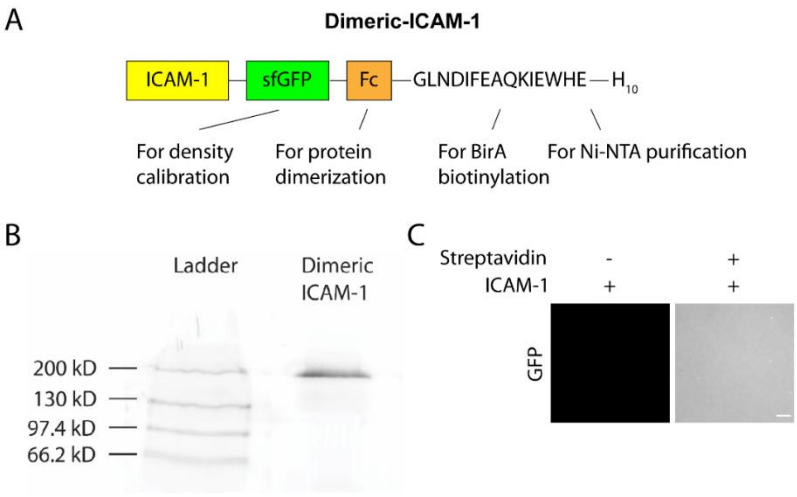

Figure A3.1. Characterizations of biotinylated ICAM-1 constructs. A) Functional map of the dimeric ICAM-1. **B)** 6% non-reducing SDS-PAGE separating gel showed estimated molecular weights of the dimeric ICAM-1. Bands were visualized with a Tycoon imager equipped with fluorescent readout with excitation for the FITC channel. **C)** Characterizing binding of the biotinylated dimeric ICAM-1 on SLB (99.9% DOPC/0.1% Biotin-Cap PE). As a control, streptavidin was withheld, and no non-specific binding were observed. Scale bar = 10 µm.

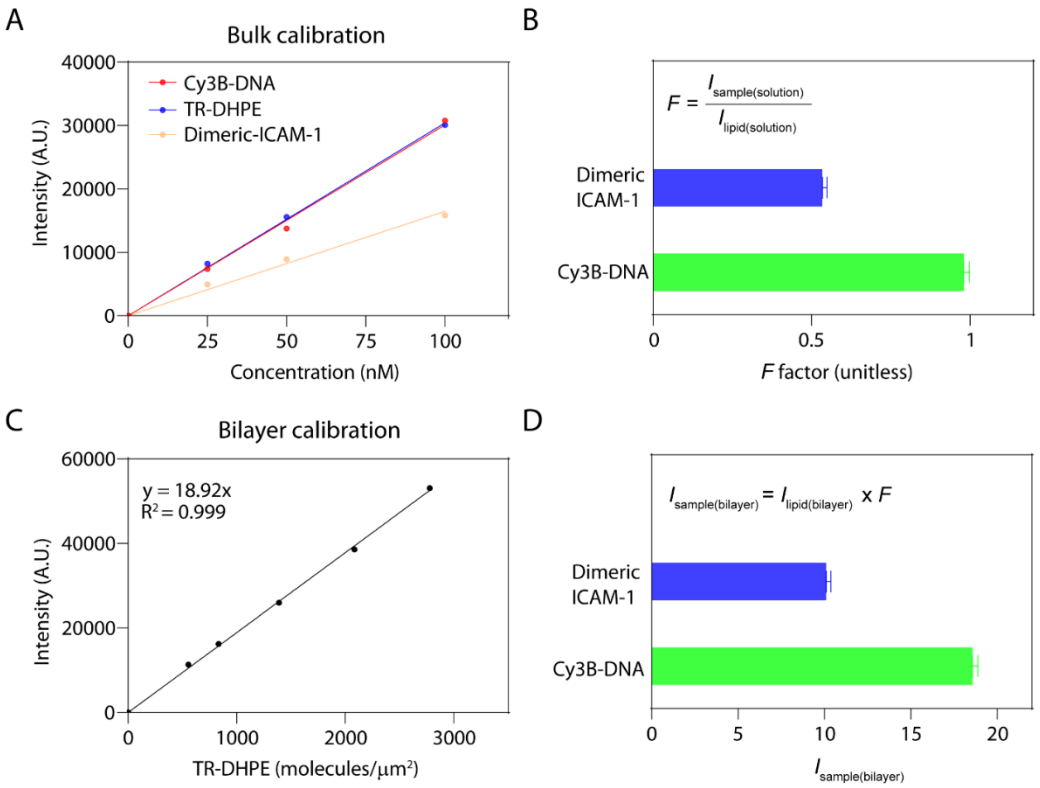

Figure A3.2. Qualitative fluorescence microscopy for density calibration of tension probe and ICAM-1. **A)** Brightness of samples and TR-DPHE liposome were measured using fluorescence microscopy. **B)** A scaling factor *F* was generated to relate the brightness of sample to the TR-DPHE by from the ratio of slopes from solution calibrations. **C)** A TR-DHPE bilayer calibration curve with known molecular densities. **D)** *F* factor was used to scale the slope of the TR bilayer calibration to estimate the relation between the sample intensity on a surface and its surface density. Density of ICAM-1s and Cy3B-tension probe used in respective experiments are summarized in **table A3.3**.

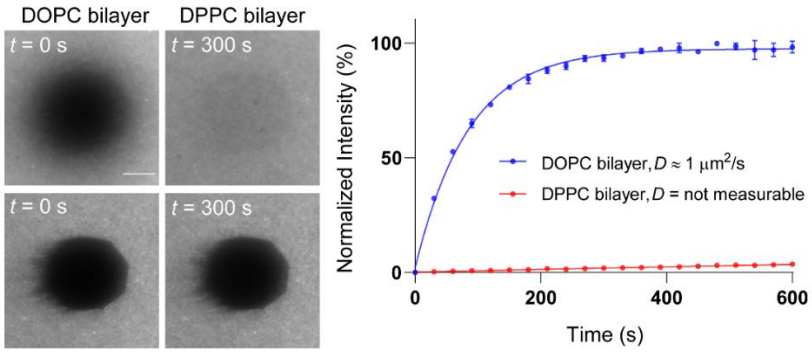

Figure A3.3. Fluorescence Recovery After Photobleaching (FRAP) experiment showing the lateral mobility of biotin-sfGFP-Fc-ICAM-1 can be manipulated using bilayers with different "fluid-to-gel" transition temperatures (Left). Representative FRAP plot shows recovery of ICAM-1 fluorescence over the course of 600 s (Right). The Lateral diffusion coefficient (D) of ICAM-1 was calculated by: $D = w^2/4t_{1/2}$, where w is the radius of the Gaussian bleaching area and $t_{1/2}$ is the time for 50% recovery obtained from the fit. Experiments were performed at 25 ^{o}C. Scale bar = 10 μm.

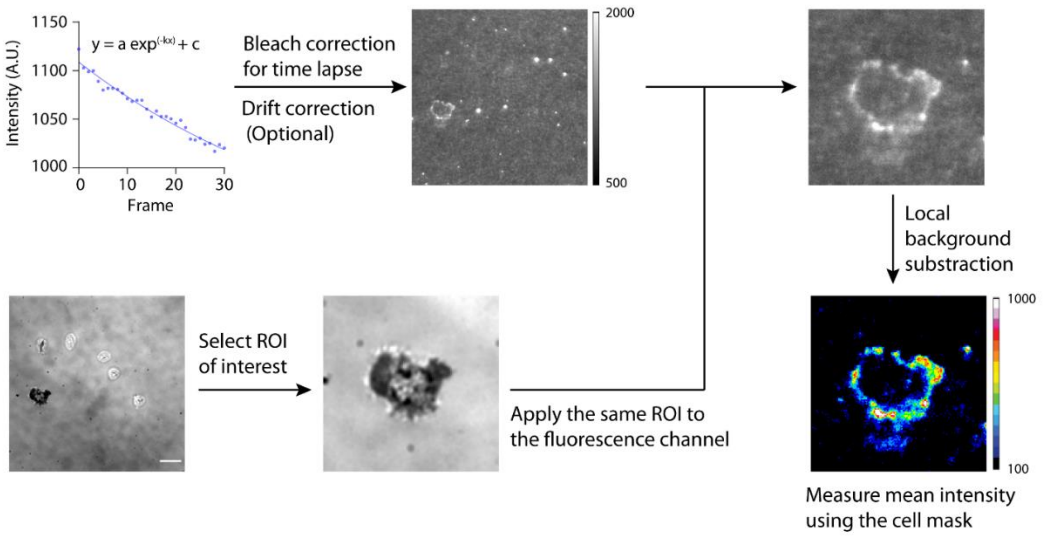

Figure A3.4. Image analysis pipeline to process the force signals. Briefly, time-lapse tension videos were subjected to photobleaching correction and drift correction. Then, a region of ROI containing at least a cell was isolated in both the tension and RICM images. From the cropped ROI, a manual local background subtraction was performed to remove signals contributed from DNA probes that were not subjected to cell pulling. The corrected image displaying tension signals were isolated using cell masks.

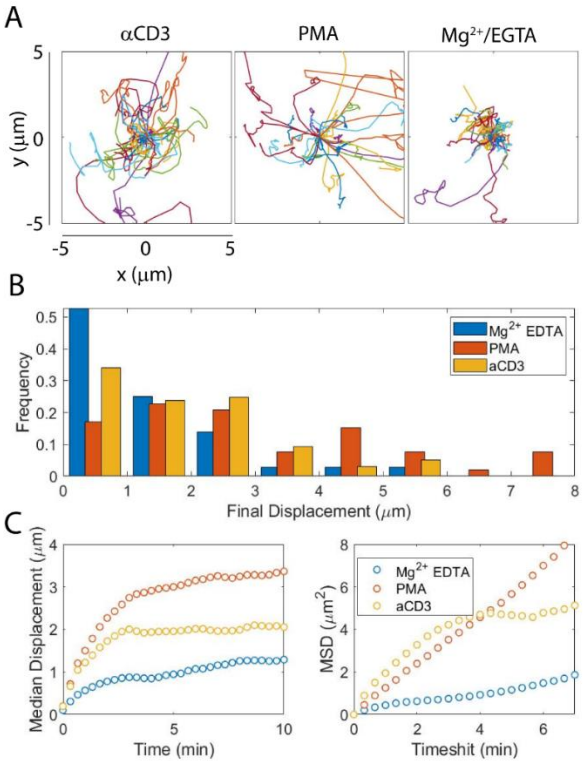

Figure A3.5. Migration analysis on *in situ* stimulated cells seeded on the ICAM-1 tension probes. A) 2D displacement plot showing ~30 tracks of cell movement in 10 min. Starting positions are normalized to the origin. **B)** Plots showing final displacements of cells from the original position. **C)** Median displacement and MSD plots showing the migration behaviour of stimulated cells. N > 50 cells from three independent experiments.

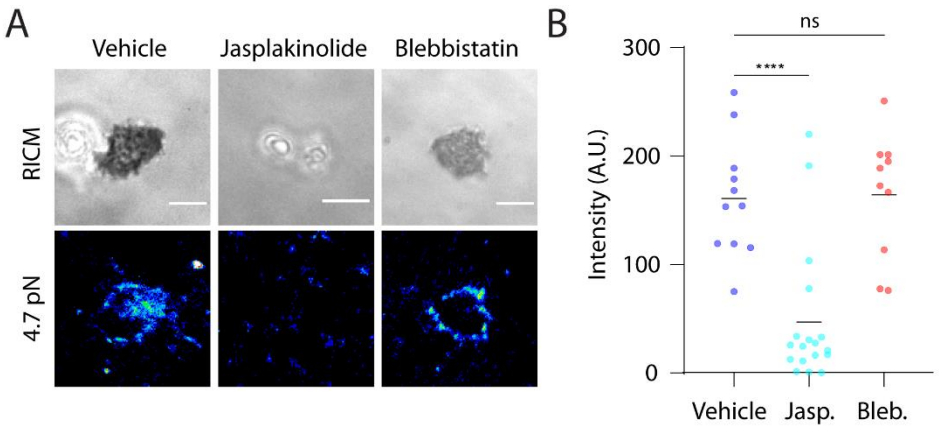

Figure A3.6. Impact of cytoskeletal drugs on LFA-1 mediated adhesion, spreading and force generation on ICAM-1 tension probe substrates. Naïve OT-1 cells were pre-treated with vehicle control (0.1% DMSO, 30 min), 0.5 µM Jasplakinolide (1 h), or 50 µM blebbistatin (30 min). Prior to cell seeding, 10 µg/mL aCD3 was infused with drug treated cells. **A)** Representative RICM and tension images of cells seeded on the ICAM-1 tension probe substrates for ~20 min. **B)** Plot showing mean tension intensity for inhibitor treated cells. ****P <0.0001.

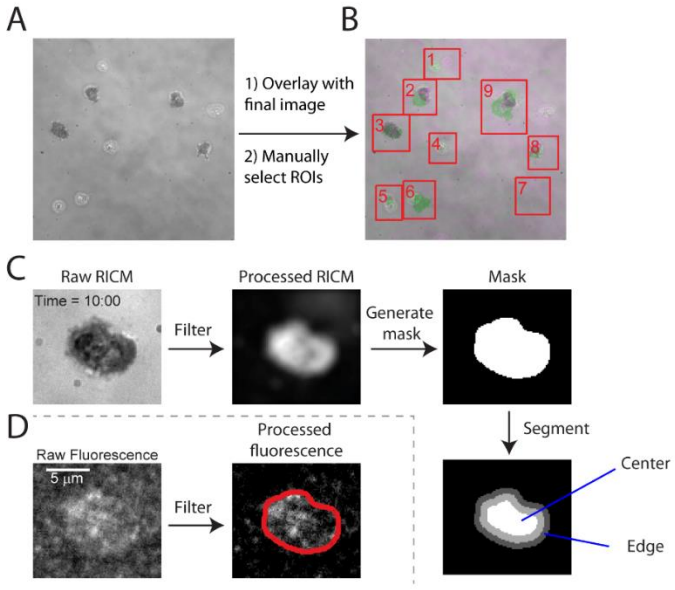

Figure A3.7. Automated image processing routine. A) The first frame of a full 512x512 reflection interference contrast microscopy (RICM) image stack is shown. **B)** The first frame is superimposed with the final frame in the image stack to enable visualization of the cell's position throughout the duration of the timelapse. The superimposed image is shown with purple denoting the initial timepoint and green denoting the final timepoint. A user then manually selects all cells in this image by drawing rectangles with MATLAB's getrect command. Each user-specified region of interest (ROI) is denoted via a numbered red rectangle. **C)** At each timepoint, the RICM image is used to generate a mask. The image is first filtered: the image is median-subtracted, and the absolute value is taken, then a 5-pixel-radius disk filter is used to smooth the image, and the image is then median-subtracted again. Next, a mask is generated by applying a threshold cutoff of 25% of the maximum value in the Processed RICM image, and the mask is then processed by removing all objects except for the largest one, closing the imaging using MATLAB's imclose command with a 3-pixel-radius disk, filling all holes with MATLAB's imfill command, and finally dilating the mask with MATLAB's imdilate command with a 3-pixel-radius disk. Finally, the mask is segmented into three regions by sorting all pixels in the mask based on distance from the mask's geometric centroid and sorting the distance-ranked pixels into three equally-sized bins. **D)** The tension image is median-subtracted, and all negative values in the image are set to zero. The filtered image is shown with mask's edge-pixels denoted in red and were divided into center and the edge regions.

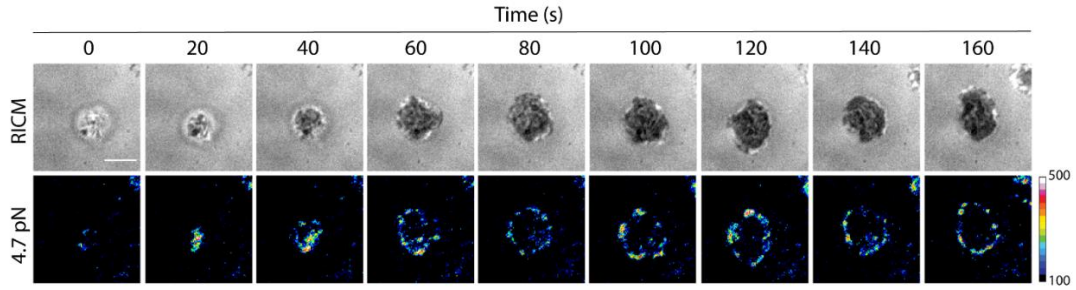

Figure A3.8. T cell generates LFA-1 forces in the presence of surface immobilized antigens. Time lapse images showing early T cell landing and LFA-1 forces on tension probe substrates co-presented with surface bound OVA N4-antigen.

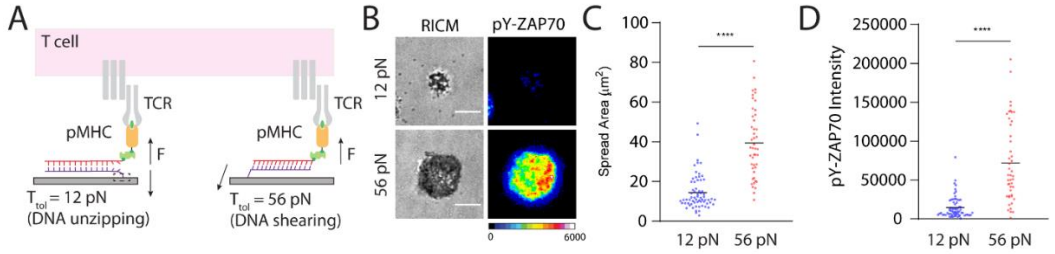

Figure A3.9. Impact of TCR mechanics on T cell signaling. A) Schematic representation of N4-TGT assay to cap maximal forces transmitted by TCR. **B)** Representative RICM and immunofluorescence images of naïve OT-1 cells seeded on 12 pN TGT or 56 pN TGT substrates for 1h. Alexa-647 phospo-ZAP70 antibody was used to stain the cells. **C)** Quantification of spread area and **D)** pY-ZAP70 intensity of cells seeded on 12 pN or 56 pN TGT substrates. N > 50 cells from three independent experiments. **** P < 0.0001.

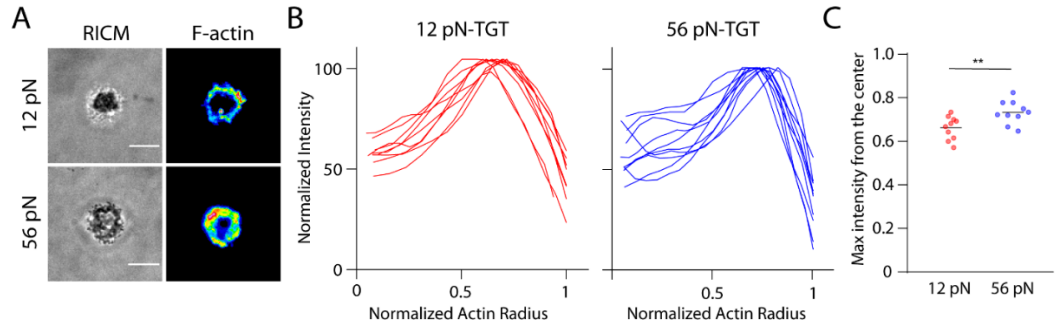

Figure A3.10. Impact of TCR mechanics on cortical actin organization. A) Representative RICM and immunofluorescence images of naïve OT-1 cells seeded on N4-12 pN TGT or 56 pN TGT substrates for 1h. Sir-actin fluorescent dye was used to stain the filamentous actin. **B)** Quantifying the radial distribution of cortical actin ring. Outline of the cells were determined using the Sir-actin signal and the cell radius was normalized to account for different cell sizes. **C)** Plot showing the position that has maximum fluorescence signal. ** P < 0.001.

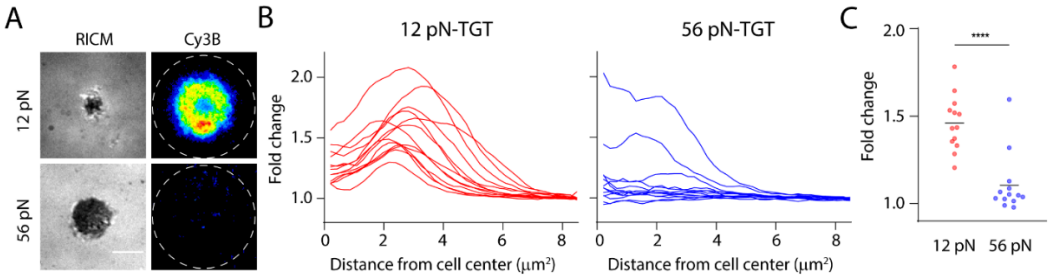

Figure A3.11. "Turn-on" TGT assay confirms TCRs transmit contractile forces >12 pN. A) Representative RICM and turn-on TGT signal of cells seeded on 12 pN TGT or 56 pN TGT substrates for ~30 min. Tension signal was normalized to background fluorescence. **B)** Single cell radial profiles of the force application history of cells seeded on 12 pN or 56 pN TGT substrates. **C)** Quantification of the fold enhancement of the fluorescence underneath the cells. **** $P < 0.0001$.

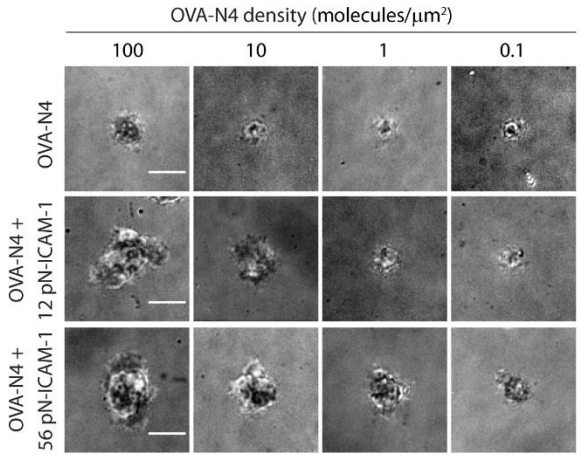

Figure A.3.12. Representative RICM images cells seeded on surfaces coated with immobilized OVA-N4, immobilized OVA-N4 and 12 pN ICAM1-TGT, or immobilized OVA-N4 and 56 pN ICAM-1-TGT. Antigen densities were varied from ~0.1 molecules/μm^2 to ~100 molecules/μm^2.

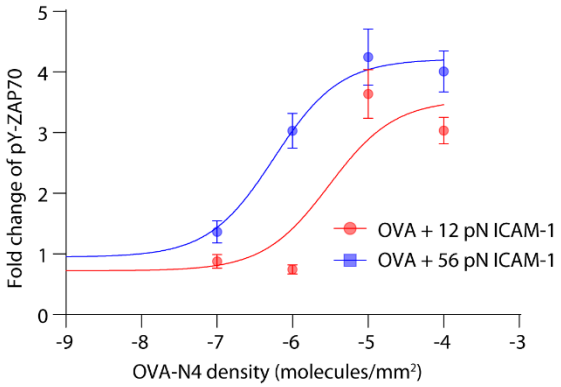

Figure A3.13. Relationship between OVA-N4 density with fixed ICAM-1 TGT density (~1000 molecules/um2) and the increase in the fluorescence enhancement of pY-ZAP70. The fits were estimated by fixing the lowest response to 1 and gave an EC_{50} (pY-ZAP70) of 3.048 x 10^{-6} molecules/nm^2 (3.05 molecules/μm^2) for cells seeded on OVA + 12 pN ICAM-1 TGT probes, and an EC_{50} (pY-ZAP70) of 5.680 x 10^{-7} molecules/nm^2 (0.57 molecules/μm^2) for cells seeded on OVA + 56 pN TGT probes.

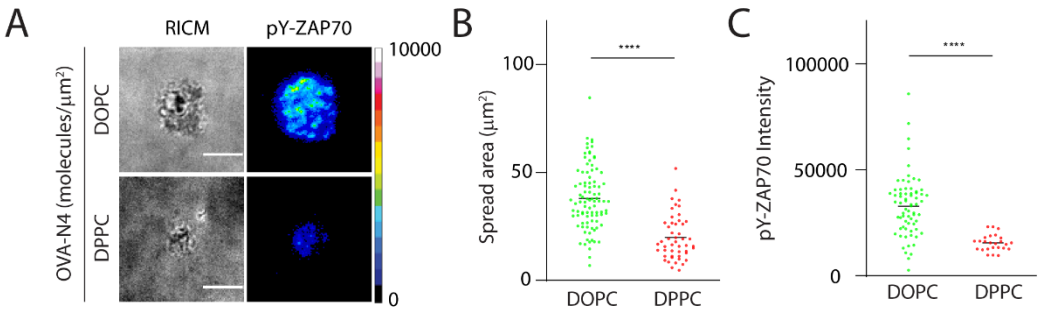

Figure A3.14. A) RICM and immunofluorescence images showing naïve OT-1 cells spreading on DOPC or DPPC bilayer presenting OVA-N4 and ICAM-1 after ~30 min of seeding. Cells were fixed and stained with Alexa 647-pY-ZAP70 antibody. **B)** Plot showing spread behavior of T cells on DOPC bilayer or DPPC bilayer presenting OVA-N4 and ICAM-1. **C)** Plot showing pY-ZAP70 intensity of cells interacting with DOPC or DPPC bilayer presenting OVA-N4 and ICAM-1. OVA density = 0.8 molecules/μm^2 and ICAM-1 density is ~800 molecules/μm^2. N>25 cells from three independent experiments. Line represents mean. ****P < 0.0001. Scale bars = 5 μm.

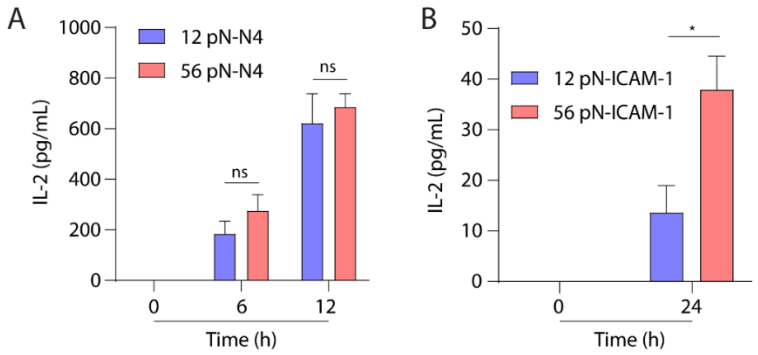

Figure A3.15. **Single component TGTs to probe the impact of receptor mechanics on T cell function**. Cytokine production ~100,000 naïve cells seeded on single ligand TGT with T_{tol} = 12 pN or 56 pN. **A)** OVA-N4-TGTs supported significant IL-2 generation but no statistically significant difference in cytokine levels in solution were detected. **B)** ICAM-1-TGTs supported little generation of IL-2 after 24 h incubation that were dependent on the T_{tol} of TGTs. Cells were co-incubated with 10 μg/mL αCD3 to trigger TCR-dependent LFA-1 activation. Experiments were run with triplicate. *$p < 0.05$.

Table A3.1. Oligonucleotide sequences used in Chapter 3.

Name	Sequence (5' to 3')
A21B	/5AmMC6/ - CGC ATC TGT GCG GTA TTT CAC TTT - /3Bio/
Quencher	/5DBCON/ - TTT GCT GGG CTA CGT GGC GCT CTT - /3BHQ_2/
Hairpin ($F_{1/2}$ = 4.7 pN)[a]	GTG AAA TAC CGC ACA GAT GCG TTT GTA TAA ATG TTT TTT TCA TTT ATA CTT TAA GAG CGC CAC GTA GCC CAG C
4.7 pN loop complement	GTA TAA ATG AAA AAA ACA TTT ATA C
DBCO-bottom strand (TGT)	/5DBCON/GT GTC GTG CCT CCG TGC TGT G
12 pN top strand (TGT)	CAC AGC ACG GAG GCA CGA CAC /3Bio/
56 pN top strand (TGT)	/5Biosg/CA CAG CAC GGA GGC ACG ACA C

[a] Underline base represents the loop forming region

Table A3.2. Annotated amino acid sequences of the soluble ICAM-1 constructs.

Dimeric ICAM-1	M A S T R A K P T L P L L L A L V T V V I P G P G D A Q V S I H P R E A F L P Q G G S V Q V N C S S S C K E D L S L G L E T Q W L K D E L E S G P N W K L F E L S E I G E D S S P L C F E N C G T V Q S S A S A T I T V Y S F P E S V E L R P L P A W Q Q V G K D L T L R C H V D G G A P R T Q L S A V L L R G E E I L S R Q P V G G H P K D P K E I T F T V L A S R G D H G A N F S C R T E L D L R P Q G L A L F S N V S E A R S L R T F D L P A T I P K L D T P D L L E V G T Q Q K L F C S L E G L F P A S E A R I Y L E L G G Q M P T Q E S T N S S D S V S A T A L V E V T E E F D R T L P L R C V L E L A D Q I L E T Q R T L T V Y N F S A P V L T L S Q L E V S E G S Q V T V K C E A H S G S K V V L L S G V E P R P P T P Q V Q F T L N A S S E D H K R S F F C S A A L E V A G K F L F K N Q T L E L H V L Y G P R L D E T D C L G N W T W Q E G S Q Q T L K C Q A W G N P S P K M T C R R K A D G A L L P I G V V K S V K Q E M N G T Y V C H A F S S H G N V T R N V Y L T V L Y H S Q N N S K G E E L F T G V V P I L V E L D G D V N G H K F S V R G E G E G D A T N G K L T L K F I C T T G K L P V P W P T L V T T L T Y G V Q C F S R Y P D H M K R H D F F K S A M P E G Y V Q E R T I S F K D D G T Y K T R A E V K F E G D T L V N R I E L K G I D F K E D G N I L G H K L E Y N F N S H N V Y I T A D K Q K N G I K A N F K I

	R H N V E D G S V Q L A D H Y Q Q N T P I G D G P V L L P D N H Y L S T Q S V L S K D P N E K R D H M V L L E F V T A A G I T H G M D E L Y K P K S C D K T H T C P P C P A P E L L G G P S V F L F P P K P K D T L M I S R T P E V T C V V V D V S H E D P E V K F N W Y V D G V E V H N A K T K P R E E Q Y N S T Y R V V S V L T V L H Q D W L N G K E Y K C K V S N K A L P A P I E K T I S K A K G Q P R E P Q V Y T L P P S R D E L T K N Q V S L T C L V K G F Y P S D I A V E W E S N G Q P E N N Y K T T P P V L D S D G S F F L Y S K L T V D K S R W Q Q G N V F S C S V M H E A L H N H Y T Q K S L S L S P G K G L N D I F E A Q K I E W H E G G G G S H H H H H H H H H H H

Orange: mouse ICAM-1 (Ig superfamily domains 1-5)
Green: superfolder GFP
Grey: Fc IgG1 heavy chain constant region
Teal: Avitag sequence for BirA biotinylation
Purple: His_{10} tag for Ni-NTA column purification

Table A3.3. Density of DNA-based tension probes/ICAM-1 on different substrates

Name	**Density (molecules/μm^2)**[a]
Dimeric ICAM-1 on DOPC bilayer	~800
Monomeric ICAM-1 on DOPC bilayer	~850
DNA-based force probe	~780
Dimeric ICAM-1 on DNA force probe	~740
Monomeric ICAM-1 on DNA force probe	~770

[a] Density of the monomeric-(dimeric-) ICAM-1or DNA-based tension probe on a substrate is estimated using the factor [$I_{\text{sample(bilayer)}}$] calculated in **Figure S2D**. Since the ICAM-1 is attached to only the upper leaflet of bilayer or the DNA probe is attached on the glass coverslip, unlike the Texas Red lipid probe which is presented on both bilayer leaflets. A factor of 2 is used to "correct the protein density (equation 1).

$$Protein\ density = \frac{2 \times\ Intensity}{I_{\text{sample(bilayer)}}}$$

where intensity is the surface fluorescent signal obtained with the same CCD camera setting as the lipid calibration experiment, and $I_{\text{sample(bilayer)}}$ is defined in **figure A3.2D**.

Chapter 4

Mechanically Induced Catalytic Amplification Reaction for Readout of Receptor-Mediated Cellular Forces

Adapted from **Ma, V.-P.-Y.**; Liu, Y.; Yehl, K.; Galior, K.; Zhang, Y.; Salaita, K. Mechanically Induced Catalytic Amplification Reaction for Readout of Receptor-Mediated Cellular Forces. *Angew. Chem. Int. Ed.*, **2016**, *128*, 5578-5582.

4.1 Introduction

Coupling between mechanical forces and chemistry at interfaces plays a profound role in biological processes ranging from biofilm formation to stem cell differentiation, and wound healing.[197-200] To understand these types of chemo-mechanical coupling processes, it is necessary to develop methods to quantify cellular forces. This is challenging because molecular forces in biochemical processes are transient and tend to range from ~1-100 pN, which is sufficient to drive conformational changes in proteins but insufficient to dissociate covalent bonds.[201] Therefore, forces in biochemical systems are difficult to detect and map.

We previously developed MTFM to image forces transmitted by cell surface receptors in living cells.[116, 202] The initial tension probes were comprised of an extendable PEG spring, flanked by a fluorophore and a spectroscopically-matched quencher.[203] pN forces extend the mean end-to-end distance of the polymer, which reduces energy transfer through an R^{-6} distance-dependent relationship. Next generation probes utilized oligonucleotides,[119-120] elastin like polypeptides,[74, 204] and engineered proteins[118], and also employed gold nanoparticle quenchers to extend energy transfer distances and enhanced sensitivity.[73, 118, 121, 205]

Nonetheless, the sensitivity of MTFM is limited due to the energy transfer-based readout and the transient nature of cellular forces. For example, current probes require high-end microscopy systems with single-photon counting EMCCDs coupled with high-numerical aperture (NA) objectives to detect changes in energy transfer efficiency. Accordingly, high-throughput screening of drugs that target mechanical processes is prohibitive. Likewise, screening the mechanical

phenotype of a library of cells is currently a challenge. Therefore, there is a pressing need to develop strategies that transduce pN forces into an easily quantifiable, and amplified chemical signal. As a corollary, catalytic amplification strategies, such as PCR and ELISA, provide the foundation of modern molecular and cellular biology, and equivalent assays for mechanics may transform the field of mechanobiology.

Enzymes that respond to specific pN mechanical inputs are widespread in Nature.[206-207] In contrast, synthetic systems that transduce defined pN forces into a catalytic output are rare (**Scheme 4.1A**). To the best of our knowledge, the only examples of synthetic catalytic reactions that are mechanically triggered are based on polymer structures that initiate mixing of an enzyme and its substrate.[208-209] These systems are sensitive to bulk forces, measured in units of kPa, rather than molecular pN events.

Herein we present the mechanically-induced catalytic amplification reaction (MCR) to amplify the signal associated with pN forces applied by cell surface receptors. The strategy depends on a blocked initiator of an enzymatic reaction that is exposed through the action of mechanical forces. Given the fidelity and sensitivity of PCR, we aimed to leverage DNA amplification as a proof-of-concept readout for MCR. The mechanically responsive element was a DNA duplex inspired by Wang and Ha's TGT assay. In their assay, an immobilized DNA duplex denatures due to cellular forces exceeding the tension tolerance, T_{tol} (defined as the minimum force needed to denature DNA when applied for 2 s). TGTs are a powerful tool in defining the mechanical forces needed for receptor activation.

As illustrated in **Scheme 4.1B**, a DNA duplex modified with a ligand is immobilized. When cells are plated on the surface, adhesion receptors engage their ligands and apply mechanical forces ($F_{receptor}$). Receptor-mediated tension exceeding the T_{tol} exposes the blocked primer for amplification. We demonstrate MCR using isothermal amplification (rather than PCR) to minimize background due to thermal denaturation of the blocked primer. For amplification, an 81-mer linear DNA template is hybridized and circularized by T4 ligase (**Table A4.1 for DNA sequences**). Next, the primer strand is replicated with isothermal rolling circle amplification (RCA).[210-211] Under optimal conditions, the RCA reaction replicates a circular template thousands of times generating a long tandem repeat of DNA (**Figure A4.1**). The repetitive amplified product is then visualized by FISH, an established technique for sensitive nucleic acid detection with high specificity.[212-214] Quantification of the product can be achieved by direct surface imaging or by release of fluorescent oligonucleotides followed by high-throughput plate reader measurements (**Scheme 4.1B)**. In principle, each mechanical rupturing event is transduced and amplified into hundreds of fluorescent oligonucleotides.

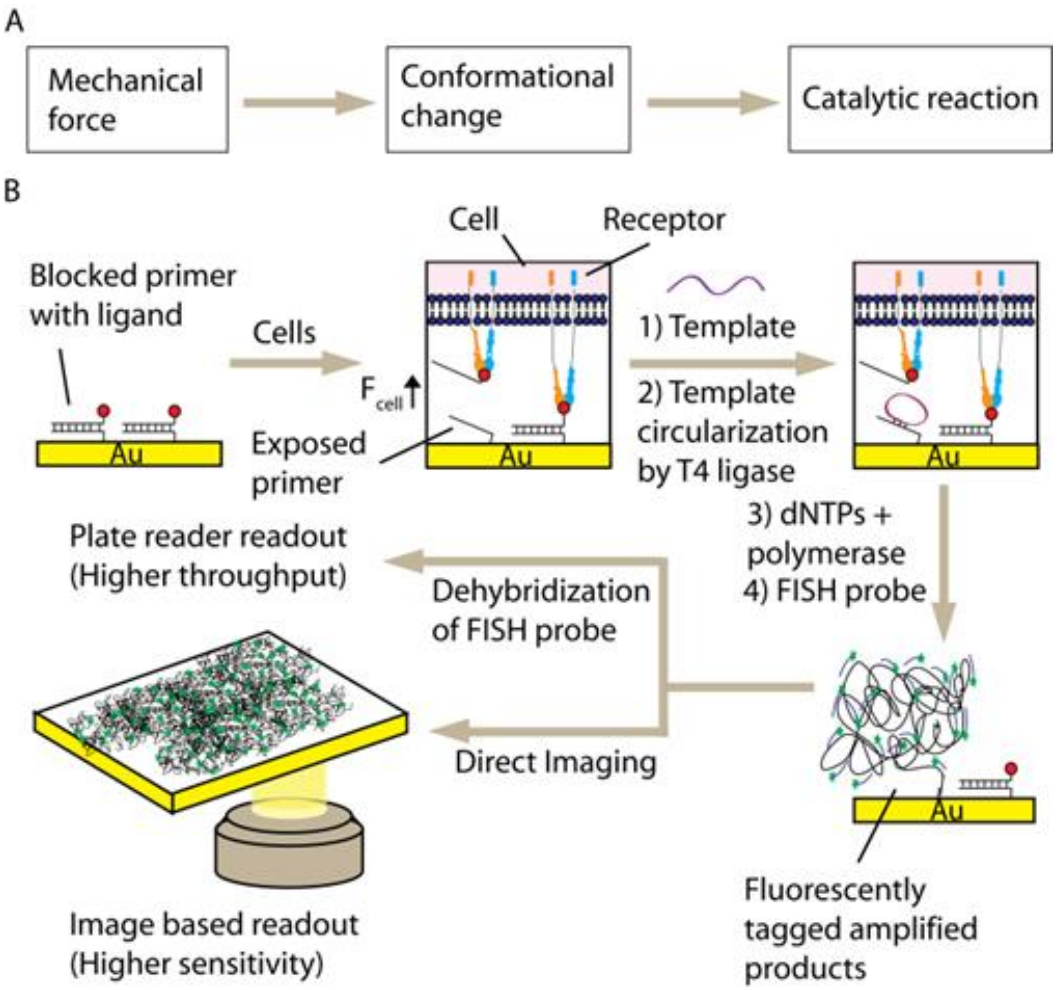

Scheme 4.1. The mechanically-induced catalytic amplification reaction (MCR).

4.2 Results and discussion

4.2.1. Characterization of the efficiency and specificity of RCA on surfaces functionalized with DNA primers

Because immobilization imposes a steric constraint to polymerases, we first quantified the efficiency and selectivity of RCA on a surface. 5' thiol modified primers with a T_{10} spacer were immobilized onto gold films,[215] and amplified as described in **Scheme 4.1B**. Surface imaging of hybridized FISH probes in the amplified samples revealed a fluorescent monolayer with a 15.7±4.9% coefficient

of variation (CV) in intensity (**Figure 4.1A**), which is likely due to heterogeneous efficiency of polymerization on the surface. In contrast, the non-amplified samples showed a 4.9±0.3% CV, demonstrating that the hybridization of complement to the primer strand is relatively more homogeneous. Importantly, the fluorescence signal in the amplified primer samples showed 102±4-fold increase compared to non-amplified samples (**Figure 4.1B**). Solution amplification shows ~1000-fold replication (**Figure A4.1**),[210] thus surface confinement inhibits polymerase activity and reduces the overall amplification efficiency. The ~ 100-fold enhancement in signal represents the maximum amplification of a mechanically triggered de-hybridization event into a chemical output.

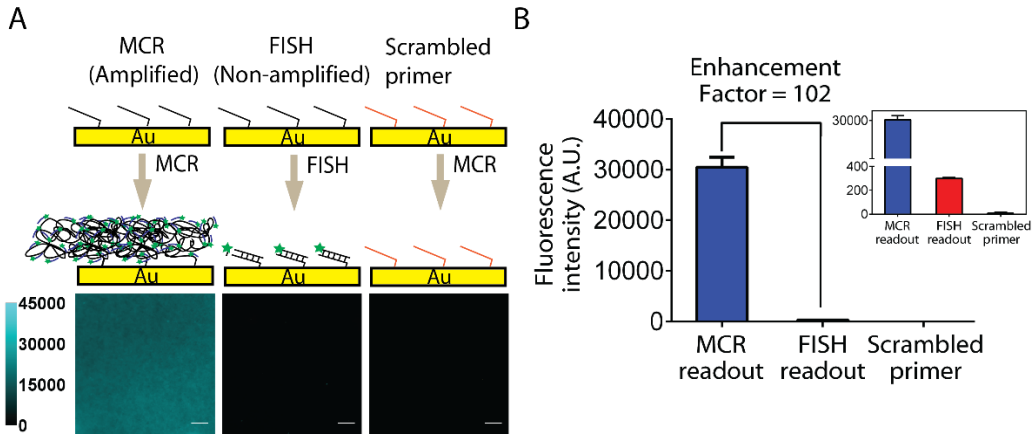

Figure 4.1. Selectivity and efficiency of surface initiated isothermal amplification. Schematic and representative epi-fluorescence images (A) and plot of mean signal (B) from positive (primer), and negative controls (non-amplified sample, and scrambled primer). Error bars represent S.E.M. obtained from three independent experiments (total 30 images). Scale bars = 10 µm.

4.2.2. "Turn-off" TGT probes report force-driven primer exposure by integrins

We next used MCR to detect forces mediated by integrins, which are a family of heterodimeric cell surface receptors that mediate cell adhesion and migration. Integrins physically bridge the cellular cytoskeleton with the

extracellular matrix, and accordingly experience pN forces. Assays that allow for screening of compounds that modulate integrin tension are of potential significance. We first quantified integrin-mediated denaturation of immobilized DNA duplexes. 5'-Cy3B, 3'-biotin labeled complement was hybridized to the primer (**Figure 4.2A**). Biotin-streptavidin binding was used to present the cyclic Arg-Gly-Asp-D-Phe-Lys (cRGDfK) peptide, a high-affinity ligand for integrin receptors. In this geometry, mechanical forces denature the duplex in an unzipping mode with a predicted T_{tol} = 12 pN. An identical primer sequence hybridized to a complement with 3'-Cy3B, 5'-biotin leads to denaturation in a shearing mode with a predicted T_{tol} = 56 pN. Note that the surface presents chemically identical probes with differing mechanical tolerance. After plating NIH/3T3 fibroblast cells on these surfaces for 1 h, we observed a loss in fluorescence that colocalized with the cell footprint as indicated by RICM (**Figure 4.2B**). Minimal loss in fluorescence was observed when the cRGDfK adhesion peptide was withheld. We quantified the decrease in Cy3B fluorescence under individual cells (**Figure 4.2C**) and found a greater fraction of the T_{tol} = 12 pN duplexes were denatured (13.7±0.9% decrease in fluorescence) compared to that of the T_{tol} = 56 pN duplex (6.5±0.45% decrease in fluorescence). The data shows differential mechanical denaturation of DNA duplexes, with a two-fold difference in DNA loss when comparing the 12 pN to 56 pN duplexes.

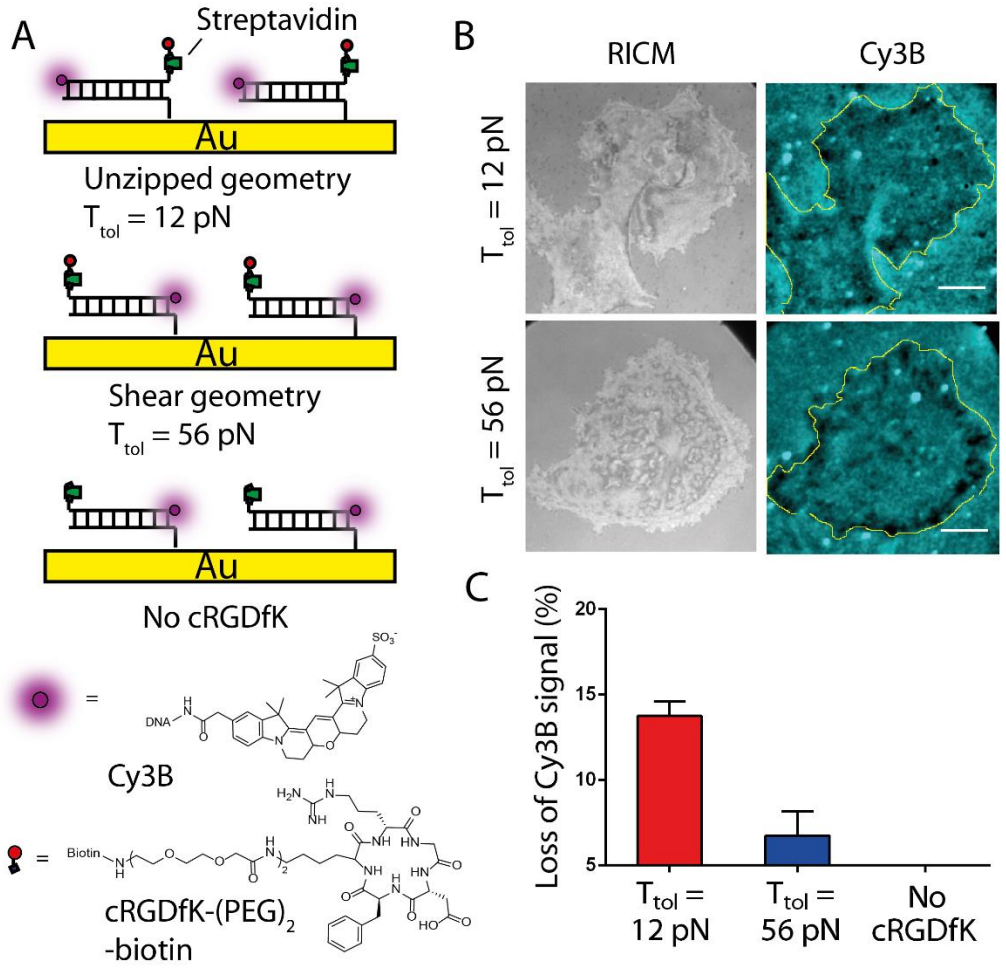

Figure 4.2. "**Turn-off" TGT probes show fibroblasts generate forces. A)** Schematic of mechanically labile duplexes used to study integrin-mediated forces. **B)** Representative RICM and fluorescence images of cells cultured on T_{tol} = 12 pN and T_{tol} = 56 pN surfaces. The negative signal observed in the Cy3B channel colocalized with cell adhesion patterns in RICM. Yellow line shows the cell edge as determined from RICM. Scale bars = 10 μm. **C)** Plot quantifying loss of Cy3B fluorescence, which indicates mechanical DNA denaturation (n = 10 cells).

4.2.3. MCR amplifies exposed primers as a result of integrin tension

To catalytically amplify exposed primers, we plated 100,000 cells to the 12 and 56 pN surfaces (surface area = 68.58 mm^2) and allowed them to spread for 1 h. This cell density corresponds to a full monolayer (680 μm^2 available per cell assuming each cell can spread ~900 μm^2). We then performed MCR and imaged

the fluorescently tagged probes by epi-fluorescence microscopy. As shown in **Figure 4.3A and B**, a significant fluorescence signal was observed on the surface. Therefore, primer amplification can readily be used to detect integrin-driven denaturation of blocked primers. Note that MCR was performed in standard conditions (20 mM Tris-OAc, 50 mM KOAc, 10 mM $Mg(OAc)_2$, 100 μg/ml BSA, pH = 7.9) as media compatible with cells (such as DMEM, PBS, and HEPES) inhibit polymerase activity which is needed for MCR (**Figure A4.2**). Therefore, cells are absent during readout likely due to the multiple washing and incubation steps in MCR buffer.

Controls using duplexes lacking cRGDfK (**Figure 4.3C**) and scrambled duplexes non-complementary to the template (**Figure 4.3D**) confirmed the specificity of MCR. In these controls, we doped the DNA surface with 10% (by incubation concentration) single stranded DNA labelled with cRGDfK to mediate cell adhesion. The cell density was nearly identical on all the tested surfaces in **Figure 4.3**, indicating that the density of cRGDfK ligands was sufficient to trigger cell adhesion prior to MCR readout (**Figure A4.3**). All controls showed low signal, ~150 fold lower than that generated by the 12 pN surface (Figure 3C and D). The background signal observed in **Figure 4.3C** is likely due to amplification of single stranded primers exposed due to spontaneous dissociation of DNA duplexes. Confirming this result, we found a ~3% loss of fluorescently labelled DNA duplexes from the surface when incubated in cell imaging media for 3 hrs at 37°C (**Figure A4.4**).

The bar graphs in **Figures 4.3E** and **F** show the results of quantifying the MCR signal using imaging-based, and plate reader-based readouts, respectively. For plate reader-based readout, the bound FISH probes were released by de-hybridization with nanopure water, and then transferred to a 96-well plate where fluorescence was quantified. Importantly, the fluorescence intensity was normalized to the maximum MCR signal obtained from a monolayer of primer (~3.5 x 10^4 primers per μm^2 (**Supplementary Note 4.1**), which is consistent with the literature precedent[216]) prepared in the same batch. The differences between image-based and plate-reader based readouts are likely due to differential levels of background and sensitivity; with the image-based readout likely more sensitive. The 12 pN duplex showed ~5-fold and 2.7-fold greater signal than that of the 56 pN duplex in **Figures 4.3E** and **3F**, respectively, consistent with the mechanically-induced dehybridization data in **Figure 4.2**.

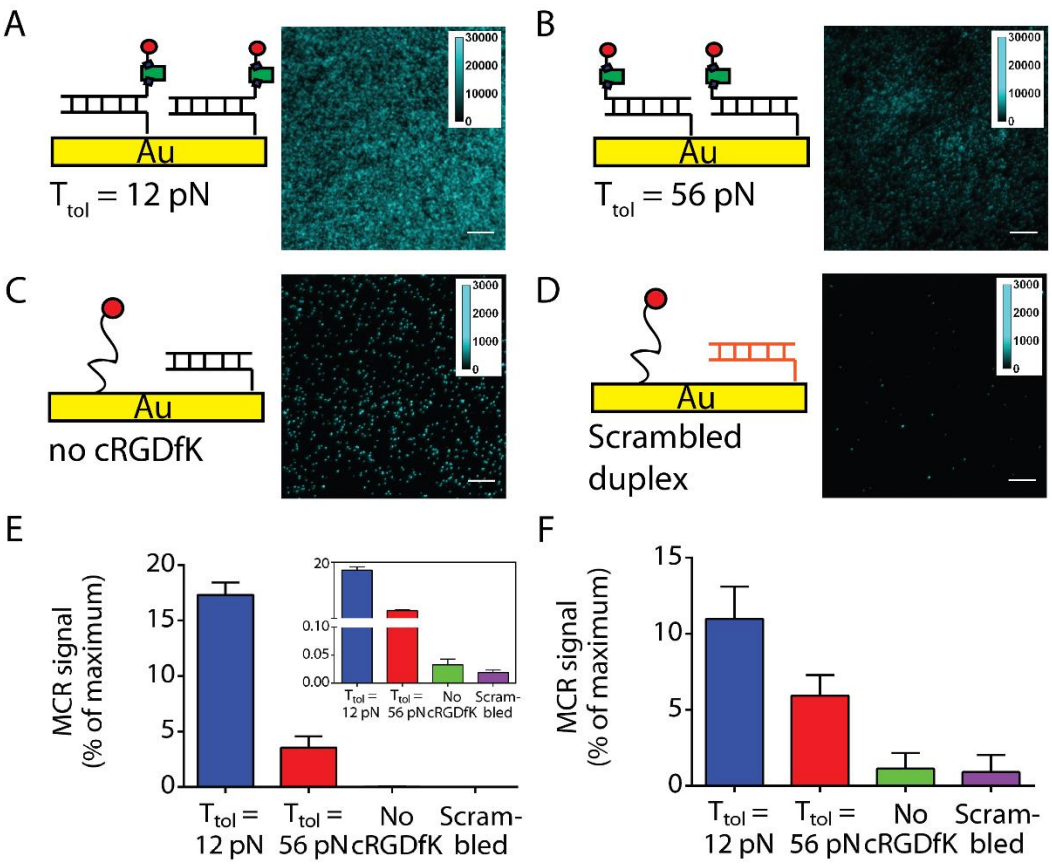

Figure 4.3. **MCR to catalytically convert integrin forces into amplified signals.** Schematic and representative fluorescence images of **A)** duplexes with T_{tol} = 12 pN, **B)** T_{tol} = 56 pN, **C)** duplexes lacking the cRGDfK peptide, and **D)** scrambled duplexes. **E)** Bar graph showing the average MCR signal from 30 different images from three independent samples. Error bars represent the S.E.M. of the results. **F)** Bar graph showing the intensity of the eluent following release of FISH probes from the surfaces and detected by a microplate reader. Error bars represent the S.E.M. of the results from three independent experiments. Scale bars = 10 μm.

4.2.4. MCR detects drug that directly impairs integrin tension

We next demonstrated the ability to conduct drug screens where we measured the effect of a drug on integrin mechanics rather than cell viability. We investigated the non-muscle myosin II inhibitor blebbistatin, which diminishes myosin contractility and thus reduces forces transmitted by focal adhesions. We pre-treated NIH/3T3 cells with a range of blebbistatin concentrations (10 nM-10

μM) for 15 min and then incubated the cells onto the surface with the 12 pN duplexes for 1 h, which was then followed by MCR readout. Brightfield imaging indicated that cells become more rounded with increasing drug dose (**Figure A4.5**). This is confirmed by *F*-actin staining which showed more disorganized and shorter actin filaments at the highest blebbistatin doses (**Figure 4.4A**). Correspondingly, the MCR signal displayed a dose-dependent relationship where the highest blebbistatin concentrations generated the lowest MCR signal (**Figure 4.4B and C**). The MCR signal is a direct readout of integrin tension, measuring the dose-dependent dissipation of actomyosin contractile forces.

4.2.5. MCR screens antibodies that impair integrin mechanics

To further highlight the utility of MCR, we measured the MCR signal on the 12 pN duplex surfaces in response to inhibiting different integrin subtypes. The two major integrin subtypes mediating adhesion of NIH/3T3 fibroblasts are $\alpha_v\beta_3$ and $\alpha_5\beta_1$ that display divergent cellular functions.[217] In surface-based imaging, anti-$\alpha_v\beta_3$ antibody treatment reduced the MCR signal by 59.6±4.1%, while anti-$\alpha_5\beta_1$ antibody treatment reduced the MCR signal by 14.6±5.6% (**Figure 4.4D, blue bars and Figure A4.6**). Incubation with both antibodies led to the greatest reduction in MCR signal (64.4±4.3%). Plate reader measurement showed a similar trend (**Figure 4.4D, red bars**). The differential MCR signal following antibody blocking is likely due to a number of factors. First, $\alpha_v\beta_3$ integrins play a more important role in mediating the adhesion of fibroblasts.[218] Second, the experiment is performed after 1 h of cell incubation, and $\alpha_v\beta_3$ integrins are thought to initiate cell adhesion.[219]

Finally, $\alpha_v\beta_3$ integrins show higher affinity toward the cRGDfK ligand (K_d ~ nM) compared to that of $\alpha_5\beta_1$.[220]

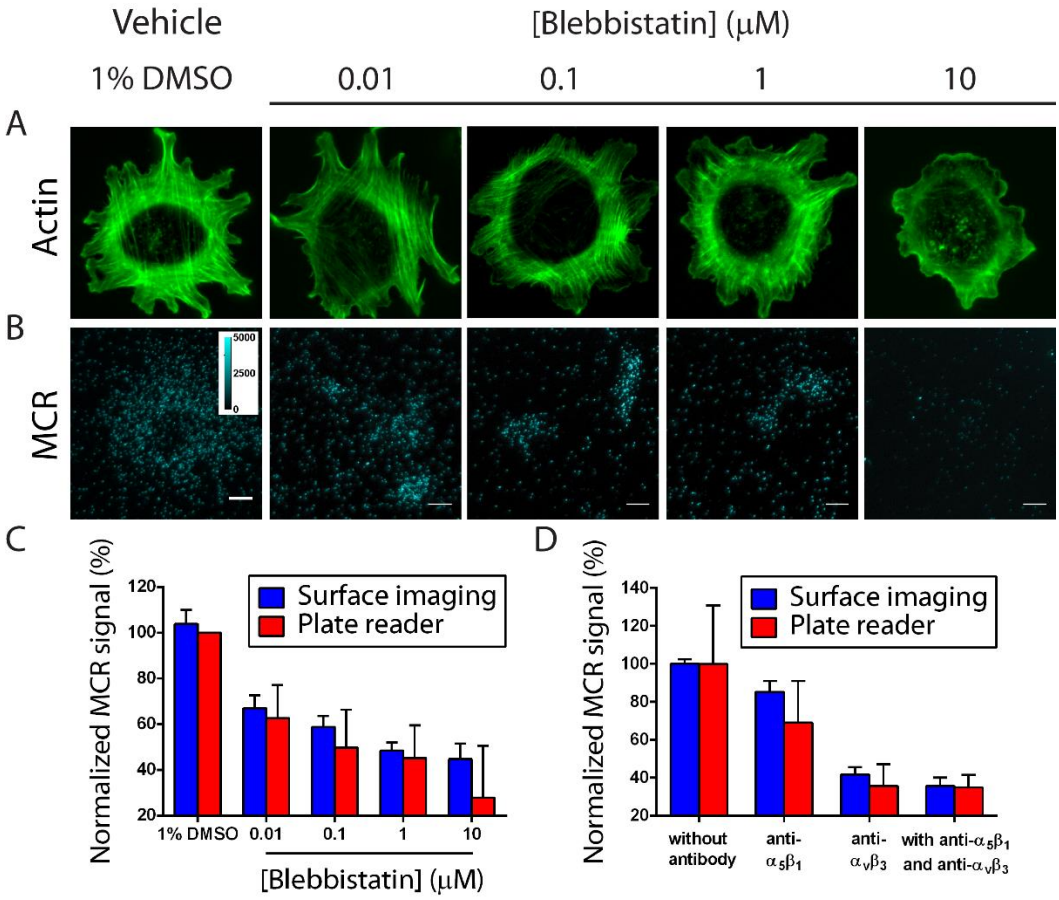

Figure 4.4. MCR screens drug/antibodies that impair integrin mechanics. Representative fluorescence images showing **A)** F-actin staining and **B)** MCR signal for NIH/3T3 cells treated with increasing concentrations of blebbistatin (0.01 -10 μM). **C)** Bar chart showing the MCR signal in response to increasing concentration of blebbistatin. **D)** Bar chart quantifying MCR signal in the presence of anti-$\alpha_5\beta_1$, anti-$\alpha_v\beta_3$ or both antibodies relative to the sample without antibodies. Error bars represent the S.E.M. from n = 30 images from 3 independent samples in surface imaging readout, and n = 3 independent samples for plate reader based readout. Scale bars = 10 μm.

4.3. Conclusion

In summary, we report herein the first catalytic amplification assay, termed MCR, for readout of cellular force. This was achieved by leveraging the surface exposed ssDNA, resulting from TGT rupture by mechanical forces generated by cell surface receptors, for enzymatic amplification. We quantitatively compared the response of this amplification assay to the FISH based technique[97] and found that it provided ~100-fold improvement in fluorescent signal in cell free conditions. We found that fibroblast cells seeded on 12 pN RGD-TGT generated ~5-fold increase in MCR signal than that of 56 pN RGD-TGT, supporting recent results that showed integrins in fibroblast cells generated a universal peak force response of ~40 pN.[90] Additionally, we demonstrated the potential use of this technique in mechano-drug screening (i.e. to identify drugs that impair cell mechanics rather than cell viability).[221] A cytoskeletal drug blebbistatin was found to dose-dependently inhibit the MCR signal with a IC_{50} of ~0.5 μM in both plate reader and microscope measurement.

It is worth to note that unlike the aforementioned DNA hairpin probes which are capable of measuring receptor forces in real time, or TGTs that detect the history of force generation, the MCR signal is highly dependent on the duration of cell incubation that alters the number of ruptured probes, as well as the amplification conditions (e.g. enzyme concentration, primer concentration, etc.). Therefore, MCR signal does not provide an absolute readout of mechanical events and requires proper calibration and controls, much like conventional ELISA and PCR assays.

4.4. Materials and methods

4.4.1. Materials

Reagents, unless otherwise specified, were purchased from Sigma Aldrich (St. Louis, MO) and used as received. All solvents were of analytical grade and purified as needed. The OliGreen stain was purchased from Molecular Probes (Eugene, OR). Cy3B NHS ester was purchased from GE Healthcare Life Sciences (Pittsburgh, PA). Azide NHS ester (Cat. no: 88902) was obtained from Thermo Scientific (Waltham, MA). Adhesion peptides *Cyclo* [Arg-Gly-Asp-d-Phe-Lys(PEG-PEG)], where PEG = 8-Amino-3,6-Dioxaoctanoic Acid and cRGDfK-biotin were purchased from Peptides International (Louisville, KY). The backfilling PEG monothiol ($HS\text{-}(CH_2)_{11}\text{-}(OCH_2CH_2)_6\text{-}OCH_3$) was purchased from nanoScience Instruments (Phoenix, AZ). Enzymes (Phi 29 polymerase and T4 ligase) are obtained from New England Biolab (Ipswich, MA). All buffer solutions were made with Nanopure water (18.2 MΩ) and passed through a 0.2 μm filtration system. All oligonucleotides were purchased from Integrated DNA Technologies (Coralville, IA) or Eurofin Genomics (Huntsville, AL) and were purified either by reverse-phase HPLC or standard desalting. Anti-integrin $\alpha_5\beta_1$ antibody (Cat no: MAB1969) was purchased from EMD Millipore (Billerica, MA). Anti-integrin $\alpha_v\beta_3$ antibody (Cat no: MAB3050) was purchased from R&D systems (Minneapolis, MN). Bottomless 6 channel slides (Sticky-Slide VI 0.4, Cat no: 80608) were obtained from ibidi (Verona, WI). mPEG-NHS (MW = 2000) and lipoic acid-PEG-NHS (MW = 3400) were purchased from Nanocs (New York, NY). Cell imaging media was prepared by dissolving 1 mix of Hanks' Balanced Salts (Cat no: H1387, Sigma

Aldrich) into 10 mM HEPES buffer, pH = 7.4.

4.4.2. Cell culture

NIH/3T3 cells were cultured in Dulbecco's modified Eagle's medium (DMEM) supplemented with charcoal-stripped calf serum serum (10%), L-glutamine (2.5 mM, Mediatech), penicillin G (100 U/mL, Mediatech) and streptomycin (100 μg/mL, Mediatech) at 37ºC in a humidified atmosphere with 5% CO_2. Cells were passaged after reaching 80% confluency and the media were changed every three days.

4.4.3. General experimental

Concentrations of purified oligonucleotide conjugates were determined by measuring their A_{260} values on a Nanodrop 2000 UV-Vis Spectrophotometer (Thermo Scientific). MALDI-TOF mass spectrometry was performed on high performance MALDI time-of-flight mass spectrometer (Voyager STR). The matrix for all experiments was prepared by freshly dissolving excess 3-hydroxypicolinic acid (3-HPA) in the matrix solvent (50% MeCN/H_2O, 1% TFA, 10% of 50 mg/mL ammonium citrate). Bulk intensities of the MCR products on 96 well plates were measured on a Bio-Tek® Synergy HT temperature-controlled plate reader.

4.4.4. Functionalization of oligonucleotides

c((RGDfK(PEG-PEG))-azide conjugate (**1**)

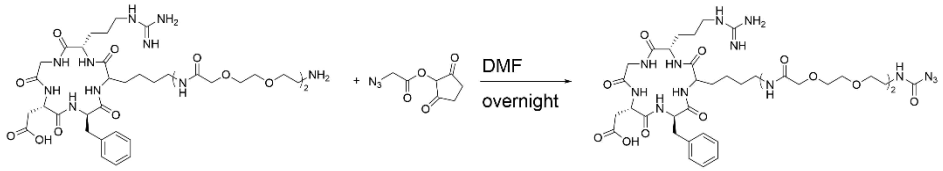

cRGDfK-$(PEG)_2$ Azide NHS ester **1**

Compound **1** was prepared following reported literature methods[77] and characterized by MALDI-TOF mass spectrometry.

T21A-alkyne (**2**)

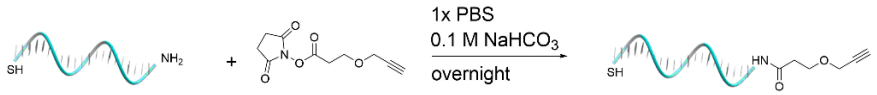

T21A Alkyne-NHS ester **2**

A mixture of T21A (10 nmol) and alkyne NHS ester (100 µg) in 0.1 M sodium bicarbonate solution (total volume = 100 µL) was allowed to react at room temperature overnight. The mixture was then separated on a P4 gel to remove salts, organic solvent and starting materials, and was further purified by reverse phase HPLC (solvent A: 0.1 M TEAA, solvent B: 100% MeCN; initial condition was 10% B with a gradient of 1%/min, flow rate: 1 mL/min). The desired product (**2**) was characterized by MALDI-TOF mass spectrometry.

T21A-cRGDfK as a supporting strand for cell adhesion (**3**)

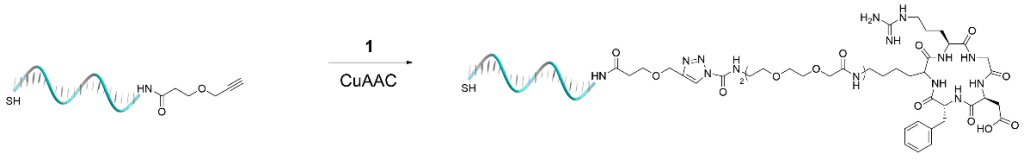

2 **3**

The cRGDfK-oligonucleotide conjugate **3** was synthesized by conventional copper

assisted [3+2] cycloaddition. A mixture of **2** (5 nmol) and compound **1** (10 nmol) in 70 µL 0.2 M TEAA solution containing 0.5 mM ascorbic acid, 0.5 mM Cu(I)-TBTA and 50% DMSO was kept at 25°C overnight. The reaction mixture was then separated on a P4 gel to remove salts, organic solvent and starting materials, and was further purified by reverse phase HPLC (solvent A: 0.1 M TEAA, solvent B: 100% MeCN; initial condition was 10% B with a gradient of 1%/min, flow rate: 1 mL/min). The desire product (**3**) was characterized by MALDI-TOF mass spectrometry.

Cy3B-FISH probe (**4**)

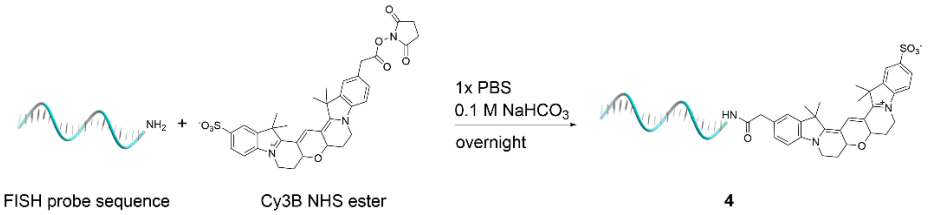

A mixture of FISH probe sequence (10 nmol) and Cy3B NHS ester (100 µg) in 0.1 M sodium bicarbonate solution (total volume = 100 µL) was allowed to react at room temperature overnight. The reaction mixture was then separated on a P4 gel to remove salts, organic solvent and starting materials, and was further purified by reverse phase HPLC (solvent A: 0.1 M TEAA, solvent B: 100% MeCN; initial condition was 10% B with a gradient of 1%/min, flow rate: 1 mL/min). The desired product (**4**) was characterized by MALDI-TOF mass spectrometry.

Primer'-Cy3B [unzipping, 12 pN (**5**)] and Primer'-Cy3B [shearing, 56 pN (**6**)]

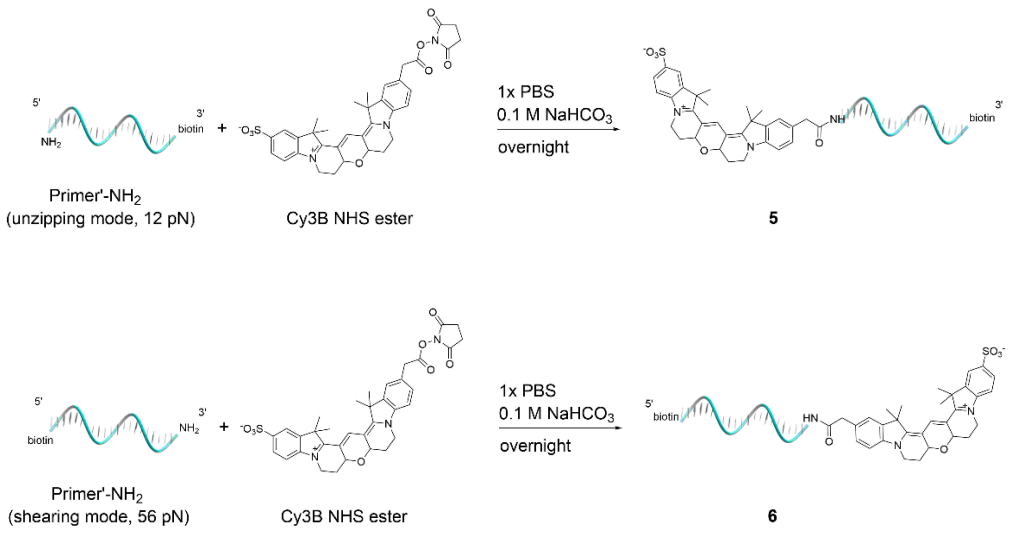

A mixture of Primer'-NH_2 (unzipping mode, 12 pN) or Primer'-NH_2 (shearing mode, 56 pN) (10 nmol) and Cy3B NHS ester (100 µg) in 0.1 M sodium bicarbonate solution (total volume = 100 µL) was allowed to react at room temperature overnight. The reaction mixture was then separated on a P4 gel to remove salts, organic solvent and starting materials, and was further purified by reverse phase HPLC (solvent A: 0.1 M TEAA, solvent B: 100% MeCN; initial condition was 10% B with a gradient of 1%/min, flow rate: 1 mL/min). The desired product (**5** or **6**) was characterized by MALDI-TOF mass spectrometry.

4.4.5. Solution-based RCA

RCA in solution was performed following an established protocol with slight modifications. Briefly, 1 pmol of the circular template and the tether strand were mixed in 1x Phi29 DNA polymerase reaction buffer containing 250 µM dNTPs and 1U/mL Phi29 polymerase. The reaction was allowed to react at 37 ºC from 0–90 min. The amplification products were separated by 0.5% agarose gel

electrophoresis or 10% polyacrylamide gel electrophoresis (PAGE), stained with SYBR gold and visualized using Gel Doc™ EZ System (Bio-rad).

4.4.6. Fabrication of gold thin films for DNA anchoring

75 x 25 mm glass slides (Cat. no: 10812, ibidi, Verona, WI) were sonicated in a 1:1 mixture of nanopure water and isopropanol for 30 min and allowed to dry at ambient conditions. Metal deposition was performed by thermal evaporation using an in-house thermal evaporation chamber (Department of Physics, Emory University) with a quartz crystal microbalance (QCM) thickness monitor. Thermal evaporation was conducted at 5 x 10^{-7} Pa. A thin 1.5 nm chromium adhesion layer was evaporated on the glass slide to promote gold adhesion. Subsequently, a 4 nm gold layer was deposited on the chromium coated glass slide. The system was allowed to cool to room temperature before removing the gold slides from the chamber to prevent carbon contamination. The thin gold films were stored in sealed petri dishes and cleaned with absolute ethanol before use.

4.4.7. Preparation of oligonucleotide modified gold film

Duplex-modified gold films (**Scheme A4.1**): 6.67 μM of primer and primer' (**Table A4.1**) were hybridized in 1X PBS by annealing to 95ºC for 5 min and the mixture was allowed to cool to room temperature. A 6-channel μ-Slide (ibidi, Verona, WI) was mounted on the thin gold film to create 6-well flow chambers with a channel volume of ~40 μL. The hybridized duplexes were dissolved in 1 M sodium chloride solution (Final concentration of duplexes = 1 μM) and were allowed to incubate on

a thin gold film overnight at 4°C with 10 μM of HS-$(CH_2)_{11}$-$(OCH_2CH_2)_6$-OCH_3 passivating polyethylene glycol. Excess DNA and PEG were removed with three washes of 0.1X SSC (1.5 mM sodium citrate, 15 mM NaCl, pH = 7.0). Afterwards, 10 μg/mL of streptavidin was added and incubated with the surfaces for 45 min. The surfaces were then washed with 0.1X SSC and subsequently 10 μg/mL of cRGDfK-biotin ligand was added and allowed to bind to the streptavidin modified duplexes for 45 min. Unbound ligand was washed away with 0.1X SSC and the surfaces were used within the same day of preparation.

ssDNA-modified gold films: 1 μM of primer was dissolved in 1 M sodium chloride solution and allowed to incubate on a thin gold film overnight at 4°C with 10 μM of HS-$(CH_2)_{11}$-$(OCH_2CH_2)_6$-OCH_3 passivating polyethylene glycol. Excess DNA and PEG were removed with three washes of 0.1X SSC and used within the same day.

4.4.8. Quantification of the density of surface-immobilized DNA

A monolayer of dsDNA was prepared according to the abovementioned protocol.[215] The duplex DNA was de-hybridized with three washes of Nanopure water and the eluents were collected and qualified by the Oligreen™ assay in 96 well plate format.

4.4.9. Preparation of glass surfaces labelled with cRGDfK

The surfaces were prepared according to literature precedent with slight modification (**Scheme A4.2**). In brief, 75 x 25 mm glass slides were sonicated in a

1:1 mixture of Nanopure water and isopropanol for 30 min, and etched in piranha solution (**Caution: Piranha can be explosive if mixed with organic solvent!**) for 15 min. The slides were then washed six times in Nanopure water and further washed in ethanol three times. Slides were then transferred to a beaker containing 1% APTES in ethanol for 1 h. Slides were extensively washed with ethanol and dried in an oven set to 80^{o}C. A 6 channel µ-Slide was then mounted to APTES functionalized glass slides to create 6 well flow chambers. 1 mg/mL biotin-NHS solution dissolved in ethanol was then introduced and allowed to incubate with the surface overnight. Surfaces were then washed extensively with Nanopure water and 1X PBS. 10 µg/mL of streptavidin was added to the chambers and incubated for 45 min. Excess streptavidin was washed out with 1X PBS. Then 10 µg/mL of biotin-cRGDfK ligand was added and incubated for 45 min. Surfaces were washed with 1X PBS and used within the same day.

4.4.10. Preparation of gold nanoparticles decorated with dsDNA

In brief, 75 x 25 mm glass slides were sonicated in a 1:1 mixture of Nanopure water and isopropanol for 30 min, and etched in piranha solution for 15 min. The slides were then washed six times in Nanopure water and further washed in ethanol three times. Slides were then transferred to a beaker containing 1% APTES in ethanol for 1 h. Subsequently, slides were extensively washed with ethanol and dried in an oven set to 80^{o}C. A 6 channel µ-Slide was then mounted to APTES functionalized glass slides to create 6 well flow chambers. Then 5% mPEG-NHS and 0.5% lipoic acid-NHS (w/v) in 0.1 M $NaHCO_3$ were added and incubated for 4 h. Surfaces were

washed extensively with Nanopure water and then 5 nM AuNP solution was introduced and incubated for 10 min. Surfaces were washed extensively with Nanopure water and then dried with nitrogen. The hybridized duplexes were dissolved in 1 M sodium chloride solution and were allowed to incubate overnight at 4°C with 10 μM of HS-$(CH_2)_{11}$-$(OCH_2CH_2)_6$-OCH_3 passivating polyethylene glycol. Excess DNA and PEG were removed with three washes of 0.1X SSC. Afterwards, 10 μg/mL of streptavidin was added and incubated for 45 min. The surfaces were then washed with 0.1X SSC and subsequently 10 μM of cRGDfK-biotin ligand was added and allowed to bind to the streptavidin modified duplexes for 45 min. Unbound ligand was washed away with 0.1X SSC and the surfaces were used within the same day of preparation.

4.4.11. Mechanically-induced catalytic amplification reaction (MCR)

Cells were incubated with the cRGDfK-labelled duplex surfaces in DMEM for 1 h to promote cell adhesion. Surfaces were then washed with 0.1X SSC. Subsequently, surfaces were incubated in 1X CutSmart® buffer (20 mM Tris-acetate, 10 mM $Mg(OAc)_2$, 50 mM KOAc, 100 μg/mL BSA, pH 7.9) with 100 nM circular template and 1U/μL T4 ligase at 37°C for 2 h to ensure complete ligation. Then, 250 μM dNTPs and 0.1U/μL Phi 29 polymerase were added to the solutions and mixed well. The surfaces were incubated at 37°C for 90 min to allow for rolling circle amplification. The chambers were washed with 0.1X TNT/0.1% SDS (15 mM NaCl, 1 mM Tris-HCl, 0.005% Tween-20, 0.1% SDS, pH = 8.0) and dried. Finally, the surface was incubated with 100 nM Cy3B-FISH probe in hybridization buffer (0.5

M NaCl, 20 mM Tris-HCl, 20 mM EDTA, and 0.01% Tween, pH = 7.4) at 37ºC for 30 min, rinsed with three washes of 0.1X TNT/0.1% SDS and subjected to fluorescence imaging. The amplification protocol was adapted from literature protocols with slight modifications.

4.4.12. Dose-dependent inhibition of integrin mediated tension quantified by MCR

Serial dilutions of blebbistatin (10 µM to 10 nM) were added to 50 µL DMEM containing ~100,000 cells/mL, respectively, and the drug treated cells were incubated in 1.5 mL Eppendorf tube for 15min. The drug treated cells were added to the duplex coated (T_{tol} = 12 pN) thin gold film assembled with a flow chamber and incubated at 37ºC for 1 h. Surfaces were then washed with 0.1X SSC and MCR was performed following the previously described procedures.

4.4.13. F-actin staining

F-actin staining of cells incubated with different concentrations of blebbistatin (10 µM to 10 nM) was performed to confirm cell response to the drug. In brief, cells were treated with various concentrations of blebbistatin as described above. Drug treated cells were then seeded on the cRGDfK-modified glass surfaces (**See Scheme A4.2 for preparation**) and incubated at 37ºC for 1h. Surfaces were then washed with 1X PBS and the cells were fixed with 4% PFA in 1X PBS at room temperature for 10 min. Cells were then permeabilized with 0.1% Triton X-100 in 1X PBS for 4 min. *F*-actin staining by Alexa-647 phalloidin (A22287, Thermo Scientific) was performed according to manufacturer's protocol.

4.4.14. Antibody blocking assay

NIH/3T3 cells were co-incubated with 10 μg/mL of monoclonal antibodies selective for integrin $\alpha_5\beta_1$ (anti-$\alpha_5\beta_1$ antibody, Millipore) or $\alpha_v\beta_3$ (anti-$\alpha_v\beta_3$ antibody, R&D systems) on gold surfaces fabricated with cRGDfK-labelled duplexes (T_{tol} = 12 pN) for 1 h. Surfaces were then washed with 0.1X SSC. MCR was performed following the previously described procedures. Note that these experiments were performed on DNA duplex immobilized onto gold nanoparticles rather than gold films. This required a slightly different protocol (**See Scheme A4.3 for preparation**). We found that immobilizing DNA duplexes on gold nanoparticles afforded improved signal by increasing the optical transparency of the substrate.

4.4.15. Image acquisition and analysis

Images were acquired using a Nikon Eclipse Ti epifluorescence microscope equipped with an Intensilight epifluorescence source, a EMCCD camera (Photometrics) a CFI Apo x100 objective (Nikon, numerical aperture = 1.49), a TIRF launcher with three laser lines: 488 nm (10 mW), 561 nm (50 mW), and 638 nm (20 mW). We used the following Chroma filter cubes for the reported experiments: RICM, TRITC and TIRF 561.

The images were processed using Fiji, an open source imaging package based on imageJ (1.50a). The background of all fluorescence images was manually subtracted by using the following commands: Process → Math → Subtract. For images shown in **Figure 2**, images are background subtracted, and then bandpass filtered by using the following commands: Process → FFT → bandpass filter.

4.6. Appendix

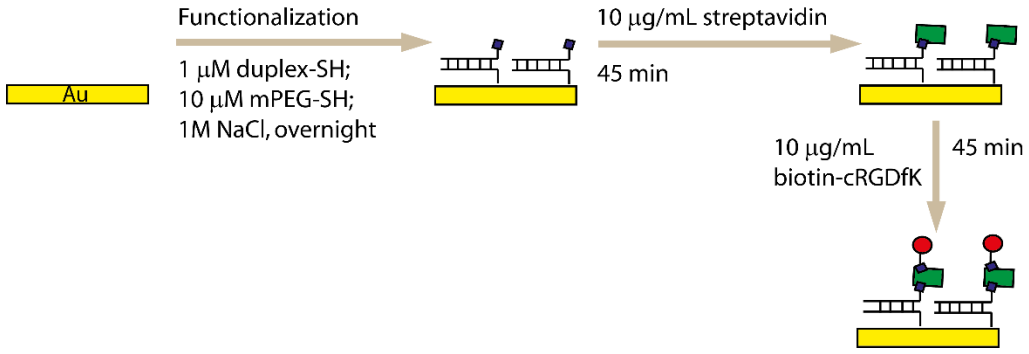

Scheme A4.1. Fabrication of thin gold film decorated with mechanically sensitive duplexes.

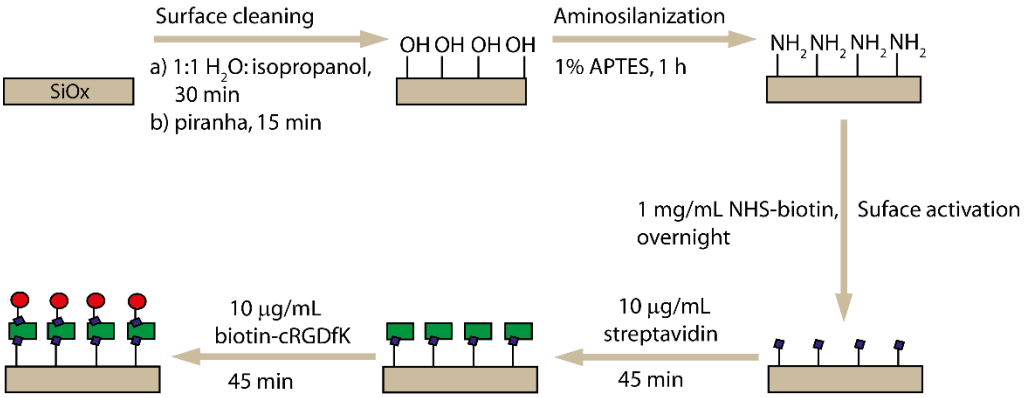

Scheme A4.2. Fabrication of glass surface labelled with cRGDfK

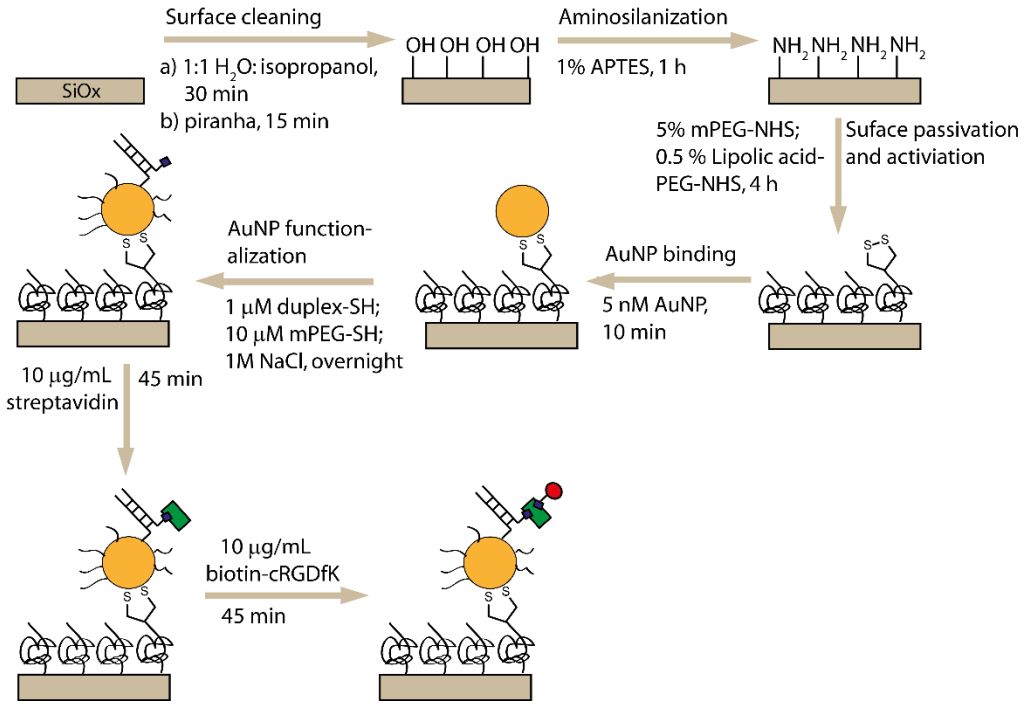

Scheme A4.3. Fabrication of AuNP surface decorated with mechanically sensitive duplexes.

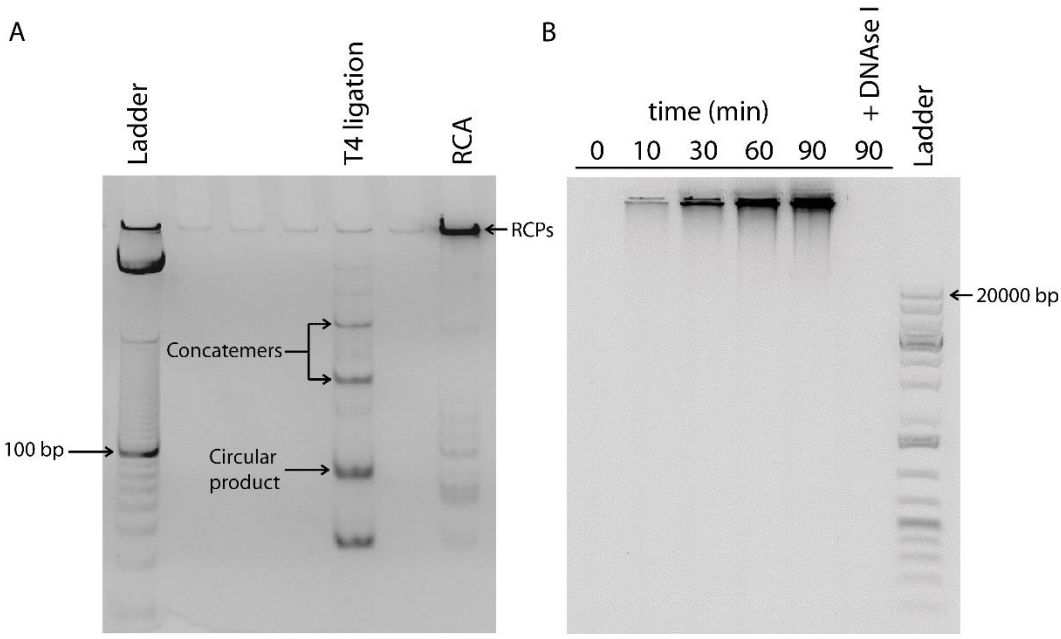

Figure A4.1. Validation of rolling circle amplification (RCA) in solution. A) 10% polyacrylamide gel showing the formation of circularized template by T4 ligation and RCA products. The product of the RCA reaction appeared as a dark band at the top of the gel. Reaction time for T4 ligation was 2 h and that for RCA was 90 min. B) 0.5% agarose gel showing the time course (0-90 min) of DNA polymerization by RCA. Treatment with DNAse I degrades the RCA product.

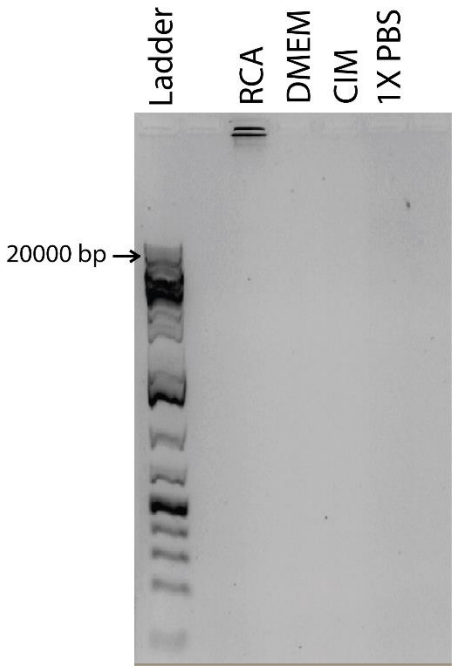

Figure A4.2. Testing RCA reaction in common biological buffers. The efficiency of RCA in three common biological buffers, including Dulbecco's Modified Eagle Medium (DMEM), cell imaging media (CIM) and 1X phosphate buffered saline (1X PBS). The RCA reaction failed to produce detectable product as indicated by the absence of high molecular weight species.

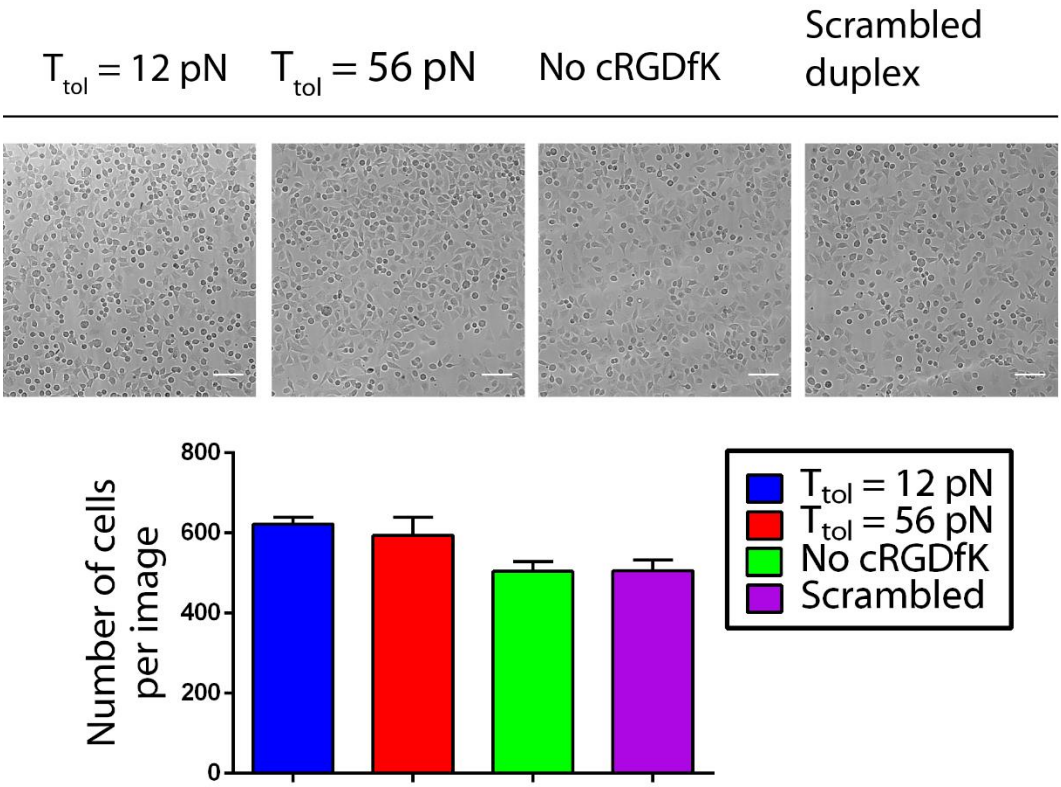

Figure A4.3. Cell adhesion on RGD-TGT functionalized gold films. Representative 10x brightfield (BF) images showing cell adhesion on different DNA constructs as shown in **Figure 4.3A–D**. Bar chart showing average cell count per image. Error bar represents the standard deviations of the results (*n* = 5 different regions). Scale bars = 100 μm.

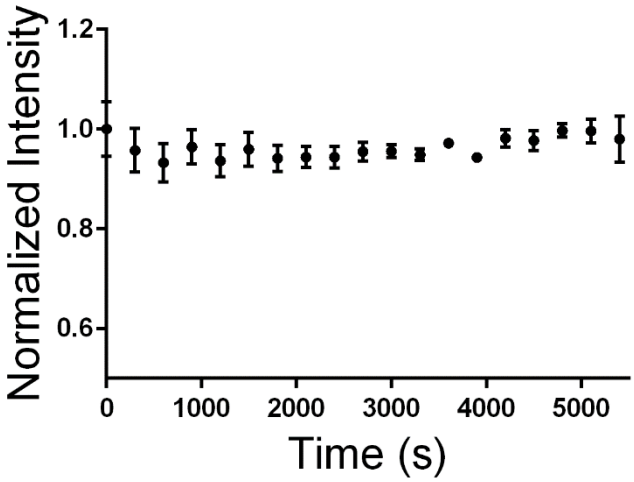

Figure A4.4. DNA dehybridization is minimal without cellular forces. Representative time course plotting DNA loss from surface functionalized with fluorescently labelled DNA duplexes. Sample was held at 37ºC in cell imaging media for 3 hrs. Error bar represents the standard deviation of the results (n = 3 different regions across the channel).

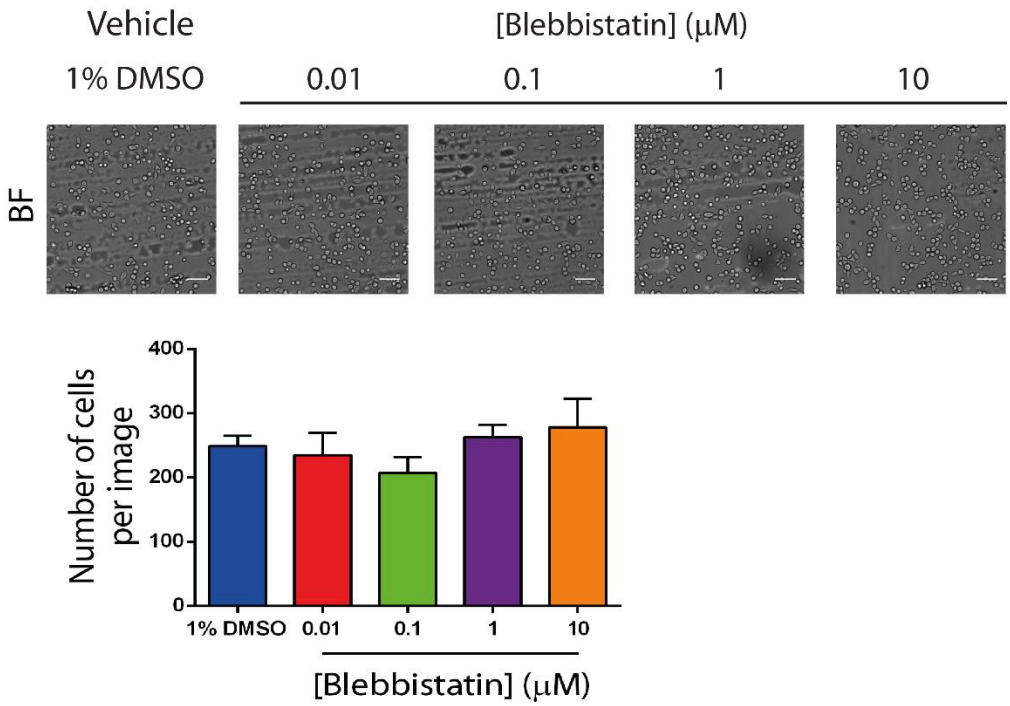

Figure A4.5. Density of drug treated cells on RGD-TGT functionalized gold films. Representative 10x brightfield (BF) images showing the density of cells treated with different concentrations of blebbistatin. Bar chart showing average cell count per image on the surface. Error bar represents the standard deviation of the results (*n* = 5 different regions). Scale bars = 100 μm.

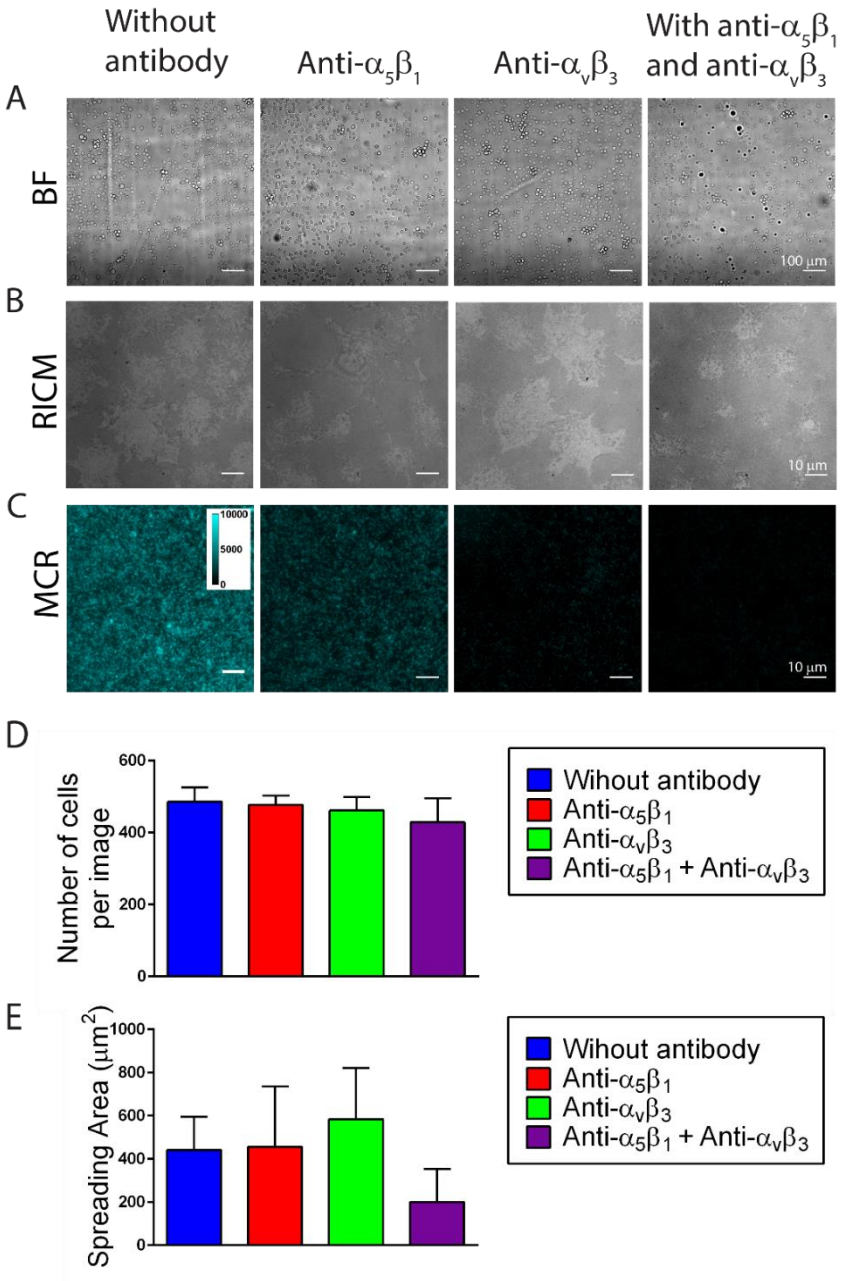

Figure A4.6. MCR signal generated by antibody-treated cells quantified by epi-fluorescence microscopy. A) Representative BF images of 3T3 fibroblasts cultured onto 12 pN DNA surfaces for 1 h and treated with different anti-integrin antibodies. Note that cell densities are similar in all four groups. **B)** Representative RICM images showing the spreading of individual cells. **C)** Representative fluorescence images showing the MCR signal following antibody blocking as described in figure 4D. **D)** Bar chart showing average cell count per image, as determined from BF. Error bar represents the standard deviations of the results (*n* = 5 different regions). **E)** Bar chart showing the average spreading area of the cells, as determined from RICM. Error bar represents the standard deviations of the results (*n* = 30 cells).

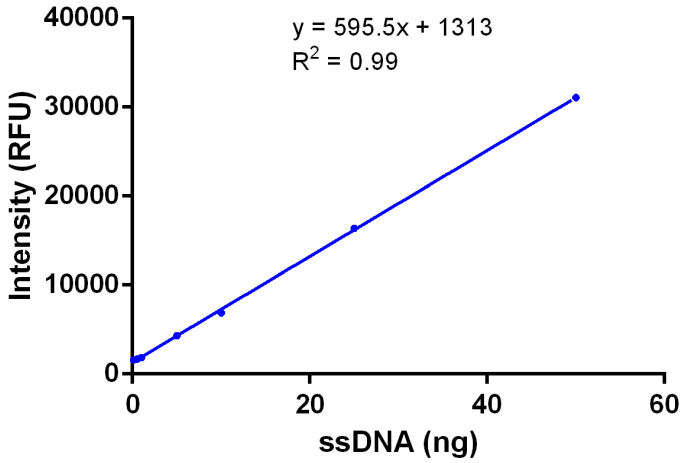

Figure A4.7. Calibration plot for determining density of DNA on gold films.

Table A4.1. Oligonucleotide sequences used in Chapter 4.

Name	**Sequence (From 5' to 3')[a]**
Circular template	/5Phos/CCGTG*TCACGGAATGGTTACTTGCACAGC* CAGCAGCCTCACGGAAT*TCACGGAATGGTTACT TGCACAGC*GTGTCGTGCCT
FISH probe sequence	/5AmMC6/TCACGGAATGGTTACTTGCACAGC
primer	/5ThiolMC6-D/T_{10}CACAGCACGGAGGCACGACAC
T21A	/5ThiolMC6-D/TTTGCTGGGCTACGTGGCGCTCTT/3AmMO/
primer' (unzipping mode, 12 pN)	GTGTCGTGCCTCCGTGCTGTG/3Bio/
primer' (shearing mode, 56 pN)	/5BiosG/GTGTCGTGCCTCCGTGCTGTG
primer'-NH_2 (unzipping, 12 pN)	/5AmMC6/GTGTCGTGCCTCCGTGCTGTG/3Bio/
primer'-NH_2 (shearing, 56 pN)	/5BiosG/GTGTCGTGCCTCCGTGCTGTG/3AmMO/

[a]The italicized and underlined bases represent FISH probe binding region and complementary region for ligation strand, respectively.

Table A4.2. MALDI-TOF MS to quantify molecular weight of synthesized oligonucleotides.

Product name	**Calcd.**		**Found**
cRGDfK-$(PEG)_2$-azide **(1)**	977.1		980.6
T21A-alkyne **(2)**	8007.5		7933.5
T21A-cRGDfK (**3)**	8988.1		8930.4
Cy3B FISH probe **(4)**	8190.7		8121.5
primer'-Cy3B (unzipping, **5**)	7708.8		7514.4
primer'-Cy3B (shearing, **6**)	7696.7		7507.1

Supplementary Note 4.1. Determining DNA density on gold films

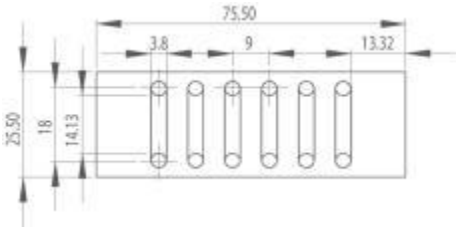

The total surface area of a flow channel can be calculated using the specification provided by the manufacturer (adapted from ibidi).

Total area of a flow channel

= Area of rectangle + Area of two half circles

$= (18 \times 3.8) + 2[\pi \left(\frac{3.8}{2}\right)^2]$

$= 68.58\ mm^2$

A calibration plot (**Figure A4.7**) was constructed by using the Oligreen assay to quantify the signal from primer' (shearing mode, 56 pN) with mass ranging from 0.1 to 50 ng. The amount of de-hybridized ssDNA was estimated by fitting the data into the calibration curve below. Based on this value, we calculated the total number of duplex DNA on the gold thin film (molecule/μm^2).

Mass of ssDNA collected	27.273 ng
No. of mol of ssDNA collected	4.12×10^{-12} mol
Total molecules of ssDNA collected	2.48×10^{12}
Total molecules of duplex on the surface (molecule/μm^2)	~35,000

Chapter 5

Conclusions and future directions

Partially adapted from **Ma, V. P.-Y.** and Salaita, K. DNA nanotechnology as an emerging tool to study mechanotransduction in living systems. *Small*, **2019**, DOI: 10.1002/smll.201900961

5.1. Conclusion and future directions

To summarize, chapter 1 gives a general overview of T cell signaling and highlights a possible role of mechanical forces in regulating T cell functions. I also provide a summary review on state-of-the-arts methods for molecular force measurements. Chapter 2 outlines a method to simultaneously map TCR forces and clustering and real time. Chapter 3 details the use of SLB technology and DNA-based force probes to question how mechanical crosstalk between TCR and LFA-1 receptors fine-tunes the overall T cell signaling and function. Chapter 4 reports the development of an approach to catalytically amplify receptor forces and its potential utility in screening drugs that impair mechanics rather than cell viability.

Overall, DNA-based force probes have emerged as a versatile biophysical toolkit for studying cellular mechanotransduction. This technique uniquely weds the strengths of SFMS (~pN force resolution) and TFM (whole cell force measurement) and has garnered significant interest from the community. While this field is still in its infancy, we will need to refine and expand the toolbox to allow easier adaptation for more diverse scientific communities. Apart from the DNA hairpins and duplexes, non-canonical DNA structures with better mechanical stabilities should enable spatiotemporal detection of surface receptors that generate high forces in real time. Non-canonical DNA structures such as G-quadruplex[222-223] and i-motif[224]were demonstrated to have relatively higher unfolding forces (~20−40 pN measured by OT) compared to DNA hairpins. Similarly, OT measurement of DNA origami nanotubes revealed that these structures could be

mechanically unfolded with forces of ~40−50 pN.[225] Because these structures also unfold cooperatively like the DNA hairpins, they can potentially be harnessed as "stiffer springs" for reversible force probe design. However, the rupture forces of naturally occurring nucleic acids are fundamentally limited because of their relatively weak hydrogen bonding interactions. To further increase the mechanical stability, and thus to push for a wider applicability in biological systems and material science, xeno nucleic acid (XNA) with improved mechanical stabilities may fulfill this challenging task. For example, peptide nucleic acid (PNA):DNA duplexes were found to have higher rupture forces (~70 pN)[226-227] compared to its DNA:DNA counterpart by dynamic force spectroscopy measurement. It is logically to conclude that other XNAs such as threose nucleic acid (TNA), locked nucleic acid (LNA) and glycol nucleic acid (GNA) would also behave similarly.

Still, directly comparing the absolute unfolding force values across different classes of DNA-based tension sensors is less meaningful when the unfolding force was determined using different methods. For example, the $F_{1/2}$ of a DNA hairpin is determined at equilibrium conditions with a constant force and this represents the minimal force to unfold a hairpin, ignoring the possibility of barriers to unfolding as the loading rate changes. More loading-rate dependent studies are needed to clearly define a relationship between loading rate and force hysteresis on the probability of DNA unfolding and refolding. However, the loading rate of receptor forces is largely unknown and likely depends on the biology of interest. Therefore,

the calibrated $F_{1/2}$ for DNA-based force probes should be considered as a calibrated value that is related to the applied force.

To date, current mechanobiology studies employing DNA-based MTFM probes have aimed to measure the forces (or peak forces) transmitted by receptors leading to receptor activation. However, an emerging concept in the field is that receptors may detect and respond to the amount of mechanical work (product of force-extension) or physical extension rather than the applied force. Alternatively, receptors may be subjected to constant extension control as part of mechanosensing circuits. Key work in this area by Hoffman and co-workers has shown that a library of genetically encoded vinculin tension sensors are extended to similar levels despite experiencing different magnitudes of forces within the FA.[228] Testing these interesting concepts of whether integrins are subjected to extension-based control or work-sensing with DNA-based probes is likely to represent a future next step for the field. These concepts intimately connect with the catch-bond model which still requires validation within functional FAs *in vivo*.

Another challenge is the chemical stability of the DNA-based force sensors within the biological environment. Cell culture often requires media that is supplemented with significant amounts (2–20%) of serum proteins (e.g. fetal bovine serum) to support normal cell metabolism. Serum is rich in nucleases that may chemically damage the DNA force probes over time. Additionally, certain cells, when activated, secrete proteases and/or nucleases that further complicate the

force measurement. For instance, we observed degradation of DNA-based force probes after incubating fibroblasts for 1-2 h,[77] which is due to mechanical probe shearing and nuclease digestion. Therefore, systematic investigations into the integrity of these probes over time is needed for each specific cellular model. Future work focused on developing chemically modified, nuclease resistant nucleic acids will ultimately solve this issue.

Developing new strategies to integrate these DNA-based force sensors with surfaces that have complex topography and composition could yield new insight into two-dimensional (2D) or three-dimensional (3D) mechanobiology. Recent work integrating DNA-based tension probes into 3D hydrogels suggests that these applications are within reach.[229] To sum, the DNA-based tension probe is rapidly transforming the study of cellular mechanotransduction. Further innovative developments will continue to push the frontiers of our capabilities as well as our fundamental understanding of molecular biophysics in developmental biology, immunology and cancer biology.

Bibliography

1. Mempel, T. R.; Henrickson, S. E.; von Andrian, U. H., T-cell priming by dendriticcells in lymph nodes occurs in three distinct phases. *Nature* **2004,** *427*, 154-159.

2. Miller, M. J.; Safrina, O.; Parker, I.; Cahalan, M. D., Imaging the Single Cell Dynamics of $CD4^+$ T Cell Activation by Dendritic Cells in Lymph Nodes. *J. Exp. Med.* **2004,** *200*, 847-856.

3. Negulescu, P. A.; Krasieva, T. B.; Khan, A.; Kerschbaum, H. H.; Cahalan, M. D., Polarity of T Cell Shape, Motility, and Sensitivity to Antigen. *Immunity* **1996,** *4*, 421-430.

4. Smith-Garvin, J. E.; Koretzky, G. A.; Jordan, M. S., T Cell Activation. *Annu. Rev. Immunol.* **2009,** *27*, 591-619.

5. Wieczorek, M.; Abualrous, E. T.; Sticht, J.; Álvaro-Benito, M.; Stolzenberg, S.; Noé, F.; Freund, C., Major Histocompatibility Complex (MHC) Class I and MHC Class II Proteins: Conformational Plasticity in Antigen Presentation. *Front. Immunol.* **2017,** *8*.

6. Zhang, N.; Bevan, Michael J., CD8⁺ T Cells: Foot Soldiers of the Immune System. *Immunity* **2011,** *35*, 161-168.

7. Wan, Y. Y.; Flavell, R. A., How Diverse—CD4 Effector T Cells and their Functions. *J. Mol. Cell Biol.* **2009,** *1*, 20-36.

8. Wucherpfennig, K. W.; Gagnon, E.; Call, M. J.; Huseby, E. S.; Call, M. E., Structural Biology of the T-cell Receptor: Insights into Receptor Assembly, Ligand Recognition, and Initiation of Signaling. *Csh Perspect Biol* **2010,** *2*.

9. Kuhns, M. S.; Badgandi, H. B., Piecing together the family portrait of TCR-CD3 complexes. *Immunol. Rev.* **2012,** *250*, 120-143.

10. Gascoigne, N. R. J., Do T cells need endogenous peptides for activation? *Nat. Rev. Immunol.* **2008,** *8*, 895.

11. Smith-Garvin, J. E.; Koretzky, G. A.; Jordan, M. S., T Cell Activation. **2009,** *27*, 591-619.

12. Rudolph, M. G.; Stanfield, R. L.; Wilson, I. A., How TCRs Bind MHCs, Peptides, and co-receptors *Annu. Rev. Immunol.* **2006,** *24*, 419-466.

13. Dorfman, J. R.; Štefanová, I.; Yasutomo, K.; Germain, R. N., CD4+ T cell survival is not directly linked to self-MHC–induced TCR signaling. *Nat. Immunol.* **2000,** *1*, 329-335.

14. Unanue, E. R., Altered Peptide Ligands Make Their Entry. *J. Immunol.* **2011,** *186*, 7-8.

15. Sloan-Lancaster, J.; Evavold, B. D.; Allen, P. M., Induction of T-cell anergy by altered T-cell-receptor ligand on live antigen-presenting cells. *Nature* **1993,** *363*, 156-159.

16. van der Merwe, P. A.; Dushek, O., Mechanisms for T cell receptor triggering. *Nat. Rev. Immunol.* **2011,** *11*, 47-55.

17. Grakoui, A.; Bromley, S. K.; Sumen, C.; Davis, M. M.; Shaw, A. S.; Allen, P. M.; Dustin, M. L., The Immunological Synapse: A Molecular Machine Controlling T Cell Activation. *Science* **1999,** *285*, 221-227.

18. Huppa, J. B.; Davis, M. M., T-cell-antigen recognition and the immunological synapse. *Nat. Rev. Immunol.* **2003,** *3*, 973-983.

19. Bromley, S. K.; Burack, W. R.; Johnson, K. G.; Somersalo, K.; Sims, T. N.; Sumen, C.; Davis, M. M.; Shaw, A. S.; Allen, P. M.; Dustin†*, M. L., The Immunological Synapse. *Annu. Rev. Immunol.* **2001,** *19*, 375-396.

20. Mossman, K. D.; Campi, G.; Groves, J. T.; Dustin, M. L., Altered TCR Signaling from Geometrically Repatterned Immunological Synapses. *Science* **2005,** *310*, 1191-1193.

21. Springer, T. A.; Dustin, M. L., Integrin inside-out signaling and the immunological synapse. *Curr. Opin. Cell Biol.* **2012,** *24*, 107-115.

22. Jun, C.-D.; Shimaoka, M.; Carman, C. V.; Takagi, J.; Springer, T. A., Dimerization and the effectiveness of ICAM-1 in mediating LFA-1-dependent adhesion. *Proc. Natl. Acad. Sci. USA* **2001,** *98*, 6830-6835.

23. Zhu, J.; Zhu, J.; Springer, T. A., Complete integrin headpiece opening in eight steps. *J. Cell Biol.* **2013,** *201*, 1053-1068.

24. Schürpf, T.; Springer, T. A., Regulation of integrin affinity on cell surfaces. *EMBO J.* **2011,** *30*, 4712-4727.

25. Abram, C. L.; Lowell, C. A., The Ins and Outs of Leukocyte Integrin Signaling. *Annu. Rev. Immunol.* **2009,** *27*, 339-362.

26. Walling, B. L.; Kim, M., LFA-1 in T Cell Migration and Differentiation. *Front. Immunol.* **2018,** *9*.

27. Perez, O. D.; Mitchell, D.; Jager, G. C.; South, S.; Murriel, C.; McBride, J.; Herzenberg, L. A.; Kinoshita, S.; Nolan, G. P., Leukocyte functional antigen 1 lowers T cell activation thresholds and signaling through cytohesin-1 and Jun-activating binding protein 1. *Nat. Immunol.* **2003,** *4*, 1083-1092.

28. Verma, N. K.; Kelleher, D., Not Just an Adhesion Molecule: LFA-1 Contact Tunes the T Lymphocyte Program. *J. Immunol.* **2017,** *199*, 1213-1221.

29. O'Connor, R. S.; Hao, X.; Shen, K.; Bashour, K.; Akimova, T.; Hancock, W. W.; Kam, L. C.; Milone, M. C., Substrate Rigidity Regulates Human T Cell Activation and Proliferation. *J. Immunol.* **2012,** *189*, 1330-1339.

30. Saitakis, M.; Dogniaux, S.; Goudot, C.; Bufi, N.; Asnacios, S.; Maurin, M.; Randriamampita, C.; Asnacios, A.; Hivroz, C., Different TCR-induced T lymphocyte responses are potentiated by stiffness with variable sensitivity. *eLife* **2017,** *6*, e23190.

31. Basu, R.; Whitlock, B. M.; Husson, J.; Le Floc'h, A.; Jin, W.; Oyler-Yaniv, A.; Dotiwala, F.; Giannone, G.; Hivroz, C.; Biais, N.; Lieberman, J.; Kam, L. C.; Huse, M., Cytotoxic T Cells Use Mechanical Force to Potentiate Target Cell Killing. *Cell* **2016,** *165*, 100-110.

32. Kim, S. T.; Takeuchi, K.; Sun, Z.-Y. J.; Touma, M.; Castro, C. E.; Fahmy, A.; Lang, M. J.; Wagner, G.; Reinherz, E. L., The αβ T Cell Receptor Is an Anisotropic Mechanosensor. *J. Biol. Chem.* **2009,** *284*, 31028-31037.

33. Das, D. K.; Feng, Y.; Mallis, R. J.; Li, X.; Keskin, D. B.; Hussey, R. E.; Brady, S. K.; Wang, J.-H.; Wagner, G.; Reinherz, E. L.; Lang, M. J., Force-dependent transition in the T-cell receptor β-subunit allosterically regulates peptide discrimination and pMHC bond lifetime. *Proc. Natl. Acad. Sci. USA* **2015,** *112*, 1517-1522.

34. Liu, B.; Chen, W.; Evavold, Brian D.; Zhu, C., Accumulation of Dynamic Catch Bonds between TCR and Agonist Peptide-MHC Triggers T Cell Signaling. *Cell* **2014,** *157*, 357-368.

35. Asally, M.; Kittisopikul, M.; Rue, P.; Du, Y.; Hu, Z.; Cagatay, T.; Robinson, A. B.; Lu, H.; Garcia-Ojalvo, J.; Suel, G. M., Localized cell death focuses mechanical forces during 3D patterning in a biofilm. *Proc. Natl. Acad. Sci. USA* **2012,** *109*, 18891-6.

36. Mammoto, T.; Ingber, D. E., Mechanical control of tissue and organ development. *Development* **2010,** *137*, 1407-20.

37. Judokusumo, E.; Tabdanov, E.; Kumari, S.; Dustin, M. L.; Kam, L. C., Mechanosensing in T lymphocyte activation. *Biophysical journal* **2012,** *102*, L5-7.

38. Brugues, A.; Anon, E.; Conte, V.; Veldhuis, J. H.; Gupta, M.; Colombelli, J.; Munoz, J. J.; Brodland, G. W.; Ladoux, B.; Trepat, X., Forces driving epithelial wound healing. *Nature physics* **2014,** *10*, 683-690.

39. McBeath, R.; Pirone, D. M.; Nelson, C. M.; Bhadriraju, K.; Chen, C. S., Cell shape, cytoskeletal tension, and RhoA regulate stem cell lineage commitment. *Dev. Cell* **2004,** *6*, 483-95.

40. Ingber, D. E., Cellular mechanotransduction: putting all the pieces together again. *FASEB J.* **2006,** *20*, 811-827.

41. Ball, P., In retrospect: On Growth and Form. *Nature* **2013,** *494*, 32.

42. Schwartz, M. A., Integrins and Extracellular Matrix in Mechanotransduction. *Csh Perspect Biol* **2010,** *2*, a005066.

43. Borghi, N.; Sorokina, M.; Shcherbakova, O. G.; Weis, W. I.; Pruitt, B. L.; Nelson, W. J.; Dunn, A. R., E-cadherin is under constitutive actomyosin-generated tension that is increased at cell–cell contacts upon externally applied stretch. *Proceedings of the National Academy of Sciences of the United States of America* **2012,** *109*, 12568-12573.

44. Liu, Y.; Blanchfield, L.; Ma, V. P.; Andargachew, R.; Galior, K.; Liu, Z.; Evavold, B.; Salaita, K., DNA-based nanoparticle tension sensors reveal that T-cell receptors transmit defined pN forces to their antigens for enhanced fidelity. *Proc. Natl. Acad. Sci. USA* **2016,** *113*, 5610-5.

45. Wan, Z.; Chen, X.; Chen, H.; Ji, Q.; Chen, Y.; Wang, J.; Cao, Y.; Wang, F.; Lou, J.; Tang, Z.; Liu, W., The activation of IgM- or isotype-switched IgG- and IgE-BCR exhibits distinct mechanical force sensitivity and threshold. *Elife* **2015,** *4*.

46. Luca, V. C.; Kim, B. C.; Ge, C.; Kakuda, S.; Wu, D.; Roein-Peikar, M.; Haltiwanger, R. S.; Zhu, C.; Ha, T.; Garcia, K. C., Notch-Jagged complex structure implicates a catch bond in tuning ligand sensitivity. *Science* **2017,** *355*, 1320-1324.

47. Salaita, K.; Nair, P. M.; Petit, R. S.; Neve, R. M.; Das, D.; Gray, J. W.; Groves, J. T., Restriction of Receptor Movement Alters Cellular Response: Physical Force Sensing by EphA2. *Science* **2010,** *327*, 1380-1385.

48. Ma, V. P.-Y.; Salaita, K., DNA Nanotechnology as an Emerging Tool to Study Mechanotransduction in Living Systems. *Small* **2019**, DOI:10.1002/smll.201900961.

49. Harris, A.; Wild, P.; Stopak, D., Silicone rubber substrata: a new wrinkle in the study of cell locomotion. *Science* **1980,** *208*, 177-179.

50. Lee, J.; Leonard, M.; Oliver, T.; Ishihara, A.; Jacobson, K., Traction forces generated by locomoting keratocytes. *J. Cell Biol.* **1994,** *127*, 1957-1964.

51. Dembo, M.; Wang, Y.-L., Stresses at the Cell-to-Substrate Interface during Locomotion of Fibroblasts. *Biophysical journal* **1999,** *76*, 2307-2316.

52. Maskarinec, S. A.; Franck, C.; Tirrell, D. A.; Ravichandran, G., Quantifying cellular traction forces in three dimensions. *Proc. Natl. Acad. Sci. USA* **2009,** *106*, 22108-22113.

53. Plotnikov, S. V.; Sabass, B.; Schwarz, U. S.; Waterman, C. M., Chapter 20 - High-Resolution Traction Force Microscopy. In *Methods in Cell Biology*, Waters, J. C.; Wittman, T., Eds. Academic Press: 2014; Vol. 123, pp 367-394.

54. Style, R. W.; Boltyanskiy, R.; German, G. K.; Hyland, C.; MacMinn, C. W.; Mertz, A. F.; Wilen, L. A.; Xu, Y.; Dufresne, E. R., Traction force microscopy in physics and biology. *Soft Matt.* **2014,** *10*, 4047-4055.

55. Tan, J. L.; Tien, J.; Pirone, D. M.; Gray, D. S.; Bhadriraju, K.; Chen, C. S., Cells lying on a bed of microneedles: An approach to isolate mechanical force. *Proc. Natl. Acad. Sci. USA* **2003,** *100*, 1484-1489.

56. Fu, J.; Wang, Y.-K.; Yang, M. T.; Desai, R. A.; Yu, X.; Liu, Z.; Chen, C. S., Mechanical regulation of cell function with geometrically modulated elastomeric substrates. *Nat. Meth.* **2010,** *7*, 733.

57. Ghassemi, S.; Meacci, G.; Liu, S.; Gondarenko, A. A.; Mathur, A.; Roca-Cusachs, P.; Sheetz, M. P.; Hone, J., Cells test substrate rigidity by local contractions on submicrometer pillars. *Proc. Natl. Acad. Sci. USA* **2012,** *109*, 5328-5333.

58. Neuman, K. C.; Nagy, A., Single-molecule force spectroscopy: optical tweezers, magnetic tweezers and atomic force microscopy. *Nat. Meth.* **2008,** *5*, 491.

59. Fuhrmann, A.; Ros, R., Single-molecule force spectroscopy: a method for quantitative analysis of ligand–receptor interactions. *Nanomedicine* **2010,** *5*, 657-666.

60. Haase, K.; Pelling, A. E., Investigating cell mechanics with atomic force microscopy. *J. Royal Soc. Interface* **2015,** *12*, 20140970.

61. Gavara, N., A beginner's guide to atomic force microscopy probing for cell mechanics. *Microsc. Res. Tech.* **2017,** *80*, 75-84.

62. Forde, N. R.; Izhaky, D.; Woodcock, G. R.; Wuite, G. J. L.; Bustamante, C., Using mechanical force to probe the mechanism of pausing and arrest during continuous elongation by Escherichia coli RNA polymerase. *Proc. Natl. Acad. Sci. USA* **2002,** *99*, 11682-11687.

63. Larson, M. H.; Greenleaf, W. J.; Landick, R.; Block, S. M., Applied Force Reveals Mechanistic and Energetic Details of Transcription Termination. *Cell* **2008,** *132*, 971-982.

64. Meyhöfer, E.; Howard, J., The force generated by a single kinesin molecule against an elastic load. *Proceedings of the National Academy of Sciences of the United States of America* **1995,** *92*, 574-578.

65. Chen, Y.; Radford, S. E.; Brockwell, D. J., Force-induced remodelling of proteins and their complexes. *Curr. Opin. Struct. Biol.* **2015,** *30*, 89-99.

66. De Gennes, P., Conformations of polymers attached to an interface. *Macromolecules* **1980,** *13*, 1069-1075.

67. Bouchiat, C.; Wang, M.; Allemand, J. F.; Strick, T.; Block, S.; Croquette, V., Estimating the persistence length of a worm-like chain molecule from force-extension measurements. *Biophysical journal* **1999,** *76*, 409-413.

68. Grashoff, C.; Hoffman, B. D.; Brenner, M. D.; Zhou, R.; Parsons, M.; Yang, M. T.; McLean, M. A.; Sligar, S. G.; Chen, C. S.; Ha, T.; Schwartz, M. A., Measuring mechanical tension across vinculin reveals regulation of focal adhesion dynamics. *Nature* **2010,** *466*, 263-266.

69. Borghi, N.; Sorokina, M.; Shcherbakova, O. G.; Weis, W. I.; Pruitt, B. L.; Nelson, W. J.; Dunn, A. R., E-cadherin is under constitutive actomyosin-generated tension that is increased at cell–cell contacts upon externally applied stretch. *Proc. Natl. Acad. Sci. USA* **2012,** *109*, 12568-12573.

70. Conway, Daniel E.; Breckenridge, Mark T.; Hinde, E.; Gratton, E.; Chen, Christopher S.; Schwartz, Martin A., Fluid Shear Stress on Endothelial Cells Modulates Mechanical Tension across VE-Cadherin and PECAM-1. *Curr. Biol.* **2013,** *23*, 1024-1030.

71. Nordenfelt, P.; Elliott, H. L.; Springer, T. A., Coordinated integrin activation by actin-dependent force during T-cell migration. *Nat. Commun.* **2016,** *7*, 13119.

72. Stabley, D. R.; Jurchenko, C.; Marshall, S. S.; Salaita, K. S., Visualizing mechanical tension across membrane receptors with a fluorescent sensor. *Nat. Meth.* **2011,** *9*, 64.

73. Liu, Y.; Yehl, K.; Narui, Y.; Salaita, K., Tension Sensing Nanoparticles for Mechano-Imaging at the Living/Nonliving Interface. *J. Am. Chem. Soc.* **2013,** *135*, 5320-5323.

74. Morimatsu, M.; Mekhdjian, A. H.; Adhikari, A. S.; Dunn, A. R., Molecular Tension Sensors Report Forces Generated by Single Integrin Molecules in Living Cells. *Nano Lett.* **2013,** *13*, 3985-3989.

75. Chang, A. C.; Mekhdjian, A. H.; Morimatsu, M.; Denisin, A. K.; Pruitt, B. L.; Dunn, A. R., Single Molecule Force Measurements in Living Cells Reveal a Minimally Tensioned Integrin State. *ACS Nano* **2016,** *10*, 10745-10752.

76. Woodside, M. T.; Behnke-Parks, W. M.; Larizadeh, K.; Travers, K.; Herschlag, D.; Block, S. M., Nanomechanical measurements of the sequence-dependent folding landscapes of single nucleic acid hairpins. *Proc. Natl. Acad. Sci. USA* **2006,** *103*, 6190-6195.

77. Zhang, Y.; Ge, C.; Zhu, C.; Salaita, K., DNA-based digital tension probes reveal integrin forces during early cell adhesion. *Nat. Commun.* **2014,** *5*, 5167.

78. Zhang, Y.; Qiu, Y.; Blanchard, A. T.; Chang, Y.; Brockman, J. M.; Ma, V. P.-Y.; Lam, W. A.; Salaita, K., Platelet integrins exhibit anisotropic mechanosensing and harness piconewton forces to mediate platelet aggregation. *Proc. Natl. Acad. Sci. USA* **2018,** *115*, 325-330.

79. Nowosad, C. R.; Spillane, K. M.; Tolar, P., Germinal center B cells recognize antigen through a specialized immune synapse architecture. *Nat. Immunol.* **2016,** *17*, 870-877.

80. Hong, J.; Ge, C.; Jothikumar, P.; Yuan, Z.; Liu, B.; Bai, K.; Li, K.; Rittase, W.; Shinzawa, M.; Zhang, Y.; Palin, A.; Love, P.; Yu, X.; Salaita, K.; Evavold, B. D.; Singer, A.; Zhu, C., A TCR mechanotransduction signaling loop induces negative selection in the thymus. *Nat. Immunol.* **2018,** *19*, 1379-1390.

81. Blakely, B. L.; Dumelin, C. E.; Trappmann, B.; McGregor, L. M.; Choi, C. K.; Anthony, P. C.; Duesterberg, V. K.; Baker, B. M.; Block, S. M.; Liu, D. R.; Chen, C. S., A DNA-based molecular probe for optically reporting cellular traction forces. *Nat. Meth.* **2014,** *11*, 1229.

82. Hatch, K.; Danilowicz, C.; Coljee, V.; Prentiss, M., Demonstration that the shear force required to separate short double-stranded DNA does not increase significantly with sequence length for sequences longer than 25 base pairs. *Phys. Rev. E* **2008,** *78*, 011920.

83. Krautbauer, R.; Rief, M.; Gaub, H. E., Unzipping DNA Oligomers. *Nano Lett.* **2003,** *3*, 493-496.

84. Zhang, J.; Yan, Y.; Samai, S.; Ginger, D. S., Dynamic Melting Properties of Photoswitch-Modified DNA: Shearing versus Unzipping. *J. Phys. Chem. B* **2016,** *120*, 10706-10713.

85. Strunz, T.; Oroszlan, K.; Schäfer, R.; Güntherodt, H.-J., Dynamic force spectroscopy of single DNA molecules. *Proc. Natl. Acad. Sci. USA* **1999,** *96*, 11277-11282.

86. Cocco, S.; Monasson, R.; Marko, J. F., Force and kinetic barriers to unzipping of the DNA double helix. *Proc. Natl. Acad. Sci. USA* **2001,** *98*, 8608-8613.

87. de Gennes, P.-G., Maximum pull out force on DNA hybrids. *Cr. Acad. Sci. IV Phys.* **2001,** *2*, 1505-1508.

88. Singh, A. R.; Giri, D.; Kumar, S., Force induced melting of the constrained DNA. *J. Chem. Phys.* **2010,** *132*, 235105.

89. Mosayebi, M.; Louis, A. A.; Doye, J. P. K.; Ouldridge, T. E., Force-Induced Rupture of a DNA Duplex: From Fundamentals to Force Sensors. *ACS Nano* **2015,** *9*, 11993-12003.

90. Wang, X.; Ha, T., Defining Single Molecular Forces Required to Activate Integrin and Notch Signaling. *Science* **2013,** *340*, 991-994.

91. Murad, Y.; Li, I. T. S., Quantifying Molecular Forces with Serially Connected Force Sensors. *Biophysical journal* **2019,** *116*, 1282-1291.

92. Wang, X.; Rahil, Z.; Li, I. T. S.; Chowdhury, F.; Leckband, D. E.; Chemla, Y. R.; Ha, T., Constructing modular and universal single molecule tension sensor using protein G to study mechano-sensitive receptors. *Sci. Rep.* **2016,** *6*, 21584.

93. Anwesha, S.; Yuanchang, Z.; Yongliang, W.; Xuefeng, W., Force-activatable coating enables high-resolution cellular force imaging directly on regular cell culture surfaces. *Phys. Biol.* **2018,** *15*, 065002.

94. Jo, M. H.; Cottle, W. T.; Ha, T., Real-Time Measurement of Molecular Tension during Cell Adhesion and Migration Using Multiplexed Differential Analysis of Tension Gauge Tethers. *ACS Biomater. Sci. Eng.* **2018**.

95. Wang, Y.; LeVine, D. N.; Gannon, M.; Zhao, Y.; Sarkar, A.; Hoch, B.; Wang, X., Force-activatable biosensor enables single platelet force mapping directly by fluorescence imaging. *Biosens. Bioelectron.* **2018,** *100*, 192-200.

96. Zhao, Y.; Wang, Y.; Sarkar, A.; Wang, X., Keratocytes Generate High Integrin Tension at the Trailing Edge to Mediate Rear De-adhesion during Rapid Cell Migration. *iSci.* **2018,** *9*, 502-512.

97. Li, I. T. S.; Ha, T.; Chemla, Y. R., Mapping cell surface adhesion by rotation tracking and adhesion footprinting. *Sci. Rep.* **2017,** *7*, 44502.

98. Heldin, C.-H., Dimerization of cell surface receptors in signal transduction. *Cell* **1995,** *80*, 213-223.

99. Schlessinger, J., Ligand-Induced, Receptor-Mediated Dimerization and Activation of EGF Receptor. *Cell* **2002,** *110*, 669-672.

100. Lemmon, M. A.; Schlessinger, J., Cell Signaling by Receptor Tyrosine Kinases. *Cell* **2010,** *141*, 1117-1134.

101. Bunnell, S. C.; Hong, D. I.; Kardon, J. R.; Yamazaki, T.; McGlade, C. J.; Barr, V. A.; Samelson, L. E., T cell receptor ligation induces the formation of dynamically regulated signaling assemblies. *J. Cell Biol.* **2002,** *158*, 1263-1275.

102. Yokosuka, T.; Sakata-Sogawa, K.; Kobayashi, W.; Hiroshima, M.; Hashimoto-Tane, A.; Tokunaga, M.; Dustin, M. L.; Saito, T., Newly generated T cell receptor microclusters initiate and sustain T cell activation by recruitment of Zap70 and SLP-76. *Nat. Immunol.* **2005,** *6*, 1253-1262.

103. Wu, H., Higher-Order Assemblies in a New Paradigm of Signal Transduction. *Cell* **2013,** *153*, 287-292.

104. Manz, B. N.; Groves, J. T., Spatial organization and signal transduction at intercellular junctions. *Nat. Rev. Mol. Cell Biol.* **2010,** *11*, 342-352.

105. Wang, N.; Suo, Z., Long-distance propagation of forces in a cell. *Biochem. Biophys. Res. Commun.* **2005,** *328*, 1133-1138.

106. Lanzavecchia, A., Antigen-specific interaction between T and B cells. *Nature* **1985,** *314*, 537-539.

107. Friedl, P.; Bröcker, E.-B., TCR triggering on the move: diversity of T-cell interactions with antigen-presenting cells. *Immunol. Rev.* **2002,** *186*, 83-89.

108. Varma, R.; Campi, G.; Yokosuka, T.; Saito, T.; Dustin, M. L., T Cell Receptor-Proximal Signals Are Sustained in Peripheral Microclusters and Terminated in the Central Supramolecular Activation Cluster. *Immunity* **2006,** *25*, 117-127.

109. Yu, Y.; Smoligovets, A. A.; Groves, J. T., Modulation of T cell signaling by the actin cytoskeleton. *J. Cell Sci.* **2013,** *126*, 1049-1058.

110. Ritter, A. T.; Angus, K. L.; Griffiths, G. M., The role of the cytoskeleton at the immunological synapse. *Immunol. Rev.* **2013,** *256*, 107-117.

111. Ma, Z.; Finkel, T. H., T cell receptor triggering by force. *Trends Immunol.* **2010,** *31*, 1-6.

112. Chen, W.; Zhu, C., Mechanical regulation of T-cell functions. *Immunol. Rev.* **2013,** *256*, 160-176.

113. Gross, C. C.; Brzostowski, J. A.; Liu, D.; Long, E. O., Tethering of Intercellular Adhesion Molecule on Target Cells Is Required for LFA-1–Dependent NK Cell Adhesion and Granule Polarization. *J. Immunol.* **2010,** *185*, 2918-2926.

114. Liu, Z.; Liu, Y.; Chang, Y.; Seyf, H. R.; Henry, A.; Mattheyses, A. L.; Yehl, K.; Zhang, Y.; Huang, Z.; Salaita, K., Nanoscale optomechanical actuators for controlling mechanotransduction in living cells. *Nat. Meth.* **2015,** *13*, 143-151.

115. Bashour, K. T.; Gondarenko, A.; Chen, H.; Shen, K.; Liu, X.; Huse, M.; Hone, J. C.; Kam, L. C., CD28 and CD3 have complementary roles in T-cell traction forces. *Proc. Natl. Acad. Sci. USA* **2014,** *111*, 2241-2246.

116. Stabley, D. R.; Jurchenko, C.; Marshall, S. S.; Salaita, K. S., Visualizing mechanical tension across membrane receptors with a fluorescent sensor. *Nat. Meth.* **2012,** *9*, 64-67.

117. Jurchenko, C.; Salaita, K. S., Lighting Up the Force: Investigating Mechanisms of Mechanotransduction Using Fluorescent Tension Probes. *Mol. Cell. Biol.* **2015,** *35*, 2570-2582.

118. Galior, K.; Liu, Y.; Yehl, K.; Vivek, S.; Salaita, K., Titin-Based Nanoparticle Tension Sensors Map High-Magnitude Integrin Forces within Focal Adhesions. *Nano Lett.* **2016,** *16*, 341-348.

119. Zhang, Y.; Ge, C.; Zhu, C.; Salaita, K., DNA-based digital tension probes reveal integrin forces during early cell adhesion. *Nat Commun* **2014,** *5*, 5167.

120. Blakely, B. L.; Dumelin, C. E.; Trappmann, B.; McGregor, L. M.; Choi, C. K.; Anthony, P. C.; Duesterberg, V. K.; Baker, B. M.; Block, S. M.; Liu, D. R.; Chen, C. S., A DNA-based molecular probe for optically reporting cellular traction forces. *Nat Meth* **2014,** *11*, 1229-1232.

121. Liu, Y.; Medda, R.; Liu, Z.; Galior, K.; Yehl, K.; Spatz, J. P.; Cavalcanti-Adam, E. A.; Salaita, K., Nanoparticle Tension Probes Patterned at the Nanoscale: Impact of Integrin Clustering on Force Transmission. *Nano Lett.* **2014,** *14*, 5539-5546.

122. Ma, V. P.-Y.; Liu, Y.; Yehl, K.; Galior, K.; Zhang, Y.; Salaita, K., Mechanically Induced Catalytic Amplification Reaction for Readout of Receptor-Mediated Cellular Forces. *Angew. Chem. Int. Ed.* **2016,** *55*, 5488-5492.

123. Liu, Y.; Blanchfield, L.; Ma, V. P.-Y.; Andargachew, R.; Galior, K.; Liu, Z.; Evavold, B. D.; Salaita, K., T Cells Transmit Piconewton Force to their Antigens for Enhanced Fidelity. *Proc. Natl. Acad. Sci. USA* **2016,** *113*, 5610-5615.

124. Katsumi, A.; Orr, A. W.; Tzima, E.; Schwartz, M. A., Integrins in Mechanotransduction. *J. Biol. Chem.* **2004,** *279*, 12001-12004.

125. Cremer, P. S.; Boxer, S. G., Formation and Spreading of Lipid Bilayers on Planar Glass Supports. *J. Phys. Chem. B* **1999,** *103*, 2554-2559.

126. Castellana, E. T.; Cremer, P. S., Solid supported lipid bilayers: From biophysical studies to sensor design. *Surf. Sci. Rep.* **2006,** *61*, 429-444.

127. Kaizuka, Y.; Douglass, A. D.; Varma, R.; Dustin, M. L.; Vale, R. D., Mechanisms for segregating T cell receptor and adhesion molecules during immunological synapse formation in Jurkat T cells. *Proc. Natl. Acad. Sci. USA* **2007,** *104*, 20296-20301.

128. Hartman, N. C.; Nye, J. A.; Groves, J. T., Cluster size regulates protein sorting in the immunological synapse. *Proc. Natl. Acad. Sci. USA* **2009,** *106*, 12729-12734.

129. Manz, B. N.; Jackson, B. L.; Petit, R. S.; Dustin, M. L.; Groves, J., T-cell triggering thresholds are modulated by the number of antigen within individual T-cell receptor clusters. *Proc. Natl. Acad. Sci. USA* **2011,** *108*, 9089-9094.

130. O'Donoghue, G. P.; Pielak, R. M.; Smoligovets, A. A.; Lin, J. J.; Groves, J. T., Direct single molecule measurement of TCR triggering by agonist pMHC in living primary T cells. *eLife* **2013,** *2*, e00778.

131. Caculitan, N. G.; Kai, H.; Liu, E. Y.; Fay, N.; Yu, Y.; Lohmüller, T.; O'Donoghue, G. P.; Groves, J. T., Size-Based Chromatography of Signaling Clusters in a Living Cell Membrane. *Nano Lett.* **2014,** *14*, 2293-2298.

132. Biswas, K. H.; Hartman, K. L.; Yu, C.-h.; Harrison, O. J.; Song, H.; Smith, A. W.; Huang, W. Y. C.; Lin, W.-C.; Guo, Z.; Padmanabhan, A.; Troyanovsky, S. M.; Dustin, M. L.; Shapiro, L.; Honig, B.; Zaidel-Bar, R.; Groves, J. T., E-cadherin junction formation involves an active kinetic nucleation process. *Proc. Natl. Acad. Sci. USA* **2015,** *112*, 10932-10937.

133. Greene, Adrienne C.; Lord, Samuel J.; Tian, A.; Rhodes, C.; Kai, H.; Groves, Jay T., Spatial Organization of EphA2 at the Cell-Cell Interface Modulates Trans-Endocytosis of EphrinA1. *Biophysical journal* **2014,** *106*, 2196-2205.

134. Narui, Y.; Salaita, K., Membrane Tethered Delta Activates Notch and Reveals a Role for Spatio-Mechanical Regulation of the Signaling Pathway. *Biophysical journal* **2013,** *105*, 2655-2665.

135. Yu, C.-h.; Law, J. B. K.; Suryana, M.; Low, H. Y.; Sheetz, M. P., Early integrin binding to Arg-Gly-Asp peptide activates actin polymerization and contractile movement that stimulates outward translocation. *Proc. Natl. Acad. Sci. USA* **2011,** *108*, 20585-20590.

136. Yu, C.-h.; Rafiq, Nisha Bte M.; Krishnasamy, A.; Hartman, Kevin L.; Jones, Gareth E.; Bershadsky, Alexander D.; Sheetz, Michael P., Integrin-Matrix Clusters Form Podosome-like Adhesions in the Absence of Traction Forces. *Cell Rep.* **2013,** *5*, 1456-1468.

137. Yu, C.-h.; Rafiq, N. B. M.; Cao, F.; Zhou, Y.; Krishnasamy, A.; Biswas, K. H.; Ravasio, A.; Chen, Z.; Wang, Y.-H.; Kawauchi, K.; Jones, G. E.; Sheetz, M. P., Integrin-beta3 clusters recruit clathrin-mediated endocytic machinery in the absence of traction force. *Nat. Commun.* **2015,** *6*, 8672.

138. Ha, T.; Enderle, T.; Ogletree, D. F.; Chemla, D. S.; Selvin, P. R.; Weiss, S., Probing the interaction between two single molecules: fluorescence resonance energy transfer between a single donor and a single acceptor. *Proc. Natl. Acad. Sci. USA* **1996,** *93*, 6264-6268.

139. Yun, C. S.; Javier, A.; Jennings, T.; Fisher, M.; Hira, S.; Peterson, S.; Hopkins, B.; Reich, N. O.; Strouse, G. F., Nanometal Surface Energy Transfer in Optical Rulers, Breaking the FRET Barrier. *J. Am. Chem. Soc.* **2005,** *127*, 3115-3119.

140. Bendix, P. M.; Pedersen, M. S.; Stamou, D., Quantification of nano-scale intermembrane contact areas by using fluorescence resonance energy transfer. *Proc. Natl. Acad. Sci. USA* **2009,** *106*, 12341-12346.

141. Vardhana, S.; Choudhuri, K.; Varma, R.; Dustin, M. L., Essential Role of Ubiquitin and TSG101 Protein in Formation and Function of the Central Supramolecular Activation Cluster. *Immunity* **2010,** *32*, 531-540.

142. Martínez-Martín, N.; Fernández-Arenas, E.; Cemerski, S.; Delgado, P.; Turner, M.; Heuser, J.; Irvine, Darrell J.; Huang, B.; Bustelo, Xosé R.; Shaw, A.; Alarcón, B., T Cell Receptor Internalization from the Immunological Synapse Is Mediated by TC21 and RhoG GTPase-Dependent Phagocytosis. *Immunity* **2011,** *35*, 208-222.

143. Dustin, M. L.; Cooper, J. A., The immunological synapse and the actin cytoskeleton: molecular hardware for T cell signaling. *Nat. Immunol.* **2000,** *1*, 23-29.

144. Ilani, T.; Vasiliver-Shamis, G.; Vardhana, S.; Bretscher, A.; Dustin, M. L., T cell antigen receptor signaling and immunological synapse stability require myosin IIA. *Nat. Immunol.* **2009,** *10*, 531-539.

145. Yu, Y.; Fay, N. C.; Smoligovets, A. A.; Wu, H.-J.; Groves, J. T., Myosin IIA Modulates T Cell Receptor Transport and CasL Phosphorylation during Early Immunological Synapse Formation. *PLoS ONE* **2012,** *7*, e30704.

146. Judokusumo, E.; Tabdanov, E.; Kumari, S.; Dustin, Michael L.; Kam, Lance C., Mechanosensing in T Lymphocyte Activation. *Biophys. J.* **2012,** *102*, L5-L7.

147. Ma, V. P.-Y.; Liu, Y.; Yehl, K.; Galior, K.; Zhang, Y.; Salaita, K., Mechanically Induced Catalytic Amplification Reaction for Readout of Receptor-Mediated Cellular Forces. *Angew. Chem. Int. Ed.* **2016,** *128*, 5578-5582.

148. Yehl, K.; Mugler, A.; Vivek, S.; Liu, Y.; Zhang, Y.; Fan, M.; Weeks, E. R.; Salaita, K., High-speed DNA-based rolling motors powered by RNase H. *Nat. Nanotechnol.* **2015,** *11*, 184.

149. Hill, H. D.; Mirkin, C. A., The bio-barcode assay for the detection of protein and nucleic acid targets using DTT-induced ligand exchange. *Nat. Protoc.* **2006,** *1*, 324.

150. Nair, P. M.; Salaita, K.; Petit, R. S.; Groves, J. T., Using patterned supported lipid membranes to investigate the role of receptor organization in intercellular signaling. *Nat. Protoc.* **2011,** *6*, 523.

151. Bousso, P.; Robey, E., Dynamics of CD8+ T cell priming by dendritic cells in intact lymph nodes. *Nat. Immunol.* **2003,** *4*, 579-585.

152. Dustin, M. L., The Immunological Synapse. *Cancer Immunol. Res.* **2014,** *2*, 1023-1033.

153. Das, D. K.; Feng, Y.; Mallis, R. J.; Li, X.; Keskin, D. B.; Hussey, R. E.; Brady, S. K.; Wang, J.-H.; Wagner, G.; Reinherz, E. L.; Lang, M. J., Force-dependent transition in the T-cell receptor β-subunit allosterically regulates peptide discrimination and pMHC bond lifetime. *Proc. Natl. Acad. Sci. USA* **2015,** *112*, 1517-1522.

154. Kim, S. T.; Takeuchi, K.; Sun, Z.-Y. J.; Touma, M.; Castro, C. E.; Fahmy, A.; Lang, M. J.; Wagner, G.; Reinherz, E. L., The αβ T Cell Receptor Is an Anisotropic Mechanosensor. *Proc. Natl. Acad. Sci. USA* **2009,** *284*, 31028-31037.

155. Bashour, K. T.; Gondarenko, A.; Chen, H.; Shen, K.; Liu, X.; Huse, M.; Hone, J. C.; Kam, L. C., CD28 and CD3 have complementary roles in T-cell traction forces. *Proc. Natl. Acad. Sci. USA* **2014,** *111*, 2241-2246.

156. Hui, K. L.; Upadhyaya, A., Dynamic microtubules regulate cellular contractility during T-cell activation. *Proc. Natl. Acad. Sci. USA* **2017,** *114*, E4175-E4183.

157. Liu, Y.; Blanchfield, L.; Ma, V. P.-Y.; Andargachew, R.; Galior, K.; Liu, Z.; Evavold, B.; Salaita, K., DNA-based nanoparticle tension sensors reveal that T-cell

receptors transmit defined pN forces to their antigens for enhanced fidelity. *Proc. Natl. Acad. Sci. USA* **2016,** *113*, 5610-5615.

158. Harris, E. S.; McIntyre, T. M.; Prescott, S. M.; Zimmerman, G. A., The Leukocyte Integrins. *J. Biol. Chem.* **2000,** *275*, 23409-23412.

159. Dustin, M. L., Integrins and Their Role in Immune Cell Adhesion. *Cell* **2019,** *177*, 499-501.

160. Dustin, M. L., The Immunological Synapse. **2014,** *2*, 1023-1033.

161. Franciszkiewicz, K.; Le Floc'h, A.; Boutet, M.; Vergnon, I.; Schmitt, A.; Mami-Chouaib, F., CD103 or LFA-1 Engagement at the Immune Synapse between Cytotoxic T Cells and Tumor Cells Promotes Maturation and Regulates T-cell Effector Functions. *Cancer Res.* **2013,** *73*, 617-628.

162. Mitroulis, I.; Alexaki, V. I.; Kourtzelis, I.; Ziogas, A.; Hajishengallis, G.; Chavakis, T., Leukocyte integrins: role in leukocyte recruitment and as therapeutic targets in inflammatory disease. *Pharmacol Ther* **2015,** *147*, 123-135.

163. Petit, A.-E.; Demotte, N.; Scheid, B.; Wildmann, C.; Bigirimana, R.; Gordon-Alonso, M.; Carrasco, J.; Valitutti, S.; Godelaine, D.; van der Bruggen, P., A major secretory defect of tumour-infiltrating T lymphocytes due to galectin impairing LFA-1-mediated synapse completion. *Nat. Commun.* **2016,** *7*, 12242.

164. Li, J.; Springer, T. A., Integrin extension enables ultrasensitive regulation by cytoskeletal force. *Proc. Natl. Acad. Sci. USA* **2017,** *114*, 4685-4690.

165. Comrie, W. A.; Li, S.; Boyle, S.; Burkhardt, J. K., The dendritic cell cytoskeleton promotes T cell adhesion and activation by constraining ICAM-1 mobility. *J. Cell Biol.* **2015,** *208*, 457-473.

166. Feigelson, S. W.; Pasvolsky, R.; Cemerski, S.; Shulman, Z.; Grabovsky, V.; Ilani, T.; Sagiv, A.; Lemaitre, F.; Laudanna, C.; Shaw, A. S.; Alon, R., Occupancy of Lymphocyte LFA-1 by Surface-Immobilized ICAM-1 Is Critical for TCR- but Not for Chemokine-Triggered LFA-1 Conversion to an Open Headpiece High-Affinity State. *J. Immunol.* **2010,** *185*, 7394-7404.

167. O'Connor, R. S.; Hao, X.; Shen, K.; Bashour, K.; Akimova, T.; Hancock, W. W.; Kam, L. C.; Milone, M. C., Substrate Rigidity Regulates Human T Cell Activation and Proliferation. *J. Immunol.* **2012,** *189*, 1330-1339.

168. Glazier, R.; Salaita, K., Supported lipid bilayer platforms to probe cell mechanobiology. *BBA Biomembr.* **2017,** *1859*, 1465-1482.

169. Perez, O. D.; Mitchell, D.; Jager, G. C.; South, S.; Murriel, C.; McBride, J.; Herzenberg, L. A.; Kinoshita, S.; Nolan, G. P., Leukocyte functional antigen 1 lowers T cell activation thresholds and signaling through cytohesin-1 and Jun-activating binding protein 1. *Nat. Immunol.* **2003,** *4*, 1083.

170. Manevich-Mendelson, E.; Feigelson, S. W.; Pasvolsky, R.; Aker, M.; Grabovsky, V.; Shulman, Z.; Kilic, S. S.; Rosenthal-Allieri, M. A.; Ben-Dor, S.; Mory, A.; Bernard, A.; Moser, M.; Etzioni, A.; Alon, R., Loss of Kindlin-3 in LAD-III eliminates LFA-1 but not VLA-4 adhesiveness developed under shear flow conditions. *Blood* **2009,** *114*, 2344-2353.

171. Dransfield, I.; Cabañas, C.; Craig, A.; Hogg, N., Divalent cation regulation of the function of the leukocyte integrin LFA-1. *J. Cell Biol.* **1992,** *116*, 219-226.

172. Huse, M., Mechanical forces in the immune system. *Nat. Rev. Immunol.* **2017,** *17*, 679.

173. Rossy, J.; Laufer, J. M.; Legler, D. F., Role of Mechanotransduction and Tension in T Cell Function. *Front. Immunol.* **2018,** *9*.

174. Pageon, S. V.; Govendir, M. A.; Kempe, D.; Biro, M., Mechanoimmunology: molecular-scale forces govern immune cell functions. *Mol. Biol. Cell* **2018,** *29*, 1919-1926.

175. Deeg, J.; Axmann, M.; Matic, J.; Liapis, A.; Depoil, D.; Afrose, J.; Curado, S.; Dustin, M. L.; Spatz, J. P., T Cell Activation is Determined by the Number of Presented Antigens. *Nano Lett.* **2013,** *13*, 5619-5626.

176. Au-Yeung, B. B.; Shah, N. H.; Shen, L.; Weiss, A., ZAP-70 in Signaling, Biology, and Disease. *Annu. Rev. Immunol.* **2018,** *36*, 127-156.

177. Wang, H.; Kadlecek, T. A.; Au-Yeung, B. B.; Goodfellow, H. E. S.; Hsu, L.-Y.; Freedman, T. S.; Weiss, A., ZAP-70: An Essential Kinase in T-cell Signaling. *Cold Spring Harb. Perspect. Biol.* **2010,** *2*, a002279.

178. Galior, K.; Liu, Y.; Yehl, K.; Vivek, S.; Salaita, K., Titin-Based Nanoparticle Tension Sensors Map High-Magnitude Integrin Forces within Focal Adhesions. *Nano Lett.* **2016,** *16*, 341-348.

179. Liu, Y.; Galior, K.; Ma, V. P.-Y.; Salaita, K., Molecular Tension Probes for Imaging Forces at the Cell Surface. *Acc. Chem. Res.* **2017,** *50*, 2915-2924.

180. Luo, B.-H.; Carman, C. V.; Springer, T. A., Structural Basis of Integrin Regulation and Signaling. *Annu. Rev. Immunol.* **2007,** *25*, 619-647.

181. Alon, R.; Dustin, M. L., Force as a Facilitator of Integrin Conformational Changes during Leukocyte Arrest on Blood Vessels and Antigen-Presenting Cells. *Immunity* **2007,** *26*, 17-27.

182. Jung, Y.; Riven, I.; Feigelson, S. W.; Kartvelishvily, E.; Tohya, K.; Miyasaka, M.; Alon, R.; Haran, G., Three-dimensional localization of T-cell receptors in relation to microvilli using a combination of superresolution microscopies. *Proc. Natl. Acad. Sci. USA* **2016,** *113*, E5916-E5924.

183. Cai, E.; Marchuk, K.; Beemiller, P.; Beppler, C.; Rubashkin, M. G.; Weaver, V. M.; Gérard, A.; Liu, T.-L.; Chen, B.-C.; Betzig, E.; Bartumeus, F.; Krummel, M. F., Visualizing dynamic microvillar search and stabilization during ligand detection by T cells. *Science* **2017,** *356*, eaal3118.

184. Dustin, M. L., Stop and Go Traffic to Tune T Cell Responses. *Immunity* **2004,** *21*, 305-314.

185. Mossman, K. D.; Campi, G.; Groves, J. T.; Dustin, M. L., Altered TCR Signaling from Geometrically Repatterned Immunological Synapses. *Science* **2005,** *310*, 1191-1193.

186. Kaizuka, Y.; Douglass, A. D.; Varma, R.; Dustin, M. L.; Vale, R. D., Mechanisms for segregating T cell receptor and adhesion molecules during immunological synapse formation in Jurkat T cells. *Proc. Natl. Acad. Sci. USA* **2007,** *104*, 20296-20301.

187. Chen, W.; Lou, J.; Zhu, C., Forcing Switch from Short- to Intermediate- and Long-lived States of the αA Domain Generates LFA-1/ICAM-1 Catch Bonds. *J. Biol. Chem.* **2010,** *285*, 35967-35978.

188. Dustin, M. L., Modular Design of Immunological Synapses and Kinapses. *Cold Spring Harb. Perspect. Biol.* **2009,** *1*, a002873.

189. Tabdanov, E.; Gondarenko, S.; Kumari, S.; Liapis, A.; Dustin, M. L.; Sheetz, M. P.; Kam, L. C.; Iskratsch, T., Micropatterning of TCR and LFA-1 ligands reveals complementary effects on cytoskeleton mechanics in T cells. *Integr. Biol.* **2015,** *7*, 1272-1284.

190. Monks, C. R. F.; Freiberg, B. A.; Kupfer, H.; Sciaky, N.; Kupfer, A., Three-dimensional segregation of supramolecular activation clusters in T cells. *Nature* **1998,** *395*, 82-86.

191. Mace, E. M.; Zhang, J.; Siminovitch, K. A.; Takei, F., Elucidation of the integrin LFA-1–mediated signaling pathway of actin polarization in natural killer cells. *Blood* **2010,** *116*, 1272-1279.

192. Barda-Saad, M.; Braiman, A.; Titerence, R.; Bunnell, S. C.; Barr, V. A.; Samelson, L. E., Dynamic molecular interactions linking the T cell antigen receptor to the actin cytoskeleton. *Nat. Immunol.* **2005,** *6*, 80-89.

193. Scholer, A.; Hugues, S.; Boissonnas, A.; Fetler, L.; Amigorena, S., Intercellular Adhesion Molecule-1-Dependent Stable Interactions between T Cells and Dendritic Cells Determine CD8⁺ T Cell Memory. *Immunity* **2008,** *28*, 258-270.

194. Natkanski, E.; Lee, W.-Y.; Mistry, B.; Casal, A.; Molloy, J. E.; Tolar, P., B Cells Use Mechanical Energy to Discriminate Antigen Affinities. *Science* **2013,** *340*, 1587-1590.

195. Wang, J.; Lin, F.; Wan, Z.; Sun, X.; Lu, Y.; Huang, J.; Wang, F.; Zeng, Y.; Chen, Y.-H.; Shi, Y.; Zheng, W.; Li, Z.; Xiong, C.; Liu, W., Profiling the origin,

dynamics, and function of traction force in B cell activation. *Sci. Signal.* **2018,** *11*, eaai9192.

196. Beningo, K. A.; Wang, Y.-l., Fc-receptor-mediated phagocytosis is regulated by mechanical properties of the target. *J. Cell Sci.* **2002,** *115*, 849-856.

197. Orr, A. W.; Helmke, B. P.; Blackman, B. R.; Schwartz, M. A., Mechanisms of Mechanotransduction. *Developmental Cell* **2006,** *10*, 11-20.

198. Ingber, D. E., Cellular mechanotransduction: putting all the pieces together again. *The FASEB Journal* **2006,** *20*, 811-827.

199. Jaalouk, D. E.; Lammerding, J., Mechanotransduction gone awry. *Nat. Rev. Mol. Cell Biol.* **2009,** *10*, 63-73.

200. Liu, Z.; Liu, Y.; Chang, Y.; Seyf, H. R.; Henry, A.; Mattheyses, A. L.; Yehl, K.; Zhang, Y.; Huang, Z.; Salaita, K., Nanoscale optomechanical actuators for controlling mechanotransduction in living cells. *Nat. Meth.* **2016,** *13*, 143-146.

201. Brantley, J. N.; Bailey, C. B.; Wiggins, K. M.; Keatinge-Clay, A. T.; Bielawski, C. W., Mechanobiochemistry: harnessing biomacromolecules for force-responsive materials. *Polymer Chem.* **2013,** *4*, 3916-3928.

202. Jurchenko, C.; Salaita, K. S., Lighting up the Force: Investigating Mechanisms of Mechanotransduction Using Fluorescent Tension Probes. *Molecular and Cellular Biology* **2015**.

203. Jurchenko, C.; Chang, Y.; Narui, Y.; Zhang, Y.; Salaita, K. S., Integrin-Generated Forces Lead to Streptavidin-Biotin Unbinding in Cellular Adhesions. *Biophysical journal* **2014,** *106*, 1436-1446.

204. Morimatsu, M.; Mekhdjian, A. H.; Chang, A. C.; Tan, S. J.; Dunn, A. R., Visualizing the Interior Architecture of Focal Adhesions with High-Resolution Traction Maps. *Nano Lett.* **2015,** *15*, 2220-2228.

205. Chang, Y.; Liu, Z.; Zhang, Y.; Galior, K.; Yang, J.; Salaita, K., A General Approach for Generating Fluorescent Probes to Visualize Piconewton Forces at the Cell Surface. *J. Am. Chem. Soc.* **2016**, DOI: 10.1021/jacs.5b11602

206. Wuite, G. J. L.; Smith, S. B.; Young, M.; Keller, D.; Bustamante, C., Single-molecule studies of the effect of template tension on T7 DNA polymerase activity. *Nature* **2000,** *404*, 103-106.

207. Maier, B.; Bensimon, D.; Croquette, V., Replication by a single DNA polymerase of a stretched single-stranded DNA *Proceedings of the National Academy of Sciences of the United States of America* **2000,** *97*, 12002-12007.

208. Mertz, D.; Vogt, C.; Hemmerle, J.; Mutterer, J.; Ball, V.; Voegel, J.-C.; Schaaf, P.; Lavalle, P., Mechanotransductive surfaces for reversible biocatalysis activation. *Nat. Mater.* **2009,** *8*, 731-735.

209. He, X.; Aizenberg, M.; Kuksenok, O.; Zarzar, L. D.; Shastri, A.; Balazs, A. C.; Aizenberg, J., Synthetic homeostatic materials with chemo-mechano-chemical self-regulation. *Nature* **2012,** *487*, 214-218.

210. Ali, M. M.; Li, F.; Zhang, Z.; Zhang, K.; Kang, D.-K.; Ankrum, J. A.; Le, X. C.; Zhao, W., Rolling circle amplification: a versatile tool for chemical biology, materials science and medicine. *Chem. Soc. Rev.* **2014,** *43*, 3324-3341.

211. Zhao, Y.; Chen, F.; Li, Q.; Wang, L.; Fan, C., Isothermal Amplification of Nucleic Acids. *Chem. Rev.* **2015,** *115*, 12491-12545.

212. Larsson, C.; Grundberg, I.; Soderberg, O.; Nilsson, M., In situ detection and genotyping of individual mRNA molecules. *Nat. Meth.* **2010,** *7*, 395-397.

213. Ke, R.; Mignardi, M.; Pacureanu, A.; Svedlund, J.; Botling, J.; Wahlby, C.; Nilsson, M., In situ sequencing for RNA analysis in preserved tissue and cells. *Nat. Meth.* **2013,** *10*, 857-860.

214. Russell, C.; Welch, K.; Jarvius, J.; Cai, Y.; Brucas, R.; Nikolajeff, F.; Svedlindh, P.; Nilsson, M., Gold Nanowire Based Electrical DNA Detection Using Rolling Circle Amplification. *ACS Nano* **2014,** *8*, 1147-1153.

215. Yehl, K.; Mugler, A.; Vivek, S.; Liu, Y.; Zhang, Y.; Fan, M.; Weeks, E. R.; Salaita, K., High-speed DNA-based rolling motors powered by RNase H. *Nat. Nanotechnol.* **2016,** *11*, 184-190.

216. Peterson, A. W.; Heaton, R. J.; Georgiadis, R. M., The effect of surface probe density on DNA hybridization. *Nucleic Acids Res.* **2001,** *29*, 5163-5168.

217. Roca-Cusachs, P.; Gauthier, N. C.; del Rio, A.; Sheetz, M. P., Clustering of α5β1 integrins determines adhesion strength whereas αvβ3 and talin enable mechanotransduction. *Proc. Natl. Acad. Sci. USA* **2009,** *106*, 16245-16250.

218. Massia, S. P.; Hubbell, J. A., An RGD spacing of 440 nm is sufficient for integrin alpha V beta 3-mediated fibroblast spreading and 140 nm for focal contact and stress fiber formation. *J. Cell Biol.* **1991,** *114*, 1089-1100.

219. Zamir, E.; Katz, M.; Posen, Y.; Erez, N.; Yamada, K. M.; Katz, B.-Z.; Lin, S.; Lin, D. C.; Bershadsky, A.; Kam, Z.; Geiger, B., Dynamics and segregation of cell-matrix adhesions in cultured fibroblasts. *Nat. Cell Biol.* **2000,** *2*, 191-196.

220. Schottelius, M.; Laufer, B.; Kessler, H.; Wester, H.-J., Ligands for Mapping αvβ3-Integrin Expression in Vivo. *Acc. Chem. Res.* **2009,** *42*, 969-980.

221. Krishnan, R.; Park, J.-A.; Seow, C. Y.; Lee, P. V. S.; Stewart, A. G., Cellular Biomechanics in Drug Screening and Evaluation: Mechanopharmacology. *Trends Pharmacol. Sci.* **2016,** *37*, 87-100.

222. Yu, Z.; Schonhoft, J. D.; Dhakal, S.; Bajracharya, R.; Hegde, R.; Basu, S.; Mao, H., ILPR G-Quadruplexes Formed in Seconds Demonstrate High Mechanical Stabilities. *J. Am. Chem. Soc.* **2009,** *131*, 1876-1882.

223. Cheng, Y.; Tang, Q.; Li, Y.; Zhang, Y.; Zhao, C.; Yan, J.; You, H., Folding/unfolding kinetics of G-quadruplexes upstream of the P1 promoter of the human BCL-2 oncogene. *J. Biol. Chem.* **2019**.

224. Dhakal, S.; Schonhoft, J. D.; Koirala, D.; Yu, Z.; Basu, S.; Mao, H., Coexistence of an ILPR i-Motif and a Partially Folded Structure with Comparable Mechanical Stability Revealed at the Single-Molecule Level. *J. Am. Chem. Soc.* **2010,** *132*, 8991-8997.

225. Koirala, D.; Shrestha, P.; Maximuck, W. J.; Cui, Y.; Mao, H.; Hidaka, K.; Emura, T.; Sugiyama, H.; Endo, M., Mechanical properties of DNA origami nanoassemblies are determined by Holliday junction mechanophores. *Nucleic Acids Res.* **2016,** *44*, 6574-6582.

226. Zohar, H.; Hetherington, C. L.; Bustamante, C.; Muller, S. J., Peptide Nucleic Acids as Tools for Single-Molecule Sequence Detection and Manipulation. *Nano Lett.* **2010,** *10*, 4697-4701.

227. Dutta, S.; Armitage, B. A.; Lyubchenko, Y. L., Probing of miniPEGγ-PNA–DNA Hybrid Duplex Stability with AFM Force Spectroscopy. *Biochemistry* **2016,** *55*, 1523-1528.

228. LaCroix, A. S.; Lynch, A. D.; Berginski, M. E.; Hoffman, B. D., Tunable molecular tension sensors reveal extension-based control of vinculin loading. *eLife* **2018,** *7*, e33927.

229. Merindol, R.; Delechiave, G.; Heinen, L.; Catalani, L. H.; Walther, A., Modular Design of Programmable Mechanofluorescent DNA Hydrogels. *Nat. Commun.* **2019,** *10*, 528.

Victor Pui-Yan Ma

NCI F99-K00 fellow/Graduate Research Assistant
Emory University
Department of Chemistry
1515 Dickey Dr
Atlanta, GA 30322

Email: pui-yan.ma@emory.edu
Phone (work): 404-727-9011
Phone (cell): 404-718-9581
Webpage: https://victorpyma.wordpress.com
Twitter: @victorpyma1

EDUCATION AND POSITION

Harvard University and Brigham and Women's Hospital, Boston, MA — Starting 2019.8
Postdoctoral Fellow in Department of Medicine, Harvard Medical School
Advisors: Jeffery M. Karp (PI, Bioengineering) and Mary-Ellen B. Taplin (Co-PI, Tumor Oncology)

Emory University, Atlanta, GA — 2013–2019.7
Ph.D., Biological Chemistry
Advisor: Khalid Salaita (Chemistry and Biomedical Engineering)

Hong Kong Baptist University, Hong Kong — 2009–2012
B.S., Chemistry

RESEARCH TRAINING

NCI K00 Postdoctoral Fellow — Starting 2019.8
With Professors Jeffery M. Karp and Mary-Ellen B. Taplin (Dana-Farber Cancer Institute)
- Development of novel biomaterials for cancer therapeutics

Graduate Research Assistant/NCI F99 Predoctoral Fellow (From 2017) — 2013–2019.7
With Professor Khalid Salaita
- Investigating the biophysical mechanism of T-cell activation using DNA force probes and supported lipid bilayer technology
- Developing liposomal-DNAzyme conjugates (Lipozymes) for gene regulation
- Developing protein-AuNP conjugates for immunophenotyping
- Developed mechanically induced catalytic amplification reaction (MCR) to study cellular traction force

Undergraduate Research Scholar and Research Assistant — 2010–2013
With Professors Dik-Lung Ma and Chung Hang Leung (ICMS, University of Macau)
- Synthesized a series of iridium complexes and studied their DNA binding behaviors
- Developed bioanalytical assays based on structural switching of G-quadruplex DNA and G-quadruplex selective Ir(III) probe
- Utilized computational tools (ICM-Pro and Discovery Studio) and methods (molecular docking, QSAR) to discover novel drug candidates

AWARDS AND HONORS

Student Leader, ACS–Younger Chemists Committee Leadership Institute — 2019
CAS SciFinder Future Leader, American Chemical Society — 2018
Charles T. Lester Award (to the best Chemistry PhD student), Emory University — 2018
The NCI Predoctoral to Postdoctoral Fellow Transition Award (F99/K00), NCI/NIH — 2017–2023
Bayer-Lindau Fellow of Lindau Nobel Laureate Meeting on Chemistry, Lindau Foundation — 2017
Education Committee Student Travel Award, Biophysical Society — 2016

Osborn R. Quayle Award, Emory University 2016
HHMI International Student Research Fellowship Nominee, Emory University 2015
HHMI International Student Research Fellowship Nominee, Emory University 2014
Dean's List, Hong Kong Baptist University 2009–2012

PUBLICATIONS

Citations = 1048 (as of May 2019); H-index = 16; ‖**Indicates equal contribution**
Google scholar profile: http://scholar.google.com/citations?user=e8kX2d8AAAAJ&hl=en
Work at Emory University

28. **Ma, V. P.-Y.** and Salaita K. "DNA nanotechnology as an emerging tool to study mechanotransduction in living systems", *Small,* **2019**, DOI: 10.1002/smll.201900961.

27. Ma, R.; Keller, A. V.; Ma, V. P.-Y., Su, H.; Deal, B. R.; Brockman, J. M. and Salaita, K. "DNA Probes that Store Mechanical Information Reveal Transient Piconewton Forces Applied by T Cells", *PNAS*, in review

26. Rao, T.; **Ma, V. P.-Y**.; Blanchard, A.; Urner, T.; Grandhi, S.; Salaita, K. and Mattheyses, A. "EGFR activation attenuates the mechanical threshold for integrin tension and focal adhesion formation", *Mol. cell.*, in review

25. **Ma, V. P.-Y.** and Salaita K. "Mechanobiology: A brighter force gauge for cells", *eLife* **2018**, *7*, e38959. (Insight)

24. Galior, K.; **Ma, V. P.-Y.**; Liu, Y.; Su, H.; Baker, N.; Panettieri, R. A.; Wongtrakool, C. and Salaita, K. "Molecular Tension Probes to Investigate the Mechanopharmacology of Single Cells: A Step toward Personalized Mechanomedicine", *Adv. Healthcare Mat.* **2018**, 7, e1800069.

23. Su, H.; Liu, Z.; Liu, Y.; **Ma, V. P.-Y.**; Blanchard, A.; Zhao. J.; Galior, K.; Dyer, R. B. and Salaita, K. "Nanoparticle force-clamp for optically controlled mechanical unfolding of DNA", *Nano Lett.* **2018**, *18*, 2630–2636

22. Zhang, Y.; Qiu, Y.; Blanchard, A.; Chang, Y.; Brockman, J.; **Ma, V. P.-Y**.; Lam, W. A. and Salaita, K. "Platelet integrins exhibit anisotropic mechanosensing and harness pN forces to mediate platelet aggregation", *PNAS* **2018**, *115*, 325–330
- Highlighted by Sciencedaily: New methods reveal the biomechanics of blood clotting (https://www.sciencedaily.com/releases/2017/12/171219133635.htm)
- See video on Emory Youtube channel explaining the work: Biomechanics of Blood Clotting (https://www.youtube.com/watch?v=NAC5hkQeh1c)

21. Brockman, J. M.; Blanchard, A. T.; **Ma, V. P.-Y**; Derricotte, W.; Zhang, Y.; Lam, W. A.; Evangelista, F. A.; Salaita, K. and Mattheyses A. L. "Mapping the 3D Orientation of Piconewton Integrin Traction Forces", *Nature Meth.* **2018**, *15*, 115–118
- Highlighted by Sciencedaily: New methods reveal the biomechanics of blood clotting (https://www.sciencedaily.com/releases/2017/12/171219133635.htm)
- Highlighted by Welt der Physik: Kraftmesser für lebende Zellen (https://www.weltderphysik.de/gebiet/leben/news/2017/kraftmesser-fuer-lebende-zellen/)
- See video on Emory Youtube channel explaining the work: Biomechanics of Blood Clotting (https://www.youtube.com/watch?v=NAC5hkQeh1c)

20. Liu, Y.; Galior, K. **Ma, V. P.-Y.** and Salaita, K. "Molecular Tension Probes for Imaging Forces at the Cell Surface", *Acc. Chem. Res.* **2017**, *50*, 2915–2924

19. **Ma, V. P.-Y.**; Liu, Y.; Blanchfield, L.; Su, H.; Evavold, B. D. and Salaita, K. "Ratiometric tension probes for mapping receptor forces and clustering at intermembrane junctions", *Nano Lett.* **2016**, *16*, 4552–4559

18. Liu, Y.; Blanchfield, L.; **Ma, V. P.-Y.**; Andargachew, R; Galior, K.; Liu, Z.; Evavold, B. D. and Salaita, K. "DNA-based tension probes reveal that T cell-generated forces are essential to Immune function", *PNAS* **2016,** *113*, 5610–5615

- Highlighted by C&EN news: T-cells tug on antigens (http://cen.acs.org/articles/94/i20/T-cells-tug-antigens.html?type=paidArticleContent)
- Highlighted by Sciencedaily: T cells use 'handshakes' to sort friends from foes (https://www.sciencedaily.com/releases/2016/05/160505145027.htm)
- See video on Emory Youtube channel explaining the work: T cells use mechanics to separate 'friends' from 'foes' (https://www.youtube.com/watch?v=fDTcserl4rM)

17. **Ma, V. P.-Y.**; Liu, Y.; Yehl, K.; Zhang, Y. and Salaita, K. "The Mechanically-induced Chain Reaction for detecting piconewton forces at the cell surface", *Angew. Chem. Int. Ed.* **2016**, *55*, 5188–5192

- Highlighted by Nature Methods: PCR for cellular forces (*Nat. Methods*, **2016**, *13*, 466–467; http://www.nature.com/nmeth/journal/v13/n6/full/nmeth.3886.html)

Prior work at HKBU as undergraduate scholar and research assistant

16. Chang, L.; Cui, W.; Yang, Y.; Xu, S.; Zhou, W.; Fu, H.; Hu, S.; Mak, S.; Hu, J.; Wang, Q.; **Ma, V. P.-Y.**; Choi, T. C.-L.; Ma, D.-L.; Tao, L.; Pang, Y.; Rowan, M. J., Anwyl, R.; Han, Y. and Wang, Q. "Protection against β-amyloid-induced synaptic and memory impairments via altering β-amyloid assembly by bis (heptyl)-cognitin", *Sci. Rep.* **2015**, *5*, 10256–10272

15. Leung, K.-H.; He, H.-Z.; **Ma, V. P.-Y.**; Zhong, H.-J.; Chan, D. S.-H.; Zhou, J.; Mergny J.-L.; Leung, C.-H. and Ma, D.-L. "Detection of base excision repair enzyme activity using a luminescent G-quadruplex selective switch-on probe", *Chem. Commun.* **2013**, *49*, 5630–5632

- Front cover of Chemical Communications (Issue 50, 2013)
- Highlighted by the Chemical Communications blog: In celebration of the 2015 Nobel Prize in Chemistry (http://blogs.rsc.org/cc/2015/10/27/in-celebration-of-the-2015-nobel-prize-in-chemistry/)

14. Leung, K.-H., He, H.-Z.; **Ma, V. P.-Y.**; Chan, D. S.-H.; Leung, C.-H. and Ma, D.-L. "A luminescent G-quadruplex switch-on probe for the highly selective and tunable detection of cysteine and glutathione", *Chem. Commun.* **2013**, *49*, 771–773

- Front cover of Chemical Communications (Issue 8, 2013)
- A part of the joint ChemComm-OBC-RSC Advances web-themed themed issue: Nucleic acids: new life, new materials (guest edited by M. Gait; M. Komiyama; D. R. Liu, J. Micklefield; N. Seeman and O. Seitz)

13. Leung, K.-H.; He, H.-Z.; **Ma, V. P.-Y.**; Yang, H.; Chan, D. S.-H.; Leung, C.-H. and Ma, D.-L. "A G-quadruplex-selective luminescent switch-on probe for the detection of sub-nanomolar human neutrophil elastase", *RSC Adv.* **2013**, *3*, 1656–1659

- A part of the joint ChemComm-OBC-RSC Advances web-based themed issue: Nucleic acids: new life, new materials (guest edited by M. Gait; M. Komiyama; D. R. Liu, J. Micklefield; N. Seeman and O. Seitz)

12. ‖Yang, H.; ‖**Ma, V. P.-Y.**, Chan, D. S.-H.; He, H.-Z.; Leung, C.-H. and Ma, D.-L. "A cyclometallated iridium(III) complex as a c-*myc* G-quadruplex stabilizer and down-regulator of c-*myc* oncogene expression", *Curr. Med. Chem.* **2013**, *20*, 576–582

11. Yang, H.; Leung, K.-H.; Chan, D. S.-H.; **Ma, V. P.-Y.**; Nanjunda, R.; Wilson, W. D.; Ma, D.-L. and Leung, C.-H. "Structure-based design of flavone derivatives as c-*myc* oncogene down-regulators", *Eur. J. Pharm. Sci.* **2013**, *48*, 130–141

10. Ma, D.-L. (P.I.); Chan, D. S.-H.; **Ma, V. P.-Y.** and Leung, C.-H. "DNA-binding small molecules as inhibitors of transcription factors", *Med. Res. Rev.* **2013**, *33*, 823–846

9. ‖Leung, K.-H.; ‖**Ma, V. P.-Y.**; He, H.-Z.; Chan, D. S.-H.; Leung, C.-H. and Ma, D.-L. "A highly selective G-quadruplex-based

luminescent switch-on probe for the detection of nanomolar strontium(II) ion in sea water", *RSC Adv.* **2012**, *2*, 8273–8276

8. Ma, D.-L. (P.I.); **Ma, V. P.-Y.**; Chan, D. S.-H.; Leung, K.-H.; He, H.-Z. and Leung, C.-H. "Recent advances in luminescent metal complexes for sensing", *Coord. Chem. Rev.* **2012**, *256*, 3087–3113

7. Leung, C.-H. (P.I.); Zhong, H.-J.; Yang, H.; Cheng, Z.; Chan, D. S.-H.; **Ma, V.P.-Y.**; Abagyan, R; Wong, C.-Y. and Ma, D.-L. "A metal-based inhibitor of tumor necrosis factor-α", *Angew. Chem. Int. Ed.* **2012**, 51, 9010–9014
- Highlighted as a frontpiece of Angewandte Chemie (Sept., 2012)

6. ‖Zhong, H.-J.; ‖**Ma, V. P.-Y.**; Cheng, Z.; Chan, D. S.-H.; He, H.-Z.; Leung, K.-H.; Ma, D.-L. and Leung, C.-H. "Discovery of a natural product inhibitor targeting protein neddylation by structure-based virtual screening", *Biochimie* **2012**, 94, 2457–2560

5. Ma, D.-L. (P.I.); He, H.-Z.; **Ma, V. P.-Y.**; Chan, D. S.-H.; Leung, K.-H.; Zhong, H.-J.; Lu, L.; Mergny, J.-L. and Leung, C.-H. "Label-free sensing of pH and silver nanoparticles using an "OR" logic gate", *Anal. Chim. Acta* **2012**, *733*, 78–83

4. Leung, C.-H. (P.I.); Yang, H.; **Ma, V. P.-Y.**; Chan, D. S.-H.; Zhong, H.-J.; Li, Y.; Fong, W.-F. and Ma, D.-L. "Inhibition of janus kinase 2 by cyclometalated rhodium complexes", *Med. Chem. Commun.* **2012**, *3*, 696–698

3. Ma, D.-L. (P.I.); **Ma, V. P.-Y.**; He, H.-Z.; Chan, D. S.-H.; Leung, K.-H.; Zhong, H.-J. and Leung, C.-H. "*In silico* screening of G-quadruplex binding ligands", *Methods* **2012**, *57*, 106–114

2. ‖He, H.-Z.; ‖**Ma, V. P.-Y.**; Leung, K.-H.; Chan, D. S.-H.; Yang, H.; Cheng, Z.; Leung, C.-H. and Ma, D.-L. "A label-free G-quadruplex-based switch-on fluorescence assay for the selective detection of ATP", *Analyst* **2012**, *137*, 1538–1540
- Featured as a "Hot paper" in Analyst (http://blogs.rsc.org/an/2012/03/08/whats-hot-highlights-from-issue-7/)

1. Ma, D.-L.; Kwan, M. H.-T.; Chan, D. S.-H.; Lee, P.; Yang, H.; **Ma, V. P.-Y.**, Bai, L.-P.; Jiang, Z.-H. and Leung, C.-H. "Crystal violet as a fluorescent switch-on probe for i-motif: label-free DNA-based logic gate", *Analyst* **2011**, *136*, 2692–2696

BOOK CHARPTERS

2. Ma, D.-L. (P.I.); **Ma, V. P.-Y.**; Leung, K.-H.; Zhong, H.-J.; He, H.-Z.; Chan, D. S.-H. and Leung, C.-H., in *Oncogene and Cancer - From Bench to Clinic*, ed. Y. Siregar, InTech, 2013, ch. 6, pp. 131–150

1. Ma, D.-L. (P.I.); **Ma, V. P.-Y.**; Chan, D. S.-H.; Leung, K.-H.; Zhong, H.-J. and Leung, C.-H., in *Natural products: Structure, bioactivity and applications*, ed. R. E. Goncalves and M. C. Pinto, Nova Science Publishers, 2012, pp. 55–74

PATENT

1. "Devices and Methods Useful for Detecting Mechanical Forces of Ligand Receptor Interactions", **2017**, US US2017-0260575 A1, **Ma, V. P.-Y.** and Salaita, K.

PRESENTATIONS

13. Nanoscale tools to interrogate chemical biology of T cells at bio/nano interfaces (**Invited Poster**)
2018 CAS SciFinder Future Leaders Symposium, Columbus, OH, August 12–18, 2018

12. Two distinct mechanical states of LFA-1-ICAM-1 bonds are mediated by different force generating machineries during TCR triggered T cell adhesion and spreading (Poster)
2018 International Physics of Living Systems Annual Meeting, Rice University, Houston, TX, June 22–26, 2018

11. Uncovering the biophysical mechanism of T cell activation (**Invited Poster**)

2nd National Cancer Institute F99 Fellows meeting, Bethesda, DC, January 11–12, 2018

10. The T cell receptor uses the force: DNA-based tension probes reveal the role of mechanical forces in ligand sensing (**Invited poster from ~400 participants**)
67th Lindau Nobel Laureate Meetings in Chemistry, Lindau Island, Germany, June 24–31, 2017

9. Ratiometric tension probes for mapping receptor forces and clustering at artificial intermembrane junctions (Poster)
61st Biophysical Society Annual Meeting, New Orleans, LA, February 13–17, 2017

8. Ratiometric tension probes for mapping receptor forces and clustering at artificial intermembrane junctions (Poster)
2016 Southeast Biomaterials Day, Georgia Tech, GA, October 14, 2016

7. Molecular tension probes reveal the role of mechanics in T-cell recognition (**Invited Oral**)
Biophysical Society Thematic Meeting-Mechanobiology of Disease, National University of Singapore, Singapore, September 27–30, 2016

6. Nanoscale optomechanical actuators for controlling mechanotransduction in living cells (Poster)
Biophysical Society Thematic Meeting-Mechanobiology of Disease, Mechanobiology Institute, National University of Singapore, Singapore, September 27–30, 2016 (On behalf of Prof. K. Salaita)

5. Spherical nucleic acid-pMHC multimer for T-cell detection and Immunophenotyping (Poster)
The 12th annual Emerson Center Lectureship Award Symposium, Emory University, GA, September 23, 2016

4. Molecular tension probes to map receptor clustering and forces at intermembrane junctions (Oral)
The 9th Southeast Meeting on Soft Materials, Georgia Tech, GA, May 16, 2016

3. The Mechanically-induced Chain Reaction (MCR) for Detecting Piconewton Forces at the Cell Surface (Poster)
The 11th annual Emerson Center Lectureship Award Symposium, Emory University, GA, October 5, 2015

2. A metal-based inhibitor of tumor necrosis factor-α (Poster)
The 6th Asian Biological Inorganic Chemistry Conference, Hong Kong Polytechnic University, Hong Kong, November 5–8, 2012 (On behalf of Prof. D.-L. Ma)

1. Label-free sensing of pH and silver nanoparticles using an "OR" logic gate (Poster)
Symposium on Cutting-Edge Analytical Science in Bio-analysis and Bio-imaging, Hong Kong Baptist University, Hong Kong, June 18–20, 2012

TEACHING

CHEM301 - Biochemistry I, Teaching Assistant (Emory)	2015 Fall
CHEM260L - Analytical Chemistry Laboratory, Teaching Assistant (Emory)	2013 Fall
CHEM3460/CHEM7800 - Organometallic Chemistry, Teaching Assistant (HKBU)	2013 Spring
CHEM3560 - Bioanalytical Chemistry, Teaching Assistant (HKBU)	2013 Spring
CHEM3480 - Advanced Materials, Teaching Assistant (HKBU)	2012 Fall

SERVICES AND MEMBERSHIP

International strategy planning committee for the ACS-Younger Chemists Committee	2019
Ad-hoc reviewer: *New J. Chem., RSC Adv., Biomed. Pharmacother., Sci. Rep. and Theranostics*	2016–present
Biophysical Society (BPS)	2016–present
American Chemical Society (ACS)	2018–present

OUTREACH

Booth organizer for "Thinking big with small scales", Atlanta Science Festival Expo 2016
Booth organizer for "Demonstration of how mixing can drive oxidation of a dye", Atlanta Science Festival Expo 2015
Booth organizer for "The Enchanted Bottle", Atlanta Science Festival Expo 2014

MENTORING

4. Yuesong Hu (Graduate student at Emory University) 2018–present
Project: Artificial antigen-presenting cells

3. Radhika Sharma (Graduate student at Emory University) 2017–present
Project: Lipid-based DNA nanostructures for gene regulation

2. Wenzheng Sun (SURE undergrad program at Emory University) 2015–2016
Project: Gold nanoparticle-protein conjugates for cell phenotyping

1. Wai-Chung Fu (Capstone student at Hong Kong Baptist University) 2012–2013
Project: Syntheses of cyclometallated Ir(III) complexes for applications in chemo-sensing
Current: Postdoctoral fellow in Prof. Timothy F. Jamison's lab at MIT Chemistry

FINANCIAL SUPPORT

The NCI Predoctoral to Postdoctoral Transition Award (F99/K00); Grant #: F99CA223074 2017–2023
Title: Enabling technologies to study how mechanics influence T cell function at the molecular and cellular levels
Role: Principal Investigator